

2023

Solid oxide membrane electrolysis of metal oxides for advanced energy applications

<https://hdl.handle.net/2144/46663>

Downloaded from DSpace Repository, DSpace Institution's institutional repository

BOSTON UNIVERSITY
COLLEGE OF ENGINEERING

Dissertation

**SOLID OXIDE MEMBRANE ELECTROLYSIS OF
METAL OXIDES FOR ADVANCED ENERGY APPLICATIONS**

by

HAOXUAN YAN

B.Eng., The University of Auckland, 2017

Submitted in partial fulfillment of the
requirements for the degree of
Doctor of Philosophy

2023

Approved by

First Reader

Uday Pal, Ph.D.
Professor of Mechanical Engineering
Professor of Materials Science and Engineering

Second Reader

Soumendra N. Basu, Ph.D.
Professor of Mechanical Engineering
Professor and associate Division Head of Materials Science and
Engineering

Third Reader

Srikanth Gopalan, Ph.D.
Associate Professor of Mechanical Engineering
Associate Professor of Materials Science and Engineering

Fourth Reader

Adam C. Powell, Ph.D.
Associate Professor of Mechanical and Materials Engineering
Associate Professor of Materials Science and Engineering
Worcester Polytechnic Institute

DEDICATION

I would like to dedicate this work to my parents, Tao Yan and Zhimei Dong,
and my wife, Zhongqi Sun.

ACKNOWLEDGMENTS

First and foremost, my heartfelt appreciation goes to my PI, Prof. Uday Pal. His astute guidance, invaluable mentorship, and persistent faith in my abilities have been instrumental in shaping this work. His enthusiasm and unwavering support have not only bolstered my academic journey but also fostered my personal and professional growth.

My co-advisors, Prof. Ludwig and Prof. Adam Powell, deserve a special mention for their expert guidance, insightful critique, and consistent encouragement. I also extend my gratitude to my committee members, Prof. Basu and Prof. Gopalan, whose expertise and advice have been pivotal in refining my research.

I extend my thanks to Bob Sjostrom, Joe Estano, Kara Morgensen, Tasker Smith, Ryan Bakinowski, Caroline Carbo and Heitor Mourato at EPIC and SIF for their exceptional advice on experimental design, sample preparation and parts machining. I'd like to thank Dr. Alexey Nikiforov and Dr. Jeff Beacon for their valuable support and instructions in scanning electron microscopy and X-ray diffraction techniques. I'd like to thank Elizabeth Flagg, Ruth Mason, Christine Ritzkowski and Anya Blount in the MSE Division for their constant assistance and unwavering dedication.

My acknowledgement also goes to my past and current colleagues. I am particularly grateful to Dr. Xiaofei Guan, Dr. Shizhao Su, Dr. Jicheng Guo, and Dr. Thomas Villalon for their valuable advice and experiences related to my PhD project. My heartfelt thanks

go to Dr. Michelle Sugimoto, Anubhav Wadehra, Alex Levy for being my excellent collaborators. I would like to sincerely thank Dr. Zhikuan Zhu, Dr. Zhihao Sun, Dr. Yan Chen Lv, Dr. Boshan Mo, Dr. Jane Banner, and Dr. Ben Levitas for their vital training and guidance when I first joined the lab. A special thanks goes to Dr. Paul Gasper, Dr. Ruofan Wang for their insights on career development. I am deeply grateful to Dr. Ayesha Akter, Jillian Mulligan, Emily Gosh, John-In Lee, Haoxiang Yu, Kaixin Suo, and Toluwalope John for their unwavering support and for being exceptional lab mates and friends. To all other colleagues who have contributed their time, shared their knowledge, and offered assistance in many forms, I express my gratitude.

I would like to express my sincere gratitude to Brett Senders, Hadassah Flagg, Federico Coppo, and Haodong Lin. As undergraduate and master students, your diligent assistance and commitment to the research work have been an invaluable contribution to the completion of this project.

My deepest gratitude goes to my family. To my parents, Tao Yan and Zhimei Dong, your unwavering love and belief in me have been my source of strength. Your sacrifices, encouragement, and lessons in perseverance have been the guiding lights in my journey, providing a strong foundation for my academic pursuits and personal growth. Last but not most importantly, to my wife, Zhongqi Sun. Your love, unwavering support, and endless understanding have been my strength. This accomplishment is as much yours as it is mine.

**SOLID OXIDE MEMBRANE ELECTROLYSIS OF
METAL OXIDES FOR ADVANCED ENERGY APPLICATIONS**

HAOXUAN YAN

Boston University, College of Engineering, 2023

Major Professor: Uday Pal, PhD., Professor of Mechanical Engineering, Professor of
Materials Science and Engineering,

ABSTRACT

This thesis presents an exploration of Solid Oxide Membrane (SOM) electrolysis as a solution to the imminent challenge of transitioning from fossil fuel dependence towards sustainable, low-carbon energy technologies. Two key applications are explored: the production of solar-grade silicon for photovoltaic cells and the recycling of iron as an electrofuel.

Solid Oxide Membrane (SOM) based electrolysis process is a promising technology that has been demonstrated to successfully produce many energy-intensive metals directly from their oxides in an efficient, economical and environmentally sound way. First, the production of solar-grade silicon from silica via a single-step SOM electrolysis process (Si-SOM) is demonstrated. During the Si-SOM electrolysis process, an yttria-stabilized zirconia (YSZ) tube was employed to separate pre-engineered molten flux with dissolved silica from the anode assembly. When the applied DC potential between the cathode and the anode exceeds the dissociation potential of silica, silicon is reduced at the cathode, while oxygen ions migrate through the YSZ membrane and are oxidized at the anode. The Si-SOM electrolytic cell design and process parameters are optimized to enable high-purity silicon deposition on the cathode and ensure stable and

efficient Si-SOM electrolysis. Electrochemical characterization and modeling of the Si-SOM electrolysis are also presented with detailed microstructural analysis of the silicon deposits.

In parallel, this thesis demonstrates an innovative method of reducing the iron oxide to iron via a molten salt-free SOM electrolysis (Fe-SOM). Iron oxide and liquid silver as the reducing medium are contained in a one-end closed YSZ membrane. The soluble oxygen is pumped out of liquid silver with an applied potential between the cathode and the anode to create a reducing condition that is sufficient to reduce the iron oxide. The Fe-SOM electrolytic cell design and process parameters are optimized to enable high-efficiency and stable electrolysis of iron oxide. Electrochemical characterization of the Fe-SOM electrolysis is also presented with detailed microstructural analysis of the iron deposits.

TABLE OF CONTENTS

DEDICATION.....	iv
ACKNOWLEDGMENT.....	v
ABSTRACT.....	vii
TABLE OF CONTENTS.....	ix
LIST OF TABLES.....	xi
LIST OF FIGURES	xii
LIST OF ABBREVIATIONS.....	xvii
1. Introduction.....	1
1.1 Background of Silicon Production.....	1
1.2 Conceptual Use of Iron as An Alternative Electrofuel	4
1.3 SOM Process Overview	8
1.4 Research Scope	14
2. SOM CELL DESIGN AND ENGINEERING	16
2.1 Si-SOM Cell Design and Engineering.....	16
2.2. Fe-SOM Cell Design and Engineering	26
2.3 Summary.....	29
3. OPTIMIZATION PROCESS OF SILICON-SOM ELECTROLYSIS	31
3.1 Introduction.....	31
3.2 Si-SOM Cell Electrolysis with Initial Setup.....	32
3.3 Silicon Cathode Stability Analysis	33
3.4 Elimination of Carbon and Zirconium Impurities	40

3.5	Elimination of Silicon-Magnesium-Oxygen Phase	63
3.6	Summary	70
4.	SOM ELECTROLYSIS PROCESS FOR SILICON PRODUCTION	72
4.1	Experimental Setup	72
4.2	Electrochemical Characterization	75
4.3	Post-experimental Characterization	81
4.4	Electrochemical Modelling	86
4.5	Summary	99
5.	SOM ELECTROLYSIS PROCESS FOR IRON RECYCLING	101
5.1	Fe-SOM Electrolysis Process with YSZ and Silver as the Reducing Medium	101
5.2	Fe-SOM Electrolysis Process with Silver as the Reducing Medium.....	109
5.3	Summary	117
6.	CONCLUSION AND FUTURE WORK	119
6.1	Conclusion	119
6.2	Future Work	121
	BIBLIOGRAPHY	123
	CURRICULUM VITAE.....	128

LIST OF TABLES

Table 2.1. Standard Dissociation Potential of Silica and Other Major Oxides with A Graphite Anode Current Collector at 1100 C.	18
Table 2.2. Standard Dissociation Potential of Silica and Other Major Impurities with an inert anode current collector at 1100 C.	20
Table 2.3. Optical Basicity of Major Oxides and Fluorides in the SOM environment	23
Table 3.1. Descriptions, Schematics and Observations of Si wafer Stability Experiment	36
Table 3.2. Description, Aim and Observation of Experiments to Validate the Source and Formation Mechanism of Zirconium Impurities.....	53
Table 3.3. Composition of YSZ in Bulk of the YSZ Membrane and Degradation Layer in Flux #4 and Flux #5.	57
Table 3.4 Composition of Si-Zr-O Observed in Different Regions at the Cathode/Flux Interface.	58
Table 3.5. Composition of the Si Deposits and Si Cathode after the Electrolysis.....	69
Table 4.1. Total, Electronic and Ionic resistance of the Flux with the Electronic Transference Number before and after Electrolysis.	77
Table 4.2. Total and Ohmic Resistance of the SOM Cell before Electrolysis 1, after Electrolysis 1 and After Electrolysis 2.....	78
Table 4.3. Definitions of Symbols in the SOM equivalent circuit.....	88

LIST OF FIGURES

Figure 1.1. Schematics of Conventional Solar Silicon Production of: A). Siemens process; B) Fluidized Bed Reactor process	3
Figure 1.2. Volumetric and Gravimetric Energy Densities of Chemical Energy Carriers .	5
Figure 1.3. Schematics of a CO ₂ -free Iron Reduction–oxidation Cycle.....	6
Figure 1.4. Schematics of Molten Salt-based SOM Process for Silicon Production.....	10
Figure 1.5. Salt-Free SOM Process for Iron Oxide Reduction with YSZ and Silver as the Reducing Medium.....	12
Figure 2.1. Schematics of the LSM-Inconel Current Collector	19
Figure 2.2. Ag-Fe Phase Diagram.....	26
Figure 2.3. Schematics of the Fe-SOM Cell Setup.....	27
Figure 3.1. Schematics of the initial Si-SOM Cell Experimental Setup.....	33
Figure 3.2. A SEM image of the interface between Silicon Cathode and the flux after the electrolysis	34
Figure 3.3. SEM Image of the As-received Silicon Wafer.....	37
Figure 3.4. SEM Image of the Silicon Wafer above Flux in 1150 C for 6 hrs.	37
Figure 3.5 SEM Image of the Silicon Wafer Partially Immersed in the Flux.	38
Figure 3.6 SEM image of the Silicon Wafer completely immersed at 1.5 cm deep in the flux.....	38
Figure 3.7 SEM image of the Silicon Wafer completely immersed at 3 cm deep in the flux.....	39
Figure 3.8 Reaction Mechanism of Si Wafer Thinning.....	40

Figure 3.9. SEM image of the Si-containing deposits at the interface between cathode and flux	42
Figure 3.10 SEM image of the Si-containing deposits dispersed in the flux.....	42
Figure 3.11. EDS Point Analysis of the Si-containing Deposits at the Cathode/Flux Interface	43
Figure 3.12. EDS Point Analysis of the Si-containing Deposits dispersed in the Flux....	44
Figure 3.13. EDS Mapping of the YSZ membrane in Contact with the Flux.....	45
Figure 3.14. Si-C-O Phase Stability Diagram at 1100 C.	47
Figure 3.15. SEM Image of the Si-Zr-O at the Cathode/Flux Interface.	49
Figure 3.16. EDS Point Analysis of the Si-containing Deposits with Zr as the Major Impurity.....	49
Figure 3.17. SEM Image of the Pristine YSZ Membrane.....	54
Figure 3.18. SEM Image of YSZ/Flux Interface after Flux Run #2.	55
Figure 3.19. EDS spot analysis of ZrC_x at the YSZ/Flux Interface after Flux Run #2.....	55
Figure 3.20. SEM Image of YSZ/Flux Interface after Flux Run #4	56
Figure 3.21. SEM Image of YSZ/Flux Interface after Flux Run #5	56
Figure 3.22. SEM Image of the the Cathode/Flux Interface after the Carbon-free electrolysis (50X Magnification)	60
Figure 3.23. EDS mapping of the Cathode/Flux Interface after the Carbon-free Electrolysis.....	60
Figure 3.24. SEM image of the Cathode/Flux Interface after the Carbon-free electrolysis (1 kX magnification).....	61

Figure 3.25 EDS Spot Analysis of the Si-Mn-Cr Deposits.	62
Figure 3.26 EDS Spot Analysis of the Si-Mg-O Phase.	62
Figure 3.27. Phase Diagram of $\text{CaF}_2\text{-MgF}_2\text{-CaO-SiO}_2$ with Eutectic $\text{CaF}_2 - \text{MgF}_2$ and 10 mol% CaO (9 wt%).....	65
Figure 3.28 Phase Diagram of $\text{CaF}_2\text{-MgF}_2\text{-CaO-SiO}_2$, with eutectic $\text{CaF}_2 - \text{MgF}_2$ and 5 mol% CaO (4 wt%).....	67
Figure 3.29 SEM Image of the Cathode/Flux Interface after the carbon and Stainless steel-free Electrolysis.....	68
Figure 3.30. EDS Mapping of the Cathode/Flux Interface after the Carbon-free Electrolysis.....	69
Figure 4.1. Optimized Si-SOM Cell Setup.	72
Figure 4.2. Schematics of the Cathode Assembly that consists of Silicon Wafer Cathode, Tungsten Current Collector and Stainless-steel Extension Rod.	74
Figure 4.3. PDS showing the Current-Potential Behavior in the potential range of A). 0.2 to 2 V; B). 0.7 to 1.1 V.	77
Figure 4.4. Current-Time Plots during Electrolysis 1 and Electrolysis 2 with applied potential of 1.75 V for 12 hrs each.	79
Figure 4.5. Current Efficiency during Electrolysis 1 and Electrolysis 2.	81
Figure 4.6. Optical Microscopy Image (10X) of the Cathode/Flux Interface after Electrolysis.....	82
Figure 4.7. EDS mapping of the Cathode/Flux Interface.	82
Figure 4.8. EDS Spot Analysis of the Silicon Deposits near the Cathode/Flux Interface.	83

Figure 4.9. SEM Image of the Tungsten Current Collector that was Immsered in the Flux during Electrolysis.	84
Figure 4.10. EDS Mapping of the Tungsten Current Collector that was Immsered in the Flux during Electrolysis.....	85
Figure 4.11. Equivalent Circuit of the SOM Process for Silicon Production.	87
Figure 4.12. Simplified Equivalent Circuit for the Optimized Si-SOM Process.....	89
Figure 4.13. Curve Fitting of Measured Applied Potential and Net Current.....	97
Figure 4.14. Ohmic, Activation, Anode Overpotential and Cathodic Concentration Polarization as a function of the Net Current by Modeling on the SOM cell.....	98
Figure 5.1. Experimental Setup of Salt-free SOM Process for Iron Production using Ag and YSZ as the reducing medium.....	102
Figure 5.2. Current-Potential Relationship Before and After the Pre-electrolysis	103
Figure 5.3. Current-Time Profile during Electrolysis 1 and Electrolysis 2 with an applied potential of 1.75 V for 2 hrs and 1.5 hrs respectively.....	105
Figure 5.4.A). SEM images of the post-experiment compact(bulk). B). EDS mapping of the corressponding area.....	107
Figure 5.5. EDS point analysis on Spectrum 98 showing the purity of iron deposits	107
Figure 5.6. A). SEM images of the post-experiment cathode/compact interface. B). EDS mapping of the corressponding area.	108
Figure 5.7. EDS point analysis of: A). the iron deposits at the cathode/compact interface. B. the iron cathode.	108
Figure 5.8. XRD spectrum of the compact before and after electrolysis.....	109

Figure 5.9. Experimental Setup of Molten Salt-free SOM process for iron production using Ag as the reducing medium.....	110
Figure 5.10. PDS showing the current-potential relationship in Fe-SOM experiments with and without YSZ in the compact	111
Figure 5.11. Current-Time Profile in the time span of A) 0 to 21600 seconds. B). 0 to 7800 seconds.....	113
Figure 5.12. Electronic conductivity of 8YSZ as a function of the oxygen partial pressure	114
Figure 5.13. EDS Mapping of the Post-electrolysis Compact (Bulk).....	116
Figure 5.14. EDS Mapping of the Post-electrolysis Cathode/Compact Interface.	116
Figure 5.15. EDS Spot Analysis of the Iron Deposits	117

LIST OF ABBREVIATIONS

DC	Direct Current
DRI	Direct Reduction of Iron
EDM	Electrical Discharge Machining
EDS	Energy Dispersive X-ray Spectroscopy
EIS	Electrochemical Impedance Spectroscopy
FBR	Fluidized Bed Reactor
LSM	Strontium-doped Lanthanum Manganite
PDS	Potentiodynamic Scans
SEM	Scanning Electron Microscopy
SOM	Solid Oxide Membrane
XRD	X-ray Diffraction
YDL	Ytria Depletion Layer
YSZ	Ytria-stabilized Zirconia

1. Introduction

Fossil fuels are a convenient and widely accessible source of stored solar energy that has enabled our modern civilization; but fossil-fuel production cannot indefinitely keep up with rising energy demand, and carbon dioxide emissions from fossil-fuel combustion contribute to climate change. To meet the increasing energy demand of the global economy and mitigate the climate change, sustainable, clean, and low-carbon power generation and storage technologies need to be developed and adopted in a large scale. Out of a wide range of promising alternative power generation technologies, two specific applications have drawn the author's attention: Silicon used in photovoltaic cells and Iron used as an alternative electrofuel.

1.1 Background of Silicon Production

Silicon is one of the most plentiful elements in the earth's crust, accounting for approximately 25.7 percent of the total mass [1]. Silicon in its high purity form is often used to make photovoltaic cells, which are capable of 'harnessing' solar energy and turning it into electricity. These silicon-based cells account for around 90 to 95 percent of the photovoltaics industry. Polycrystalline and monocrystalline silicon cells are two of the most common forms of silicon cells. Both kinds require the same supply of high-quality silicon.

Silicon photovoltaics are one of the most environmentally friendly ways for harvesting and converting solar energy flux into electricity. The conventional method of generating electricity relies on the combustion of carbon-rich fuels to propel turbines. This process is, however, unsustainable due to the large emission of greenhouse gases

like CO₂. Brown coal, hard coal, and natural gas, respectively, emit 1.183, 1.142, and 0.572 kilograms (kg) of CO₂ per kWh of power generated [2]. In contrast, the use of silicon solar cells, whether monocrystalline or polycrystalline, is estimated to have an environmental cost of 27 to 38 grams of CO₂ per kWh of electricity produced [3]. Due to its lesser environmental impact, the market value of silicon photovoltaics is expected to reach \$150 billion by 2024 with an expected growth of 920 gigawatts [4].

To meet the current demand, the need to develop low-cost solar cells remains a critical priority for future growth. Numerous processes are used to produce the ultrapure silicon required for photovoltaics (purity over 99.9999%, 6N) and electronics (purity over 99.9999999%, 9N). All large-scale processes initiate from the carbothermic reduction of high purity silica to metallurgical grade (MG) silicon. In this process, silicon purity is affected by the introduction of carbon, boron, phosphorous, alkane earth metals, and transition metals, which exist as impurities in the raw silica. Secondary refining processes are therefore needed. The most prominent techniques are the Siemens process and fluidized bed reactors.

In Siemens process, small particles of MG silicon are ground up and react with hydrogen chloride (HCl). The resulting trichlorosilane (TCS) has a low boiling point of 31.8 degrees °C, allowing it to be purified relatively easily in tall distillation columns. Silicon is then deposited from the TCS onto highly pure, slim silicon filaments, which are electrically heated to up to 1,150 °C in a steel bell-jar reactor (see **Figure 1.1a**) until they have grown to polysilicon rods with a diameter of 15 to 20 cm [5].

A fluidized bed reactor (FBR) is cylindrical in shape. Through nozzles at the

bottom, silicon-containing gas is combined with hydrogen (H_2) to create a fluidized bed that carries microscopic silicon seed particles fed from above (see **Figure 1.1B**). Most FBR facilities use SiH_4 as the feed gas. When the decomposition temperature of SiH_4 is reached, Silicon builds up on the seed particles until they grow into larger granules that fall to the bottom of the reactor. It is noted that those granules can be removed continuously, whereas Siemens process is a batch or semi-batch processing [5].

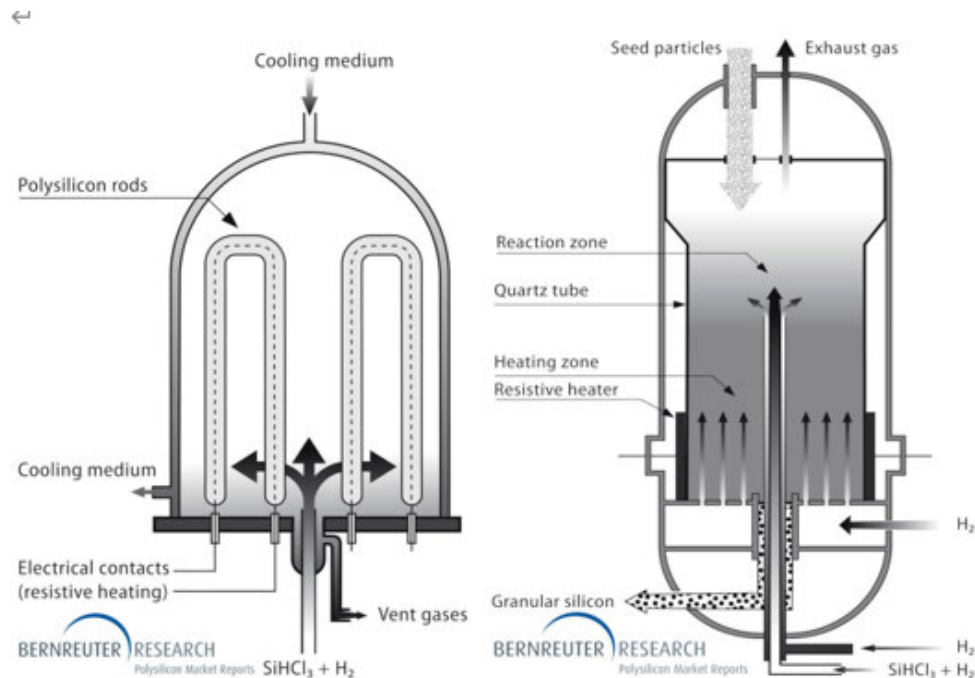


Figure 1.1. Schematics of Conventional Solar Silicon Production of: A). Siemens process; B) Fluidized Bed Reactor process

Both techniques react MG silicon with gaseous chemicals and generate new, solar grade silicon crystals. These procedures are labor-intensive, involve many steps, and use potentially hazardous halogenated compounds [6]. In addition, carbon dioxide and halogenated emissions are produced in the manufacturing supply chain. Thus, the demand for a low-cost, environmentally friendly, and efficient method of silicon manufacturing persists.

1.2 Conceptual Use of Iron as An Alternative Electrofuel

Electrofuels are low-carbon, recyclable fuels that are produced primarily from electricity. They can provide high energy and energy densities and are recycled back into reactive fuel after the fuels are combusted. H₂ has long been regarded as an ideal electrofuel. However, limited energy-cycle efficiency and problems with hydrogen storage and safety limits its ability to replace fossil fuels at a global scale and thus provides the necessary motivation for researching alternative electrofuels.

In the search for the alternative electrofuels, the periodic table unveils the potential candidates [7]. Since the fuel must be oxidized by air oxygen, only elements of groups 1-14 are applicable. In addition, it is desired that the fuel has a high specific energy, which necessitates the minimization of the nuclear mass for a given number of valence electrons. Consequently, only elements of periods 1 through 4 are applicable, which leaves metals or metalloids. Metals as recyclable electrofuels, which can be reacted or burned with both water and air and are often-overlooked as an energy-carrier. **Figure 1.2** compares the energy density and specific energy of several metal-fuel alternatives to those of fossil and other low-carbon alternatives. Metals, among all fuel options, have the most volumetric heat generation when burned in air, and are therefore the most energetically dense chemical fuels available. Several metal fuel candidates have been proposed and some are currently being investigated as eligible solutions, including Lithium (Li), Boron(B), Magnesium (Mg), Aluminum (Al), Silicon (Si), Iron (Fe), and Zinc (Zn) [8].

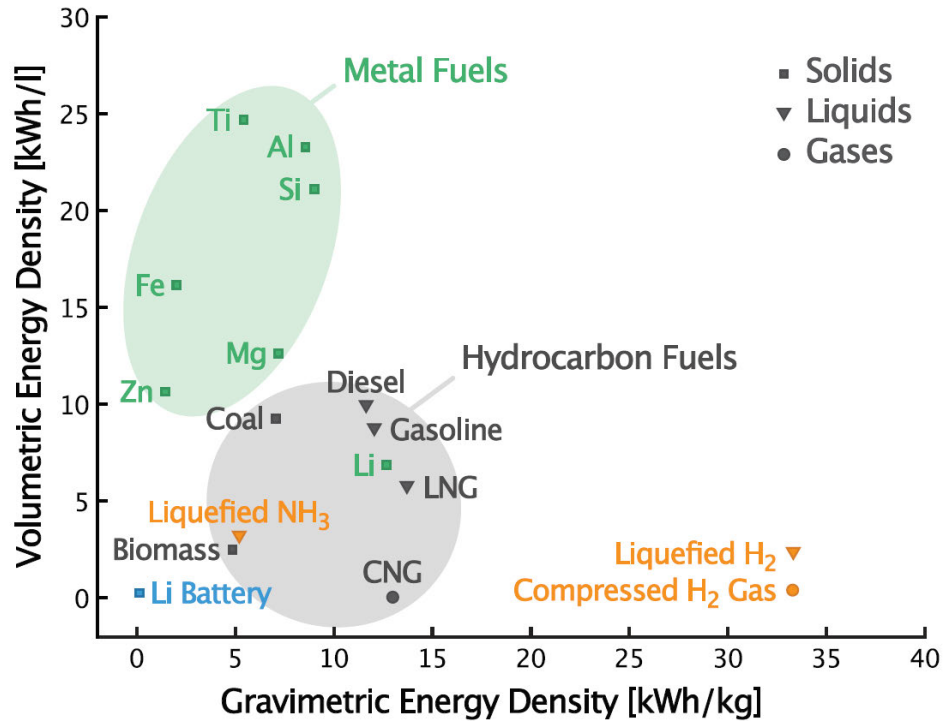


Figure 1.2. Volumetric and Gravimetric Energy Densities of Chemical Energy Carriers

From the perspective of a green metal fuel economy, Iron (Fe) in particular is highly desirable for stationary power generation. It is stable and abundant, has a high volumetric energy density, low toxicity, a cheap market price, and has an existing infrastructure for production and distribution. **Figure 1.3** demonstrates a clean, dry oxidation/reduction cycle for using iron as an energy carrier [8]. At the beginning of the cycle, electricity is produced with iron as a fuel that is burned to release heat during high-temperature oxidation, like the conventional burning of solid fuels. In contrast to burning of fossil fuels, CO₂ is not released during the burning of iron. The combustion products are solid iron oxides (Fe_xO_y), which are easily collected. Iron oxides are stored and transferred to the reduction facilities at the bottom of the cycle. Electrochemical or thermochemical techniques involving renewable energy are employed to chemically

reduce iron oxides. Both approaches regenerate iron fuel for the combustion process without emitting carbon dioxide. When recycled iron fuel is transferred to the thermal power plant and burnt again to generate electricity, a circular energy economy is established.

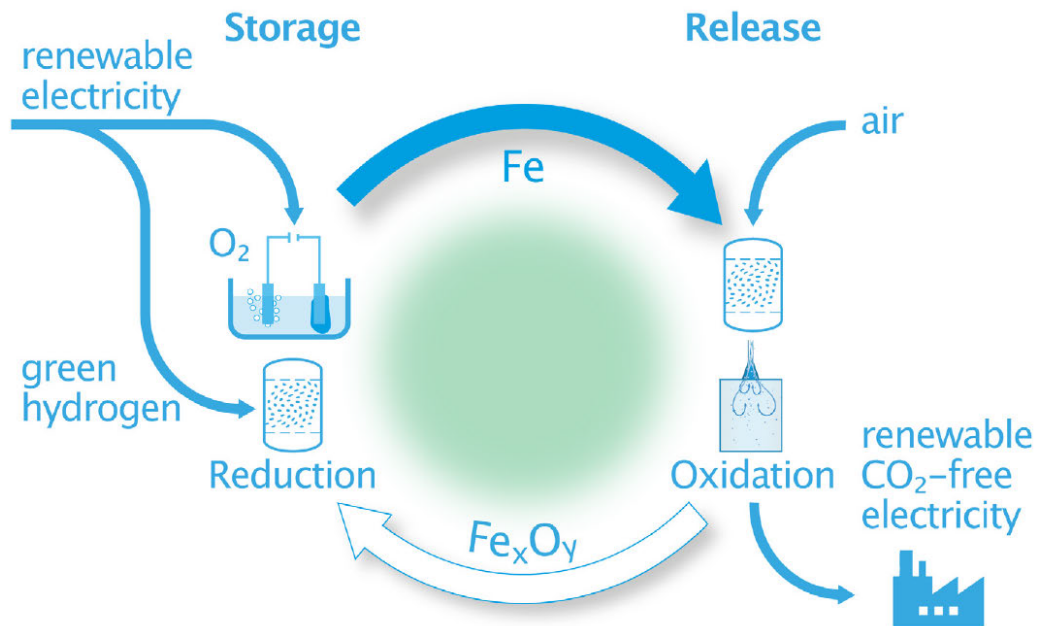


Figure 1.3. Schematics of a CO₂-free Iron Reduction–oxidation Cycle.

The direct reduction of iron (DRI) utilizing green hydrogen as a reducing agent is proposed as one of the most promising routes to carbon neutrality in this energy cycle. Green hydrogen is a type of hydrogen produced using renewable energy sources, such as wind, solar, or hydroelectric power, through the process of water electrolysis. However, green hydrogen production only consists of less than 1% of the total US hydrogen market [9]. Production of hydrogen via other approaches, such as steam methane reforming (counts 75% of the hydrogen market), release greenhouse emissions, making it a less environmentally friendly method compared to green hydrogen.

In addition, the reduction efficiency is significantly hindered by the small equilibrium constant of the reduction of iron oxide using hydrogen at the operating temperature of 1050C. The equilibrium constant for the reaction ($\text{Fe}_2\text{O}_3 + 3\text{H}_2 = 2\text{Fe} + 3\text{H}_2\text{O}$) at 1050°C is approximately 61, indicating that the reaction will stop when 80% of the hydrogen is utilized. The reaction is expected to proceed with Fe_2O_3 first converting to FeO and then further to Fe . In this case, the equilibrium constant for the reaction ($\text{FeO} + \text{H}_2 = \text{Fe} + \text{H}_2\text{O}$) at 1050°C is about 0.77. This means the reaction will stop when 44% of the hydrogen is utilized, leaving 56% unreacted. It is estimated that changing the gas composition from 98% water vapor with 2% hydrogen to 44% water vapor with 56% hydrogen on one side of the electrolyzer and air on the other side may increase the voltage for electrolysis by around 32%. This voltage increase leads to a power consumption of 3.28 kWh/kg Fe. Given that the thermal energy release is 2.05 kWh/kg Fe, increasing the electrolyzer power consumption to that figure would likely result in an overall efficiency of only around 63%.

Lastly, storage and transportation of hydrogen remains a big challenge. Systems that store and transport the gaseous form H_2 require safety precautions to prevent explosion, flashback hazards, and environmental damage. A H_2 -free approach to reduce iron oxide is needed to be compatible with the requirements of higher reduction efficiency and much lower direct and indirect emissions in the iron recovery process.

1.3 SOM Process Overview

1.3.1 Description of the SOM Process

Solid oxide membrane (SOM) electrolysis is a novel method that has been developed and effectively utilized for the extraction of metals or alloys from their oxides. Previous research has established the feasibility of this method in the production of a variety of metals and intermetallic, such as tantalum, titanium, ytterbium, magnesium, and aluminum [10]– [27].

The key components of the SOM electrolytic cell include anode assembly, cathode and electrolyte. The anode assembly consists of a ceramic-based SOM, an anode, and an anode current collector. Ytria-stabilized Zirconia (YSZ) is the common material as the membrane for SOM electrolysis. It exhibits high oxygen ionic conductivity and selectively conducts oxygen ions. Liquid silver is generally selected as the anode because it exhibits excellent electrical conductivity and thermal stability at the temperature of interest. In addition, liquid silver has high oxygen solubility, diffusivity, and wettability with the YSZ membrane.[28] At the anode of the SOM cell, depending on the anode current collector materials, oxygen anions are oxidized to either pure O₂ or CO/CO₂. When a graphite rod is employed as the anode current collector, the oxygen anions are oxidized by the carbon rod to form CO or CO₂. When an inert anode current collector (Strontium-doped Lanthanum Manganite (La_{0.8}Sr_{0.2}MnO_{3-x} or LSM) with Inconel rod), is employed, pure O₂ is produced.

The cathode materials are selected based on the type of the desired metals. The primary selections include:

- 1). An inert metal if the desired metal is produced in the gaseous form and later condensed in a separate container vessel (e.g., Mg (g) produced on a steel cathode.).
- 2) The desired metal itself.
- 3). Another metal if an alloy with that metal is desired.
- 4). Another metal if the desired metal has solubility at the operating temperature but no mutual solubility at lower temperatures that enables separation upon cooling.
- 5). An inert electronic collector.

Mixture of molten fluorides and oxides are commonly employed as the electrolyte, while the feasibility of a molten-salt free electrolytic cell is also explored in this work. In the rest of this dissertation, the SOM process that employs molten salt as the electrolyte is referred to as molten salt-based SOM process, and the SOM process that employs other forms of electrolyte is referred to as molten salt-free SOM process. In the application of molten salt-based SOM electrolytic cell, the salt electrolyte needs to meet several characteristics. It should have high ionic conductivity ($> 2 \text{ S/cm}$), low electronic conductivity ($< 0.2 \text{ S/cm}$), low volatility ($< 1 \mu\text{g/cm}^2\text{-s}$), adequate solubility of Silica ($> 3 \text{ wt.}\%$), low viscosity ($< 0.1 \text{ Pa}\cdot\text{s}$).

1.3.2 Silicon Production via Molten Salt-based SOM Process

In comparison to conventional silicon production methods such as the Siemens process and fluidized bed reactors, molten salt-based SOM process has three significant advantages: it is a single-step operation that consumes less energy and capital, it produces no direct greenhouse gases or halogenated emissions, and yields pure O_2 as a valuable

by-product with an inert anode current collector [11,15, 29, 30]. **Figure 1.4** shows the schematics of the molten salt-based SOM process for silicon production.

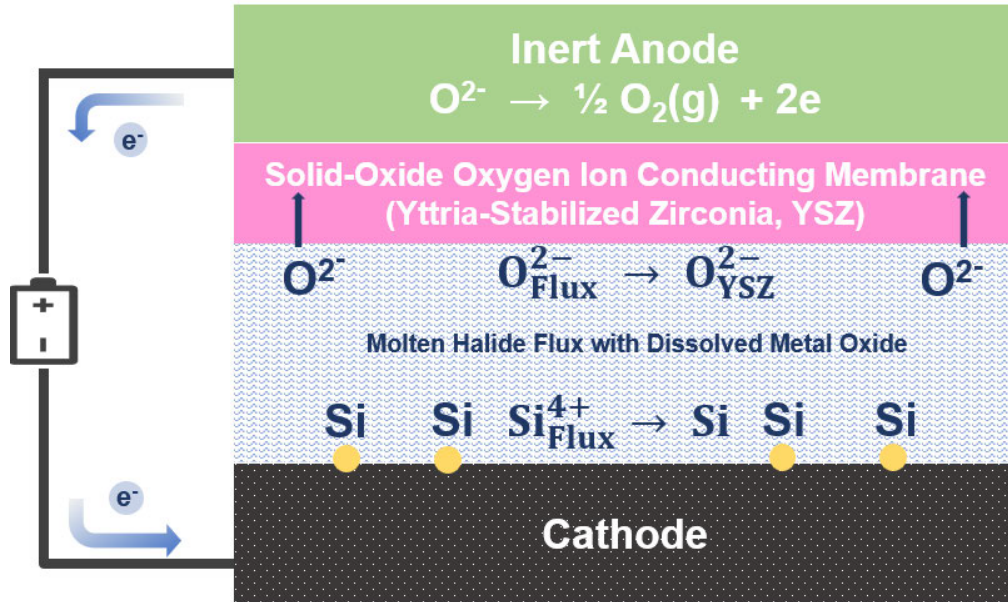
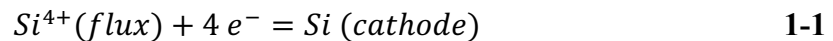
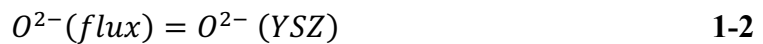


Figure 1.4. Schematics of Molten Salt-based SOM Process for Silicon Production.

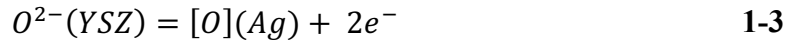
The process of silicon production via molten salt-based SOM electrolysis begins with the dissolution of silicon oxide in the molten salt. An electric potential greater than the disassociation potential of silicon oxide is applied, causing the silicon cations to migrate to the cathode and the oxygen anions to migrate to the anode. When silicon cations reach the cathode, they undergo a half-cell reaction, shown in **Equation 1-1**:



When the oxide ions reach the membrane, they migrate through the YSZ membrane as shown in **Equation 1-2**:



When liquid silver is used as the anode, the oxygen ions are oxidized at the YSZ/liquid silver interface as shown in **Equation 1-3**. Once the silver is saturated with dissolved oxygen, the oxygen evolves as gas, shown in **Equation 1-4**. Thus, pure silicon metal is produced in a single step at the cathode while producing pure oxygen gas as a byproduct at the anode.



Previous studies have demonstrated the production of high purity silicon via the SOM process. Two unique designs of cathode current collector were attempted: one with a liquid tin cathode and one with a solid molybdenum [31]. However, with the liquid tin cathode, an extra step of acid etching is required to extract the high purity silicon deposits from the solidified tin upon cooling. With the solid molybdenum current collector, silicon is produced as molybdenum silicide. This system also has high resistance, which is detrimental for long-term operation. Therefore, it is necessary to develop a stable, removable, and efficient cathode assembly. The ideal cathode assembly should consist of:

- 1) A cathode current collector that is thermally and chemically stable in the SOM environment while staying mechanically intact with the cathode. It should also have low electrical resistance in contact with the cathode.
- 2) A cathode that can collect Silicon deposits that is reduced from silica in the salt electrolyte and is free of other chemical impurities. It should also be able to completely separate from the flux after the experiment.

1.3.3 Molten Salt-free SOM Process as A Proposed Approach for Iron Recovery

Since the SOM process can effectively extract metals from their oxides, it is a promising process to recover iron from iron oxide in the iron oxidation/reduction cycle when iron is used as the electrofuel. This electrolytic approach is featured by its high reduction efficiency. With an applied potential of 2 V, the power consumption is 2.87 kWh/kg Fe. The reduction efficiency is calculated to be 71% given that the thermal energy release of iron oxide is 2.05 kWh/kg Fe. In addition, the SOM process does not require H₂ or other reducing agents, and it emits zero greenhouse gases with the incorporation of an inert anode and anode current collector.

In this work, a proof-of-concept molten-salt free SOM process is developed and implemented for the recovery of iron from iron oxide. **Figure 1.5** shows the schematics of the molten salt-free SOM process for iron production.

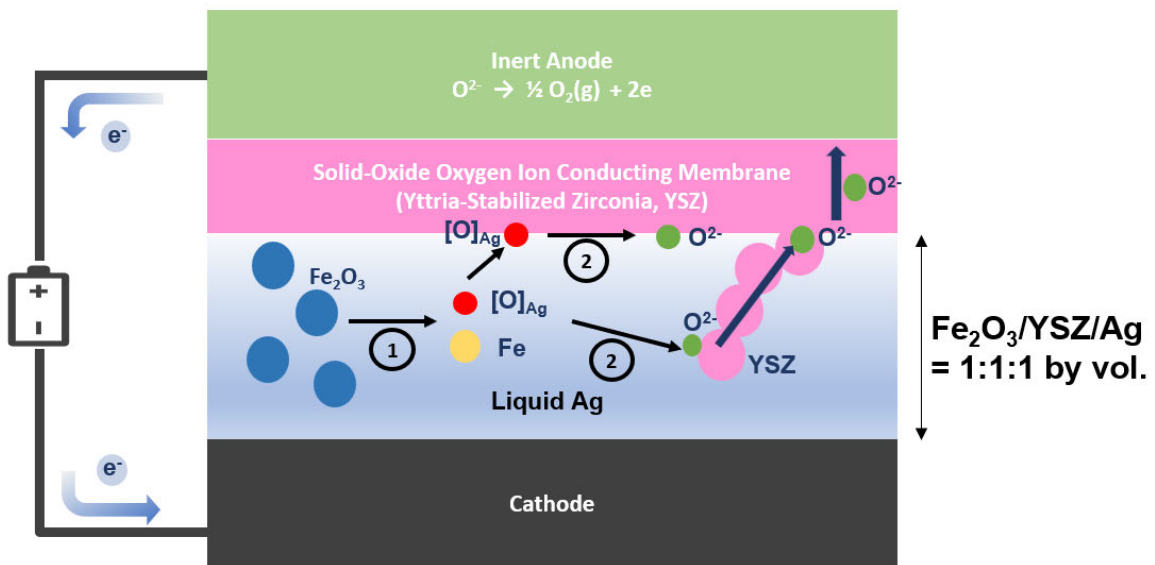
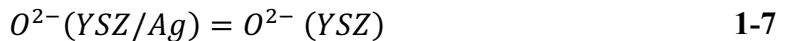


Figure 1.5. Salt-Free SOM Process for Iron Oxide Reduction with YSZ and Silver as the Reducing Medium

Equal volume of iron (III) oxide, silver and YSZ powders are contained within a one-end closed YSZ tube. When an electrical potential greater than the disassociation potential of iron (III) oxide is applied across the YSZ tube with a system of electrodes, iron oxide is dissociated into iron (Fe) and soluble oxygen in Ag ($[O]_{Ag}$) [28, 32]. Oxygen can migrate through the silver to the YSZ membrane and undergoes a reduction to O^{2-} at the silver/YSZ membrane interface. Another possible pathway is that soluble oxygen is reduced to O^{2-} at the silver/YSZ particle interface within the electrolyte. The oxygen ions formed at this interface can migrate through interconnected YSZ particles within the electrolyte to the silver/YSZ membrane interface. Overall, the half-cell reactions at the cathode can be expressed as follows:



When the oxide ions reach the YSZ membrane, they migrate through the membrane as shown in **Equation 1-7**:



Similar to the anode reaction in the SOM process for silicon production, when liquid silver is used as the anode, the oxygen ions are oxidized at the YSZ/liquid silver interface as shown in **Equation 1-3**. Once the silver is saturated with dissolved oxygen, the oxygen evolves as gas as per **Equation 1-4**. The reduced iron powders can be separated from the silver and YSZ using a magnet since ferric iron is immiscible with non-ferric silver and YSZ.

1.4 Research Scope

In the previous section, current status and challenges for silicon production and the conceptual use of iron as a sustainable energy carrier have been reviewed. The increasingly growing global energy demand is driving the development of energy-efficient and environmental-friendly processes for both silicon production and iron recovery. Therefore, the main objectives of this dissertation are:

- 1). To investigate and develop a molten salt-based SOM process that enables efficient production and collection of high-purity silicon.
- 2) To demonstrate the feasibility of a molten salt-free SOM process that enables efficient recovery of iron from iron oxide.

The dissertation is divided into 6 chapters. Chapter 1 outlines the need of developing energy-efficient and environmental-friendly processes for silicon production and iron recovery. Chapter 2 describes the design and assembly of molten salt-based Si-SOM electrolytic cell and molten salt-free Fe-SOM electrolytic cell. It also entails the materials selection of cell components and experimental procedure of operating Si- and Fe-SOM electrolysis. Chapter 3 describes the optimization process of Si-SOM electrolysis. Initially, some challenges were encountered in obtaining pure silicon. To address these issues, a systematic approach was adopted, involving initial formulation of failure mode hypotheses, thermodynamic simulations, and comprehensive microstructural characterization of relevant cell components. Chapter 4 details the electrochemical and post-experimental characterization of the Si-SOM electrolysis, with the discussion of periodic potential switch that aims to facilitate epitaxial growth of

Silicon. Chapter 5 details the electrochemical and post-experimental characterization of the Fe-SOM electrolysis. Chapter 6 summarizes the findings and gives suggestions for future work.

2. SOM CELL DESIGN AND ENGINEERING

Each component of a SOM cell was chosen for its compatibility with others and maximal electrolytic efficiency when the cell is in operation. Furthermore, each component needs to be stable in the surrounding chemistries. In general, a SOM cell consists of three key components: cathode assembly, anode assembly, and the electrolyte. In this chapter, the design criteria of each component will be reviewed for both Si-SOM and Fe-SOM cell. Initial materials selections and preparation of each component are specified. It should be noted that some cell components were later adjusted to eliminate the impurities in the deposits and optimize the cell efficiency. These changes are further detailed in Chapter 3 and Chapter 5.

2.1 Si-SOM Cell Design and Engineering

2.1.1 Cell Design and Engineering: Cathode, Anode and Current Collectors

In this work, polycrystalline silicon wafer was chosen as the cathode because it provides natural starting seeds for any Silicon deposits produced during SOM electrolysis. In addition, after the SOM electrolysis, no extra steps are required to extract the Si deposits. The extraction of silicon deposits can be easily accomplished by mechanically detaching the cathode from the cathode current collector, given that the silicon deposits maintain strong adherence to the cathode. A graphite rod was first employed as the cathodic current collector due to its high electrical conductivity at elevated temperatures, chemical stability in contact with the flux, and good machinability. These attributes allow it to have a secure connection and contact with the Si wafer cathode. Thus, the initial setup for a Si-SOM cell incorporates a silicon (1 0 0)

wafer as the cathode, and a graphite rod which acts as the cathode current collector. The Si wafer is attached to the graphite rod by Aremco Graphi-Bond High Temperature Graphite Paste.

Using prior SOM studies as a guide, an anode with a YSZ membrane that encapsulates a liquid silver pool was constructed [11-15]. Silver was used as an anode due to its high electrical conductivity and oxygen diffusivity, stability in contact with the SOM, and ability to oxidize the oxygen ions without forming an oxide phase. A graphite rod was used as the anode current collector, for ease of operation and to demonstrate process feasibility. The oxygen created at the anode reacts with the carbon to form carbon monoxide (CO), overall reaction shown in **Equation 2-1**.



Combining **Equation 2-1** and **Equation 1-1** to **1-4**, the overall electrolysis reaction for this particular SOM process can be written as **Equation 2-2**.



Equation 2-3 shows that the disassociation potential is proportional to the Gibbs free energy.

$$\Delta G = -nFE \quad 2-3$$

where ΔG is the change in Gibbs free energy ($J * mol^{-1}$); n is the number of electrons transferred during the electrolysis process (mol); F is Faraday's constant ($96485 C * mol^{-1}$); and E is the applied potential ($J * C^{-1}$).

The standard disassociation potential of Silica and other major oxides with carbon at $1100\text{ }^\circ\text{C}$ are listed in **Table 2.1**.

	ΔG (kJ/mol)	n	E(V)
Fe_2O_3	-232.052	6	-0.401
CrO_2	-133.155	4	-0.345
FeO	-58.56	2	-0.303
Cr_2O_3	79.58	6	0.137
MnO	50.267	2	0.262
B_2O_3	240.861	6	0.416
SiO_2	200.436	4	0.519
Al_2O_3	539.007	6	0.931
ZrO_2	374.631	4	0.971
MgO	217.542	2	1.127
CaO	256.313	2	1.328
Y_2O_3	810.896	6	1.401

Table 2.1. Standard Dissociation Potential of Silica and Other Major Oxides with A Graphite Anode Current Collector at 1100 C.

In order to reach zero direct carbon emission, an inert anode current collector is also employed. One option is to employ the LSM ($\text{La}_{0.8}\text{Sr}_{0.2}\text{MnO}_{3-\delta}$)–Inconel Inert Anode Current Collector, suggested and verified in a previous study [11]. A schematic of this SOM anode current collector configuration can be found in **Figure 2.1**. This current collector consists of a sintered LSM bar, an Inconel alloy rod, an alumina sheath, a mixture of alumina pastes and LSM powders and a liquid silver contact. LSM was chosen as the inert anode current collector in SOM experiments due to its high-temperature tolerance, resistance to oxidation while maintaining good electronic conductivity at high temperatures. The Inconel alloy 601 rod was selected for its excellent resistance to high-temperature oxidation and consistent conductivity across a wide range of temperatures. The use of liquid silver ensures proper wetting and electrical connection between the LSM bar and the Inconel rod. To protect the Inconel rod from

oxidation in the high-temperature oxygen environment, an alumina sheath is employed. Additionally, a combination of alumina and LSM powders forms a tight seal that prevents oxygen from entering the alumina sheath.

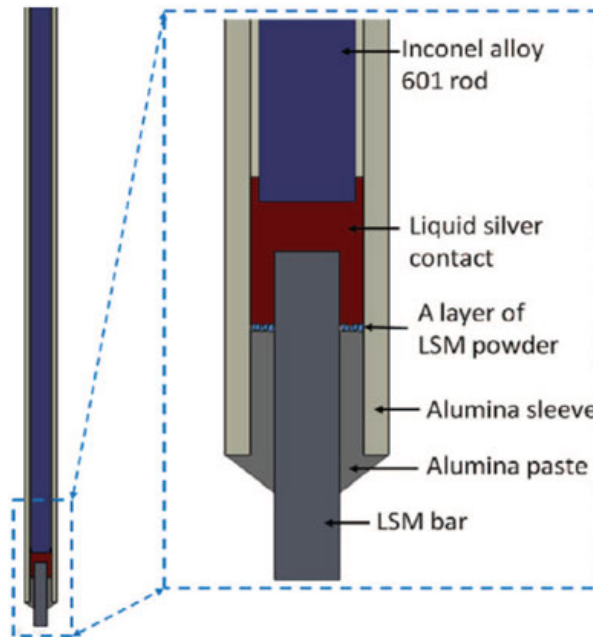


Figure 2.1. Schematics of the LSM-Inconel Current Collector

When an inert anode current collector is employed, the oxygen created at the anode is stable and exit at the top of the anode assembly. Combining **Equation 1-1** to **1-4**, the overall electrolysis reaction instead can be written as **Equation 2-5**.



Equation 2-5 can be used for SOM cells producing O_2 gas at the anode and the standard disassociation potential of Silica and other major oxides at 1100 °C can be determined from the free energy of formation of the oxide; values are listed in **Table 2.2**.

	delta G (kJ)	n	delta E (V)
Fe ₂ O ₃	466.493	6	0.805
CrO ₂	332.542	4	0.861
FeO	881.526	10	0.914
Cr ₂ O ₃	778.125	6	1.344
MnO	283.475	2	1.469
B ₂ O ₃	939.406	6	1.622
SiO ₂	666.133	4	1.726
Al ₂ O ₃	1237.552	6	2.138
ZrO ₂	840.328	4	2.177
MgO	450.39	2	2.334
CaO	489.1615	2	2.535
Y ₂ O ₃	1509.441	6	2.607

Table 2.2. Standard Dissociation Potential of Silica and Other Major Impurities with an inert anode current collector at 1100 C.

2.1.1 Electrolyte Design – Base Electrolytes

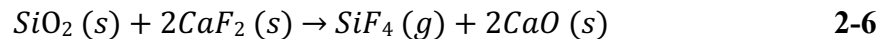
As previously discussed in Section 1.3, the flux electrolyte used in the molten salt-based SOM process needs to meet several characteristics to enable an efficient and stable electrolysis. The flux electrolyte of Si-SOM electrolysis should have high ionic conductivity (> 2 S/cm), low electronic conductivity (< 0.2 S/cm), low volatility (< 1 $\mu\text{g}/\text{cm}^2\text{-s}$), adequate solubility of Silica (> 3 wt.%), low viscosity (< 0.1 Pa-s). CaF₂ and MgF₂ were chosen as the base salts for the following reasons [33, 34]:

- High melting point: Both CaF₂ and MgF₂ have relatively high melting points, which makes them suitable for high-temperature applications such as the SOM process.
- Ionic conductivity: These fluorides can exhibit high ionic conductivity when molten, allowing for the transport of ions within the electrolyte. This property is crucial for the efficient functioning of an electrolysis process.

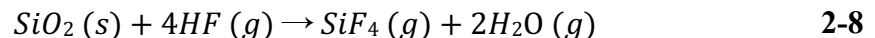
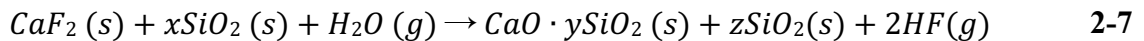
- Stability: CaF₂ and MgF₂ are chemically stable at high temperatures and in the presence of oxygen. This stability is important to maintain the integrity of the electrolyte during the electrolysis process.
- Low viscosity: Both CaF₂ and MgF₂ exhibit relatively low viscosities at high temperatures. Lower viscosity can facilitate the movement of ions, enhance mass transfer, and improve overall system efficiency.

Once the base eutectic was chosen, the investigation focused on the stability and solubility of the Silica in the flux. Previous study has revealed that Silica can leave the system by two mechanisms, shown in **Equation 2-6** and **Equation 2-7** to **Equation 2-8** respectively[35-38]:

High Temperature Reaction:



Water-driven Reaction:



To prevent the water-driven reaction, a moisture-free experiment environment is needed. Elimination of water in the system is achieved by:

- 1) All fluoride and oxide powders are dried prior to mixing.
- 2) The flux is baked at 400 C prior to any melting or electrolysis.
- 3) Forming gas is passed through a moisture trap filled with drierite.

To prevent the high temperature reaction, CaO is added to the flux and melts with CaF₂ and MgF₂ prior to addition of SiO₂. By lowering the activity of calcium fluoride and

increasing the activity of CaO, the equilibrium constant for **Equation 2-6** can be increased until the overall reaction is suppressed with a positive Gibbs Free Energy.

2.1.3 Electrolyte Design – Stability with YSZ membrane

Another critical requirement for the SOM flux is that the flux should have high chemical stability in contact with the YSZ membrane (in other words, the degradation rate of the membrane should be less than 0.1 $\mu\text{m}/\text{hour}$.) Previous research has revealed that the degradation of the YSZ membrane is caused by two mechanisms. One mechanism is the imbalance in Yttria activity between the flux and the membrane. When the Yttria activity in the flux is lower than that in YSZ, Yttrium can diffuse from the high activity phase to the low activity phase. This can result in the formation of cracks and the penetration of the flux into the membrane when Yttrium is lost from the 6-mol% Yttria Stabilized Zirconia (6YSZ) membrane. As a result, the diffusion distance for Yttrium to reach the liquid flux is reduced, leading to faster Yttrium dissolution and increase in thickness of the yttrium depletion layer to hundreds of microns. On the other hand, when the Yttria activity in the flux is slightly higher than in YSZ, Yttrium diffuses into the solid YSZ but no crack formation or flux penetration occur. The yttrium enrichment layer in the YSZ is generally only a few micrometers. Therefore, in order to prevent this outward diffusion from the YSZ membrane to the flux, more than 2wt% of YF₃ is required in the flux.

Second mechanism is the grain boundary attack caused by the interaction between basic Yttria in the YSZ and acidic Silica network in the flux. This attack only happens when the optical basicity of the oxides in the molten flux is lower than that of the Yttria

in the YSZ membrane. Optical basicity refers to the ability of an oxide or fluoride compound to act as a Lewis base and donate electrons in electronic transitions involving the absorption or emission of light. It is a measure of the basicity of the oxide or fluoride and its ability to interact with excited states. Oxides and fluorides can exhibit a range of optical basicities depending on the nature of the metal cation and the coordination environment around the cation, shown in **Table 2.3** [39, 40].

Compound	CaO	SiO ₂	ZrO ₂	Y ₂ O ₃	MgF ₂	CaF ₂
Optical Basicity (Λ)	1.0	0.48	0.71	0.72	0.34	0.43
Oxidation State (n)	+2	+4	+4	+3	+2	+2

Table 2.3. Optical Basicity of Major Oxides and Fluorides in the SOM environment

Previous study has revealed that YSZ degradation is mitigated by balancing the optical basicity of the oxides in the flux to that of Ytria within the YSZ membrane [34]. It was also observed that the optical basicity of the fluorides did not exert any significant influence on the degradation of the YSZ. The exact reason behind this phenomenon remains unclear. To estimate the optical basicity of the oxide, Duffy's optical basicity model for multiple oxides system is used, shown in **Equation 2-9**.

$$\Lambda = \frac{X_1 n_1 \Lambda_{th,1} + X_2 n_2 \Lambda_{th,2} + \dots}{X_1 n_1 + X_2 n_2 + \dots}, \quad \mathbf{2-9}$$

where Λ is the optical basicity of the oxide system; Λ_{th} is the optical basicity of individual oxides; X is the mole fraction of each individual oxide; and n is the cation oxidation state of individual oxides.

As only CaO and SiO₂ are present in the flux, this model is further simplified to a function of the ratio of mole fractions of CaO and SiO₂, shown in **Equation 2-10**.

$$\Lambda = \frac{X_{CaO}n_{CaO}\Lambda_{CaO} + X_{SiO_2}n_{SiO_2}\Lambda_{SiO_2}}{X_{CaO}n_{CaO} + X_{SiO_2}n_{SiO_2}} = \frac{\frac{X_{CaO}}{X_{SiO_2}} + 0.96}{\frac{X_{CaO}}{X_{SiO_2}} + 2} \quad \mathbf{2-10}$$

Based on this simplified model, The optical basicity of the flux can be adjusted by altering the ratio between the acidic SiO₂ and basic CaO. When the optical basicity of the flux is lower than that of the Yttria in the YSZ membrane, Silica network in the flux reacts with the YSZ grain boundaries. This reaction attracts oxygen ions from the Yttria at the grain boundaries, causing Yttrium ions to be incorporated into the flux.

Consequently, the Yttria concentration decreases within the 6YSZ grains, creating a concentration gradient between the bulk of the grain and the grain boundary. This leads to the diffusion of Yttria from the bulk to the grain boundary, resulting in the conversion of partially stabilized 6YSZ to tetragonal 2YSZ within the YDL (Yttria Depletion Layer). The formation rate of the YDL depends on the rate at which the Silica in the flux attacks the grain boundaries, which is influenced by the concentration of unnaturalized Silica in the flux. Once the optical basicity of the flux matches that of the Yttria, the YSZ membrane is protected from grain boundary attack and the subsequent formation of the YDL. Therefore, to counter the imbalance of the optical basicity between the flux and that of Yttria, a flux with 5.8 mol % Silica (5 weight%) should contain at least 10 mol% CaO (9 weight%) [34]. Overall, to minimize concentration polarization losses and prevent any damage to the SOM membrane, a eutectic CaF₂-MgF₂ flux with 5wt% SiO₂, 9wt% CaO, and 4wt% YF₃ is proposed for the initial SOM electrolysis experiments.

2.1.4 Electrolyte Preparation

During the initial stage of the SOM experiments, the electrolytic flux is prepared as follows. The fluoride and calcium oxide powders were thoroughly dried for six hours at a temperature of 400 °C inside a Carbo-lite RHF 1600/3 box furnace. They were then mixed in the appropriate ratios and ball milled for six hours at a rate of 120 rpm. The milling process employed glass balls with 1 cm in diameter, which guarantees that only Silica could possibly get introduced into the flux mixture.

The flux mixture was then put into a graphite crucible and was pre-heated to 1150 °C for 2 hours under a forming gas environment. This initial heating phase is critical in inhibiting the formation of silicon tetrafluoride gas (SiF_4). After this, the pre-melted flux was crushed and mixed with silicon oxide.

The combined flux and silicon oxide were then heated once more in a graphite crucible to 1150 °C, maintaining the forming gas environment, and held at this temperature for another 2 hours. After the flux cooled, the carbon on its surface from the graphite crucible was removed by grinding. The fluoride-oxide mixture was then ready for use in the SOM experiment.

It should be noted that in subsequent SOM experiments, several components of the SOM cell and procedures are changed for better cell performances. Therefore, the preparation of the electrolyte is adjusted based on those changes, which will be detailed in Chapter 3 and 4.

2.2. Fe-SOM Cell Design and Engineering

2.2.1 Cell Design and Engineering: Cathode, Anode and Current Collectors

An Iron rod was used as the cathode and current collector. In a reducing environment at high temperatures, an Iron rod exhibits good electrical conductivity and are stable with molten Silver that is present in the electrolyte compact and reduced Iron deposits. Shown in **Figure 2.2**, Iron and Ag are immiscible at the experiment temperature (1100 C) [41]. In addition, by using an Iron cathode, the freshly reduced Iron atoms can deposit directly onto the existing Iron cathode.

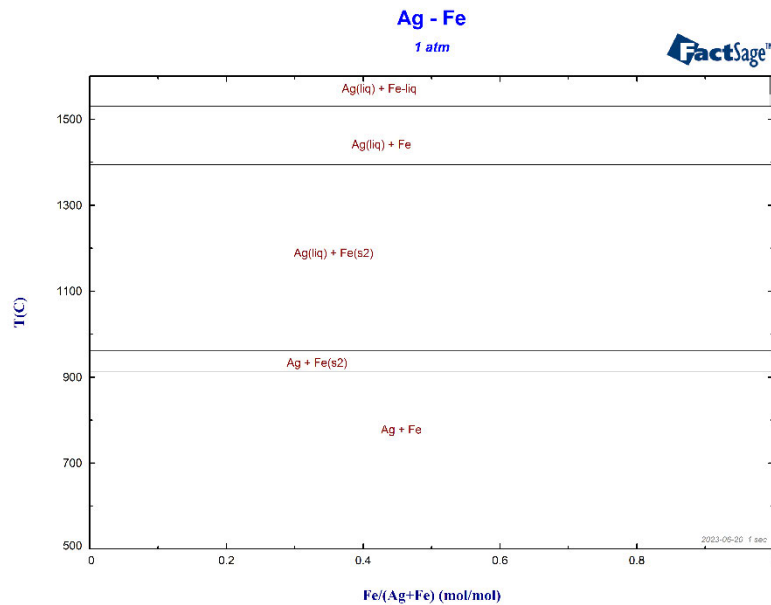


Figure 2.2. Ag-Fe Phase Diagram

Similar to the Si-SOM cell, Silver was also used as an anode because it has excellent electrical conductivity and chemical stability in oxygen that is produced at the anode. YSZ membrane was used to separate the silver anode and electrolyte. Due to its high oxygen ion conductivity, it can effectively transport oxygen ions during the

electrolysis. Low-carbon steel crucible was used to contain the silver pool and connect the anode and anode current collector. It exhibits high mechanical strength, electrical conductivity, and stability with other cell components at high temperatures. These attributes allow it to have excellent electrical connection, durability, and structural support in the cell. Inconel rod was selected as the anode current collector. While Inconel's electrical conductivity is lower than materials like pure nickel, its high corrosion resistance and mechanical strength at high temperatures makes it an excellent choice as an anode current collector.

Overall, the anode assembly of the Fe-SOM cell incorporates a silver pool as the anode, YSZ membrane that conducts oxygen ions from the cathode to anode, steel crucible that contains silver pool and Inconel rod as the anode current collector. To maintain an initial oxygen-free environment on the anodic side for efficient electrolysis, 200 sccm argon gas is passed through an oxygen trap filled with heated copper chips. The schematics of the Fe-SOM cell is shown in **Figure 2.3**.

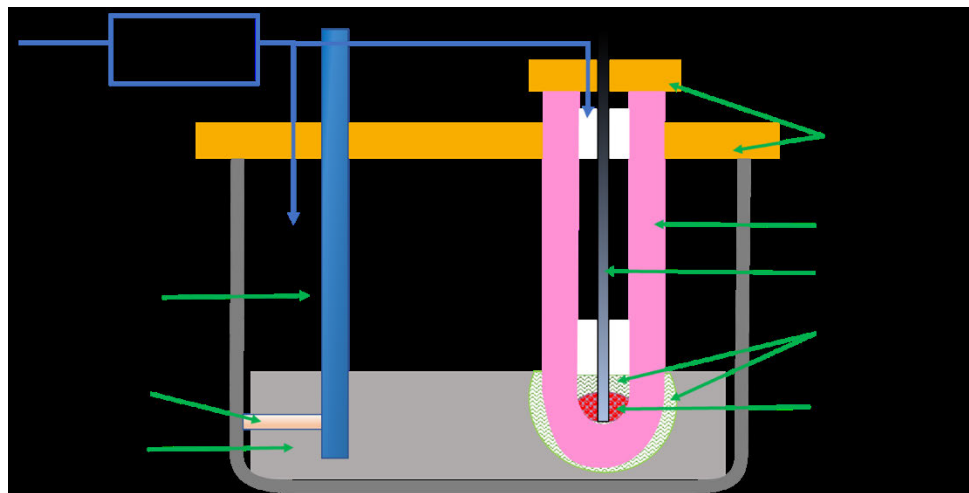


Figure 2.3. Schematics of the Fe-SOM Cell Setup.

2.2.2 Electrolyte Design

Efficient electrolytes for the Fe-SOM electrolysis should meet several criteria to ensure effective and sustainable Iron production. It should have high oxygen diffusivity and high physical and chemical stability with the chosen cathode, anode materials and YSZ membrane. The electrolyte should be able to be effectively separated from the Iron deposits and recycled for multiple experiments. Based on those criteria, a mixture of silver and YSZ was selected as the base electrolyte for the following reason:

- Fast oxygen transport: silver exhibits relatively good oxygen diffusivity at high temperatures ($D = 3 \times 10^{-4} \text{ cm}^2/\text{s}$ at 1100 C) [28]. When the dissociation of iron oxide occurs, oxygen from the iron oxide forms soluble oxygen in the silver and diffuses through liquid silver. At the same time, oxygen from iron oxide may undergo reduction at the YSZ/silver interface, allowing oxygen ions to migrate through the YSZ lattices. Because of high concentration of oxygen vacancies in YSZ lattice, YSZ exhibits excellent oxygen ion conductivities ($\sigma_{ion} = 0.3 \text{ S/cm}$ at 1100 C) [42]. Therefore, fast oxygen transport should occur through diffusion of atomic oxygen within the silver or ionic conduction of oxygen in the YSZ lattices.
- Compatibility with cathodes and YSZ membrane: Both YSZ and Ag are stable with the Fe cathode and YSZ membrane. As indicated from **Figure 2**, Ag does not alloy with Fe, which ensures good electrical contact and electrode stability.

- Cost-effectiveness: Although the use of Silver and YSZ (Yttria-stabilized zirconia) can be costly, the overall cost of the Fe-SOM cell is relatively affordable. By employing a magnet, the reduced Iron particles can be separated from a mixture containing ferromagnetic Iron, non-ferric Silver and ceramic YSZ. This suggests that recycling of the Silver and YSZ is possible, leaving the reducing Iron Oxides as the only consumable in this electrolytic process.

2.2.3 Electrolyte Preparation

To enhance the interfacial contact between Iron Oxide, Silver and YSZ, a compact that consists of those materials was constructed. The powders are combined in a 1:1:1 volume ratio, mixed with 6.5mm YSZ balls, and ball milled in ethanol for 6 hours. After sieving to remove the balls, the powder is dried overnight. The dried powder is then transferred to a die to form a compact. To ensure a smooth release of the compact from the die, the internal surfaces of the die are applied with lubricant before adding the powder. After the compact is compressed in a hydraulic press at a pressure of 8 tons of force for at least 5 minutes, it is unloaded and broken into small granules that are ready for the electrolysis.

2.3 Summary

In this chapter, the design and engineering of the Si-SOM and Fe- cells are discussed. Each component of the cell, including the cathode assembly, anode assembly, and electrolyte, are chosen based on compatibility, electrolytic efficiency, and specific characteristics required by their surrounding chemistries.

For the Si-SOM cell, a polycrystalline silicon wafer is selected as the cathode due to its ability to serve as a starting seed for silicon deposits and ease of extraction. A graphite rod is used as the cathodic current collector for its high electrical conductivity, chemical stability, and machinability. Silver is employed as the anode material, as it exhibits excellent electrical conductivity and chemical stability with oxygen gas evolution. The anode current collector can be a graphite rod or an LSM-Inconel inert anode current collector. The electrolyte consists of a eutectic $\text{CaF}_2\text{-MgF}_2$ flux with 9% CaO and 4% YF_3 and 5 wt% SiO_2 to meet the stability criteria with respect to the YSZ membrane.

In the Fe-SOM cell, an Iron rod is chosen as both the cathode and current collector due to its electrical conductivity, stability, and compatibility with the molten silver electrolyte. Silver is used as the anode material, and a YSZ membrane separates the anode from the electrolyte. A steel crucible containing the silver pool and an Inconel rod as the anode current collector complete the anode assembly. The electrolyte comprises a mixture of Silver and YSZ, providing fast oxygen transport and compatibility with the cathode and YSZ membrane.

3. OPTIMIZATION PROCESS OF SILICON-SOM ELECTROLYSIS

3.1 Introduction

This chapter provides an overview of the three major obstacles encountered during the deposition of high-purity Silicon employing the SOM electrolysis cell and the steps taken to overcome the challenges to get better quality deposits.

The first challenge was thinning of the Si wafer cathode. When the Silicon wafer cathode was removed from the flux after few initial SOM electrolysis trials, the Si wafer cathode experienced thinning due to oxidation. The second challenge involved observing impurities such as carbon (C) and zirconium (Zr) in the Silicon deposits. The third challenge was the existence of a Si-Mg-O in the Si deposits.

The optimization process to overcome these challenges was carried out employing a systematic approach. It involved the initial formulation of failure mode hypotheses, thermodynamic simulations, and comprehensive microstructural characterization of relevant cell components. These investigations were followed by a series of validation experiments to confirm the proposed theories and assess the effectiveness of the implemented changes. To address the challenge of Si cathode thinning, appropriate experiments were designed based on initial observations, followed by demonstration of the underlying mechanisms. After conducting each Si cathode stability experiments, cross section of Si cathode was thoroughly characterized under Scanning Electron Microscopy (SEM) to identify any signs of oxidation or dissolution into the flux. Similarly, for the elimination of carbon and zirconium impurities, appropriate experiments were designed and conducted. Post-experimental microstructural analysis of the interfaces between the

cathode and the electrolytic flux, as well as between the YSZ membrane and the flux, was conducted. By examining the interfaces, the origin and mechanisms of the incorporation of the impurities were revealed. Finally, in the case of the Si-Mg-O phase formation, thermodynamic analysis and experimental observations were combined to propose a mechanism. This approach ensured a thorough understanding of each issue and helped in mitigating these challenges and optimize the Si-deposition process.

3.2 Si-SOM Cell Electrolysis with Initial Setup

An initial laboratory-scale proof-of-concept Si-SOM electrolysis experiment was conducted using the setup shown in **Figure 3.1**. To maintain a reducing atmosphere, a graphite crucible was heated to 1150°C in the presence of a gas mixture consisting of 95% argon and 5% hydrogen. The graphite crucible contained 450g of powdered flux with a eutectic CaF₂-MgF₂ mixture containing 5wt% SiO₂, 9wt% CaO, and 4wt% YF₃.

A one-end closed 8 mol% Yttria Stabilized Zirconia (YSZ) tube separated the flux from 5g of liquid silver contained within the YSZ tube. To extend the YSZ tube out of the reactor an alumina tube was connected using gas-sealing ceramic paste (Aremco v552). A graphite rod anode current collector was submerged in the liquid silver within the YSZ membrane tube at the desired temperature. A digital mass flowmeter was connected to the exit of the anode assembly, which recorded the flowrate of the evolving anodic gas during electrolysis.

On the cathode side, a slit was cut at the end of the graphite rod, and a silicon wafer was inserted and attached using graphite paste (Resbond 931). During the electrolysis, the Silicon cathode wafer was partially immersed into the flux. Before and

after the electrolysis, two tungsten reference electrodes were inserted into the molten flux to monitor any changes of electrolytic properties of the flux. To ensure homogeneity of the molten flux and minimize concentration polarization at the Si wafer cathode, a stainless-steel bubbling tube was immersed in the flux during the electrolysis. Argon was flowing through this bubbling tube. The entire cell was operated in a vertical tube furnace with the SOM cell positioned at the center of the heating zone.

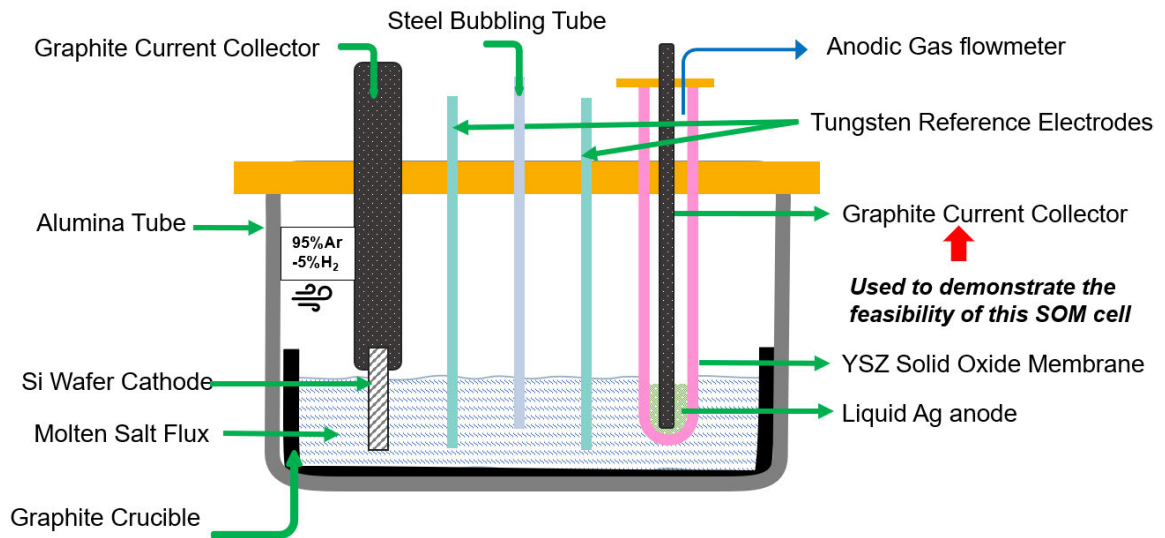


Figure 3.1. Schematics of the initial Si-SOM Cell Experimental Setup.

3.3 Silicon Cathode Stability Analysis

3.3.1 Initial Observation of Silicon Wafer Thinning

After conducting the initial SOM electrolysis trials, the section of the Si wafer cathode that was immersed in the flux during the electrolysis process underwent some degree of oxidation or thinning. To determine its exact thickness, the Silicon cathode was sectioned, mounted in epoxy, and characterized under SEM. **Figure 3.2** shows the cross

section of the interface between Silicon cathode and flux after one initial SOM electrolysis trial. The as-received Si wafer had an initial thickness of 500 μm , whereas the post-electrolysis Si wafer exhibited a reduction of thickness ranging from 150 to 160 μm . The thinning of the Silicon wafer became more significant as the Silicon wafer approached the flux-gas interface. In other words, there appeared to be a direct relationship between the reduction in thickness and the immersion depth of the Silicon wafer cathode in the flux. To understand this observation a series of experiments were conducted to investigate the effect of the immersion depth on Silicon wafer thinning.

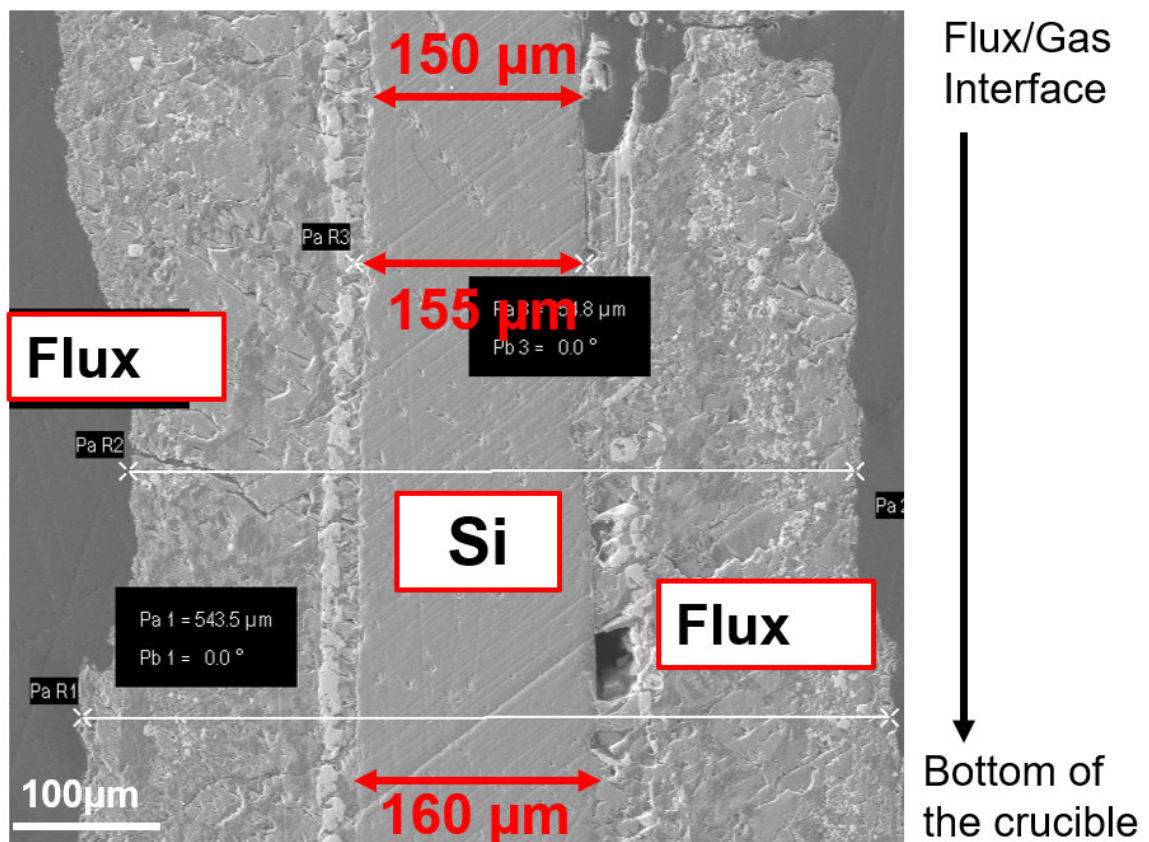

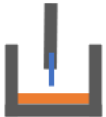

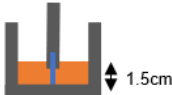
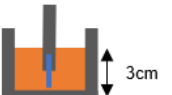


Figure 3.2. A SEM image of the interface between Silicon Cathode and the flux after the electrolysis

3.3.2 *Silicon Wafer Stability Experiment Setup and Observations*

Under a reducing atmosphere that consists of 95% Argon and 5% Hydrogen, the graphite current collector and Silicon wafer cathode were heated to 1150°C and immersed at different depths in the flux for a duration of 6 hours. The flow rate of forming gas was set to 50 sccm. Additionally, a test was conducted where the cathode current collector with the silicon wafer was positioned above the flux for the same duration of 6 hours to observe the effect of trace amounts of Oxygen on the oxidation behavior of the silicon wafer. After completing these tests, the silicon wafer was removed, sectioned, and mounted in epoxy for microstructure evaluation using a Zeiss Supra 55 Scanning Electron Microscope (SEM) equipped with an Energy Dispersive X-ray Spectroscopy (EDS) analyzer. **Table 3.1** summarizes the schematics and post-experimental observations of each experiment.

Ex #	Description	Schematics	Observation
1	As received		507 μm
2	Above the flux		505 μm
3	Partially immersed in flux		155 μm
4	Completely immersed 1.5 cm deep in flux		367 μm
5	Completely immersed 3 cm deep in flux		502 μm

Note: Experiment 2 to 5 were all conducted in a reducing environment at 1100 C for 6 hrs.

Annotation:




Table 3.1. Descriptions, Schematics and Observations of Si wafer Stability Experiment

A detailed microstructural analysis of each silicon wafer in different experiments is shown in **Figure 3** to **Figure 7**. Initially, a pristine silicon wafer was sectioned and mounted at room temperature to determine its thickness. SEM/EDS analysis revealed that the as-received Silicon wafer had a thickness of 507 μm , with no visible silicon oxide layer (**Figure 3.3**).

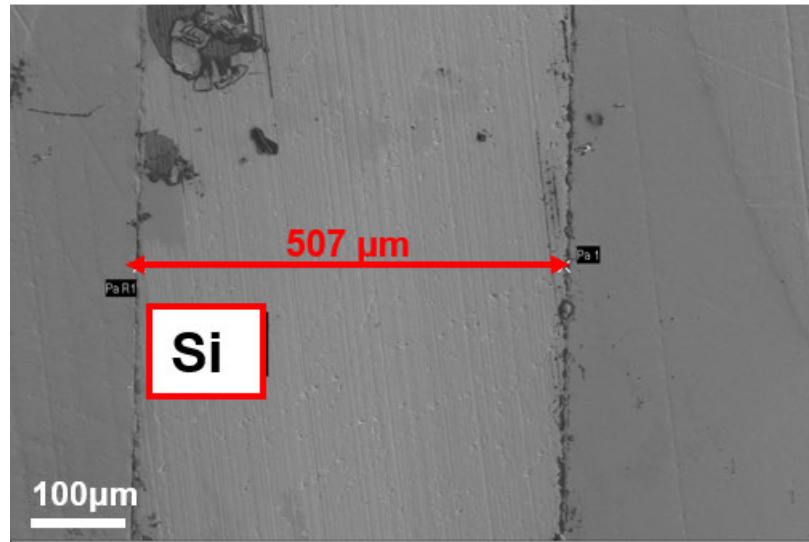


Figure 3.3. SEM Image of the As-received Silicon Wafer.

Subsequently, when the Silicon wafer was heated to 1150°C in forming gas to examine the impact of the experimental gas environment in the reactor, it was observed that the thickness of the silicon wafer had reduced by 4 micrometers, and a very thin coating of silicon oxide had formed on the surface (**Figure 3.4**).

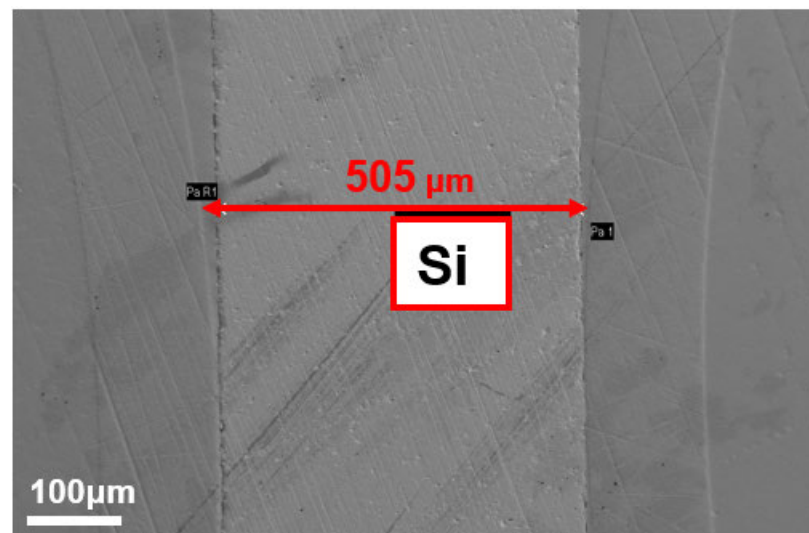


Figure 3.4. SEM Image of the Silicon Wafer above Flux in 1150 C for 6 hrs.

However, when the silicon wafer was partially immersed in the flux, the section of the wafer that was immersed in the flux showed significant thinning, with a thickness of only 155 μm (Figure 3.5).

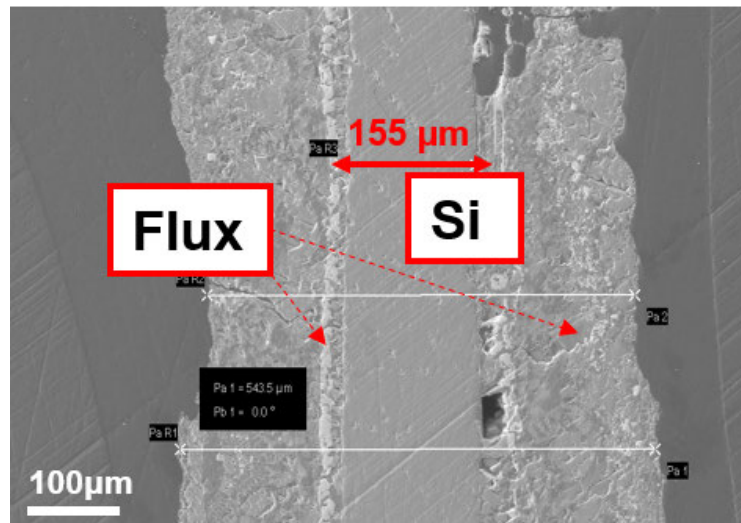


Figure 3.5 SEM Image of the Silicon Wafer Partially Immersed in the Flux.

And when the Silicon wafers were fully immersed in the flux at depths of 1.5 cm and 3 cm, the final thickness of the silicon wafers were 367 μm and 503 μm , respectively (Figure 3.6 and 3.7).

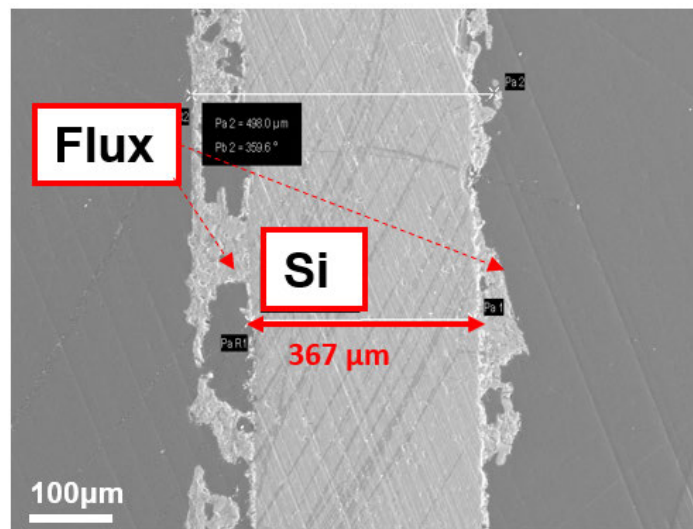


Figure 3.6 SEM image of the Silicon Wafer completely immersed at 1.5 cm deep in the flux.

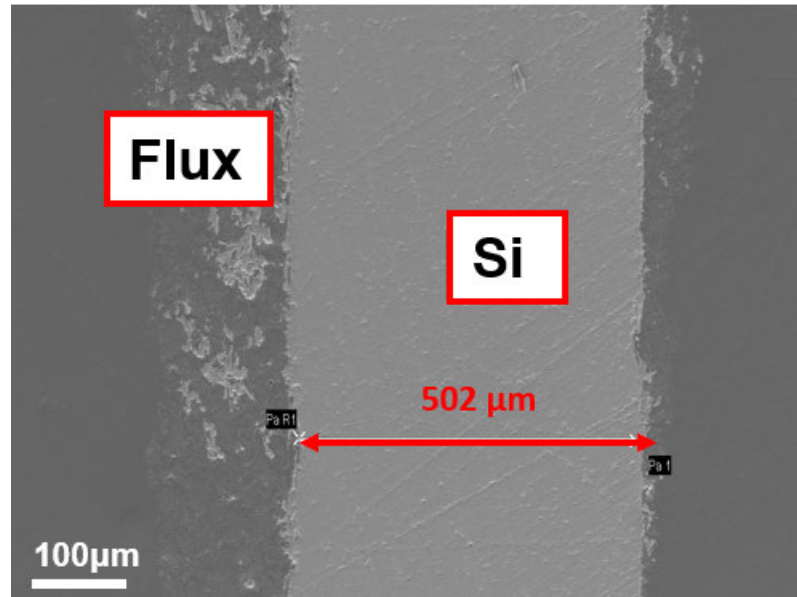


Figure 3.7 SEM image of the Silicon Wafer completely immersed at 3 cm deep in the flux.

These findings indicate that as the wafer is immersed deeper into the flux, the degree of thinning decreases. When the Silicon wafer is immersed at a depth greater than 3 cm into the flux, the thinning of Silicon wafer is mitigated.

3.3.3 Silicon Wafer Thinning Mechanism

Based on the observations of the Silicon cathode stability experiments, the mechanism of Silicon wafer thinning is proposed (**Figure 3.8**). In the presence of an electronic conductor (graphite or silicon), impurity oxygen in the gas phase is reduced to oxygen ions at the flux/gas interface. The silicon wafer is oxidized to silicon ions (Si^{4+}) at the wafer/flux interface. In this molten fluoride-oxide system, it is likely that silicon ions (Si^{4+}) exist in the form of Si -O (-F) complex ions and are dissolved in the flux. Thus, the flux aids the silicon wafer oxidation reaction, while the rate of the reaction is controlled

by electron and oxygen ion transfer between the oxidation and reduction reaction sites. As a result, increasing the immersion depth increases the resistance to electron-oxygen ion transfer and slows down the thinning of the Silicon wafer. Therefore, to prevent silicon wafer thinning during SOM electrolysis, the silicon wafer immersion depth was always kept at 4 cm from the flux/gas interface.

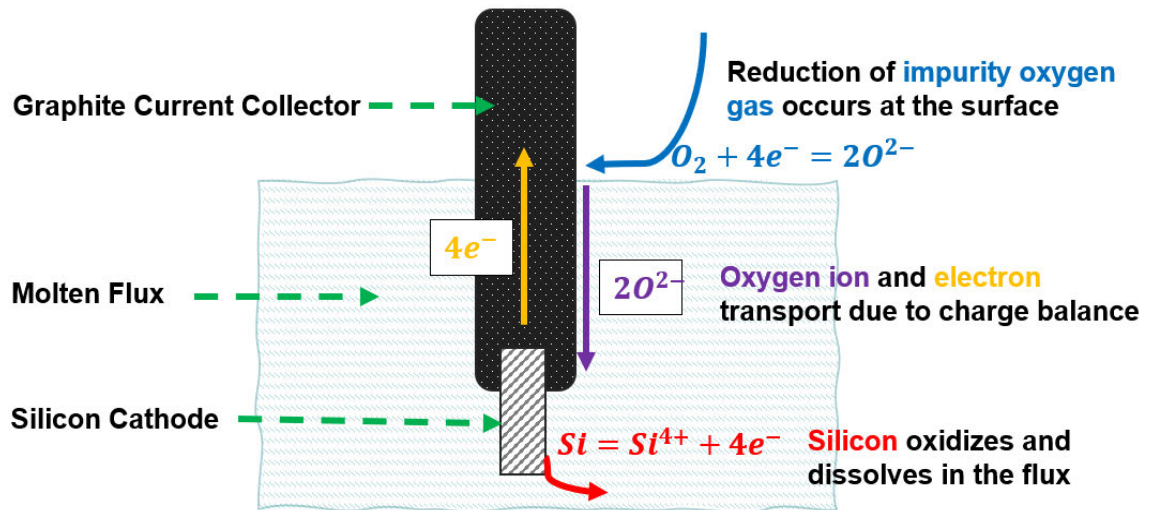


Figure 3.8 Reaction Mechanism of Si Wafer Thinning.

3.4 Elimination of Carbon and Zirconium Impurities

Another challenge encountered in the initial SOM electrolysis trials was the presence of Carbon and Zirconium in the Silicon deposits. This section will commence by presenting the detailed microstructural analysis of the post-electrolysis Silicon deposits, with a focus on its composition. Subsequently, potential origins of Carbon and Zirconium impurities and their respective formation mechanisms are proposed, followed by a series of experiments that were designed to confirm the proposed theories and eliminate the impurities from getting incorporated in the silicon deposits.

3.4.1 Initial Observations of Carbon and Zirconium Impurities in the Silicon Deposits

After the SOM electrolysis experiments, the Silicon wafer cathode with the adhering solidified flux was removed and sectioned. This sectioned piece was then mounted with epoxy and examined using SEM and EDS. The section of the Ytria-Stabilized Zirconia (YSZ) tube that contained the silver was also cross-sectioned and inspected using the same procedure. The goal of this post-characterization process was to evaluate the nature of the Silicon deposition and to verify the stability of YSZ membrane in contact with the flux.

The following set of SEM images and EDS spectra show the microscopic characteristics of the Silicon-containing deposits, the distribution of these deposits within the flux, the potential impurities contained in the Silicon deposits and the interface between YSZ membrane and the flux. Shown in **Figure 3.9**, a 17.6 μm layer of Silicon-containing deposits was observed on this interface. In addition to this layer, Silicon-containing deposits were dispersed within the flux, positioned about 400 microns from the interface between cathode and flux (**Figure 3.10**).

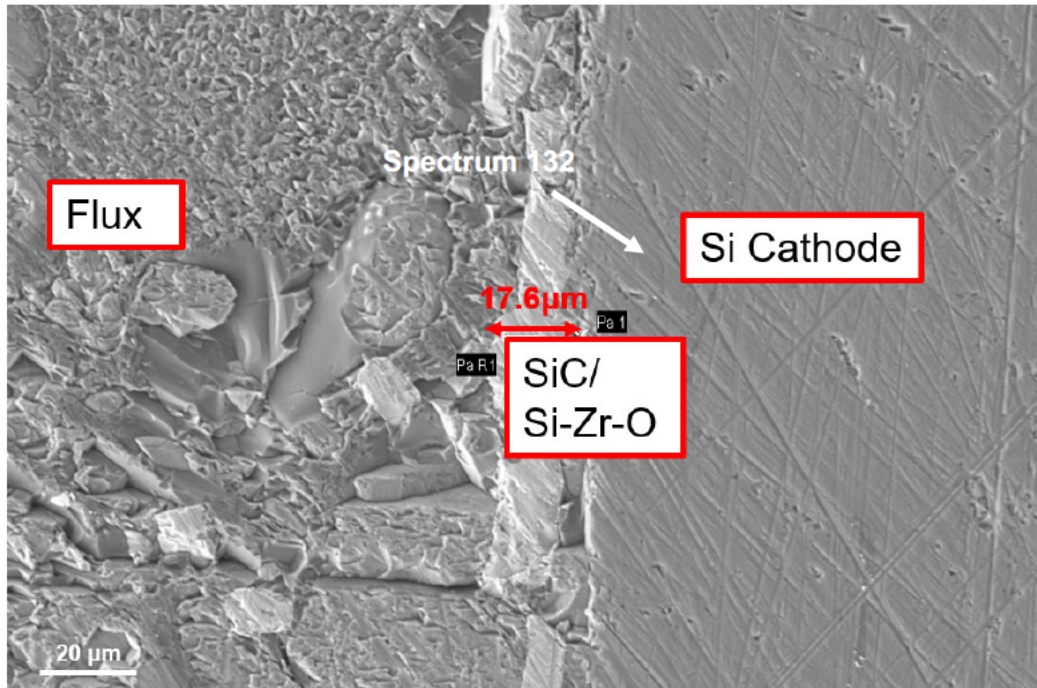


Figure 3.9. SEM image of the Si-containing deposits at the interface between cathode and flux

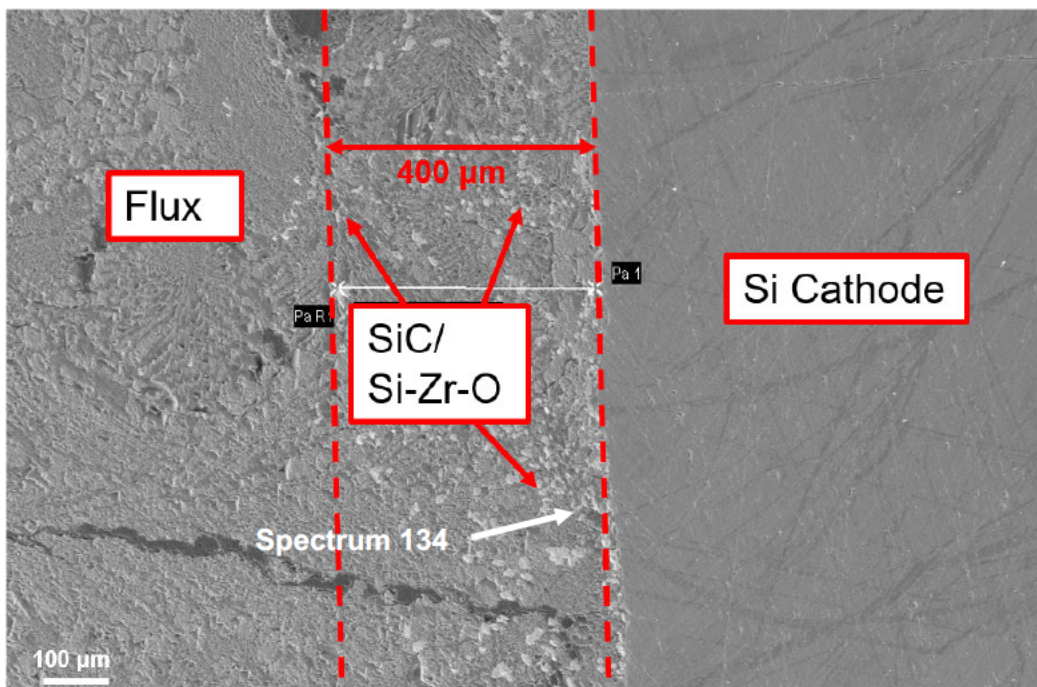


Figure 3.10 SEM image of the Si-containing deposits dispersed in the flux

EDS point analysis (**Figure 3.11** and **3.12**) suggests that Si-containing deposits predominantly comprise of Silicon Carbide (SiC) and a Silicon-Zirconium-Oxygen compound (Si-Zr-O), indicating that Carbon and Zirconium are the primary impurities within these deposits.

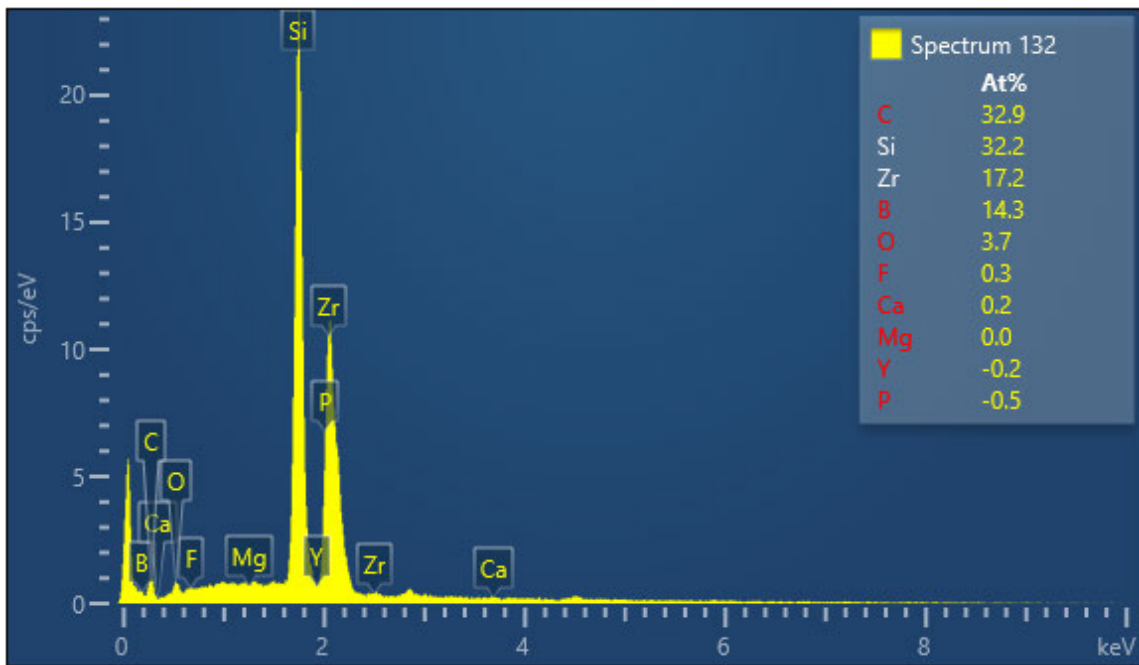


Figure 3.11. EDS Point Analysis of the Si-containing Deposits at the Cathode/Flux Interface

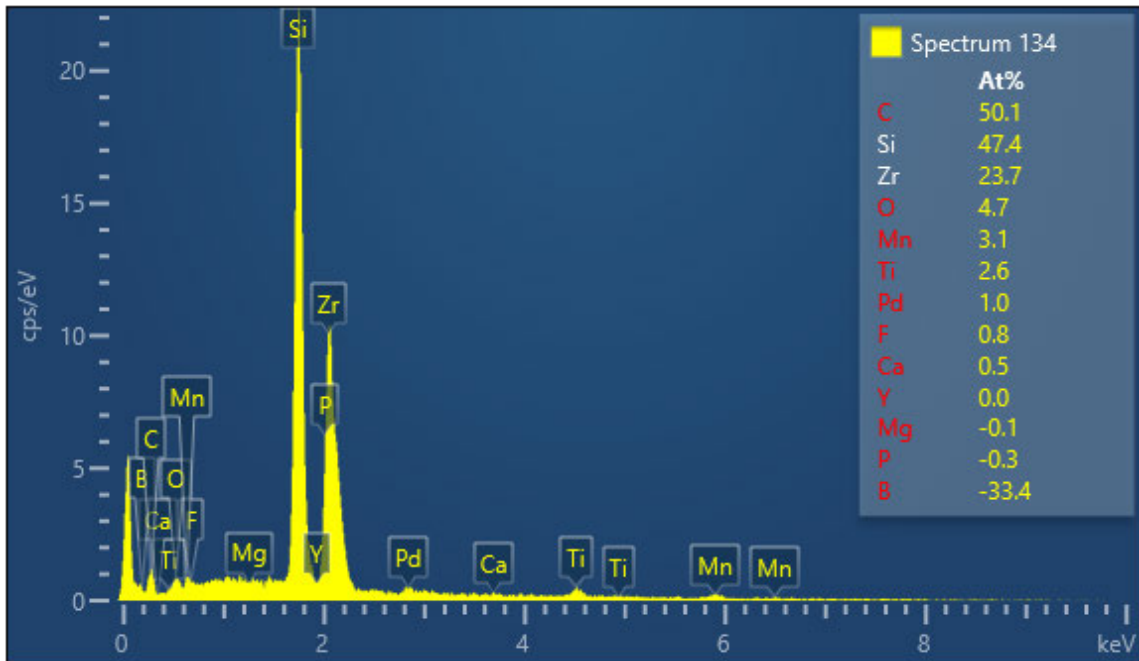


Figure 3.12. EDS Point Analysis of the Si-containing Deposits dispersed in the Flux

As depicted in **Figure 3.13**, the section of the YSZ membrane in contact with the flux did not exhibit a Yttria Depletion Layer (YDL). As discussed in Section 2, the appearance of YDL is a key sign that the YSZ membrane has been attacked by the flux [23]. The YSZ membrane appeared to be stable with the flux as no YDL was observed. However, due to the presence of Zirconium impurities, the stability of the YSZ membrane during the electrolysis was uncertain.

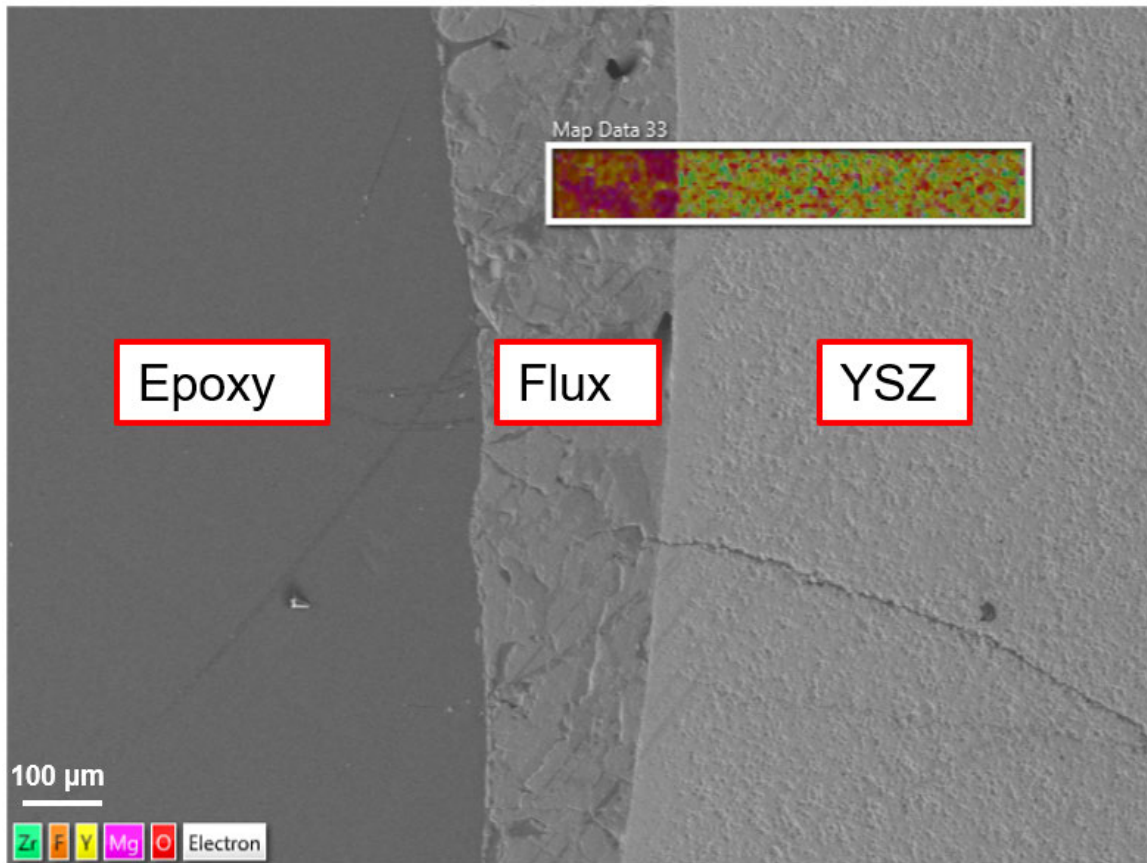


Figure 3.13. EDS Mapping of the YSZ membrane in Contact with the Flux.

3.4.2 Source and Formation Mechanism of Carbon Impurities: Postulation

A potential source of carbon impurities in the silicon deposits can be attributed to the graphite cathode current collector. During the electrolysis, the portion of the graphite cathode current collector that was in contact with the silicon cathode wafer was immersed in the flux. Small particles or fragments of carbon can detach from the graphite current collector due to the surface abrasion by the movement of the molten flux. Another source of carbon impurities in the silicon deposits might be the graphite crucible that was used to contain the molten flux during its preparation. Carbon particles detached from the graphite crucible were primarily present at the surface of the solidified flux, which was

removed prior to electrolysis. However, it is possible that trace amounts of carbon entered the flux when it was melting, and those carbon particles were not adequately removed prior to the electrolysis process.

A Si-C-O phase stability diagram was used to understand the thermodynamic behavior and potential reactions of carbon in the SOM environment. By examining the stability regions and boundaries on this diagram, conditions under which certain phases are thermodynamically favored or not can be determined. As a result, potential reaction pathways are identified, and the formation of impurities or undesired compounds can be predicted.

The Si-O-C phase stability diagram is shown in **Figure 3.14**. The diagram suggests that in the presence of carbon at unit activity ($a_c = 1$), as the oxygen partial pressure (P_{O_2}) decreases to below 10^{-23} , Silica is converted into Silicon Carbide (SiC). Silicon is thermodynamically stable when P_{O_2} is below $2.5 * 10^{-26}$ and a_c is below $4 * 10^{-3}$ at the cathode. During electrolysis, P_{O_2} at the cathode is significantly low due to the applied potential, however, due to the presence of carbon particles that originated from either the cathode current collector or the crucible, a_c would be near 1. Based on this understanding, to eliminate the formation of SiC, no carbon should be present at the cathode during the electrolysis.

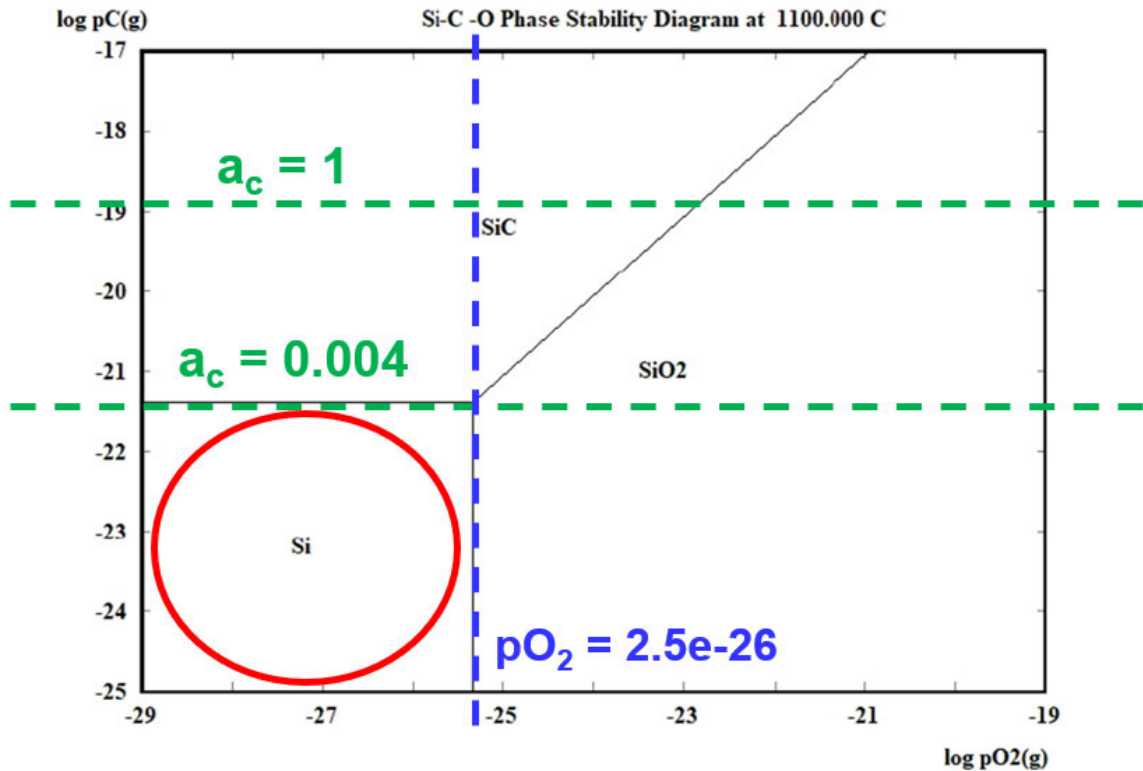


Figure 3.14. Si-C-O Phase Stability Diagram at 1100 C.

3.4.3 Source and Formation Mechanism of Carbon Impurities: Validation

To evaluate the exact source of carbon impurities in the silicon deposits and confirm the mechanism, a validation experiment was designed and conducted. The experiment involved replacing the graphite cathode current collector with a tungsten current collector while retaining the graphite crucible. The silicon wafer cathode was securely connected to a tungsten rod by creating a slit at the bottom of the rod, inserting the silicon wafer into the slit, and applying a tungsten paste (purchased from Nanochemazone) to secure the joint. Following that, the combined Silicon-Tungsten cathode assembly was immersed 4 cm deep into the flux with the same YSZ membrane-based anode assembly at 1150 C. The SOM electrolysis at 0.95V was then performed for

8 hours. After the flux cooled, the Silicon wafer with the solidified flux was sectioned, mounted with epoxy and evaluated under SEM/EDS.

Figure 3.15 and **3.16** presents the SEM image of the sectioned Silicon wafer cathode and accompanying EDS spot analysis. Notably, SiC was not detected at the interface between silicon wafer and the flux. Zirconium was still present as one of the major impurities in the Silicon deposits, which existed in the form of Si-Zr-O. Based on this observation, it is evident that the replacement of the graphite current collector eliminates the presence of SiC. Therefore, it can be concluded that the carbon impurities originated solely from the graphite cathode current collector. In addition, it is confirmed that the presence of carbon in proximity of cathode leads to the formation of SiC. This validates the proposed theories regarding the source of carbon impurities and their formation mechanism.

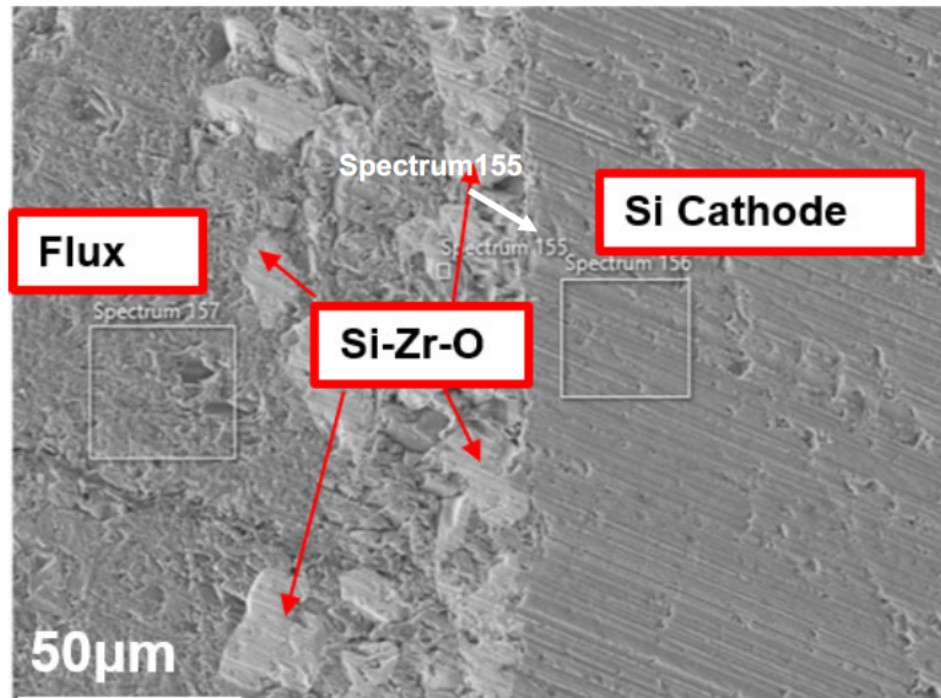


Figure 3.15. SEM Image of the Si-Zr-O at the Cathode/Flux Interface.

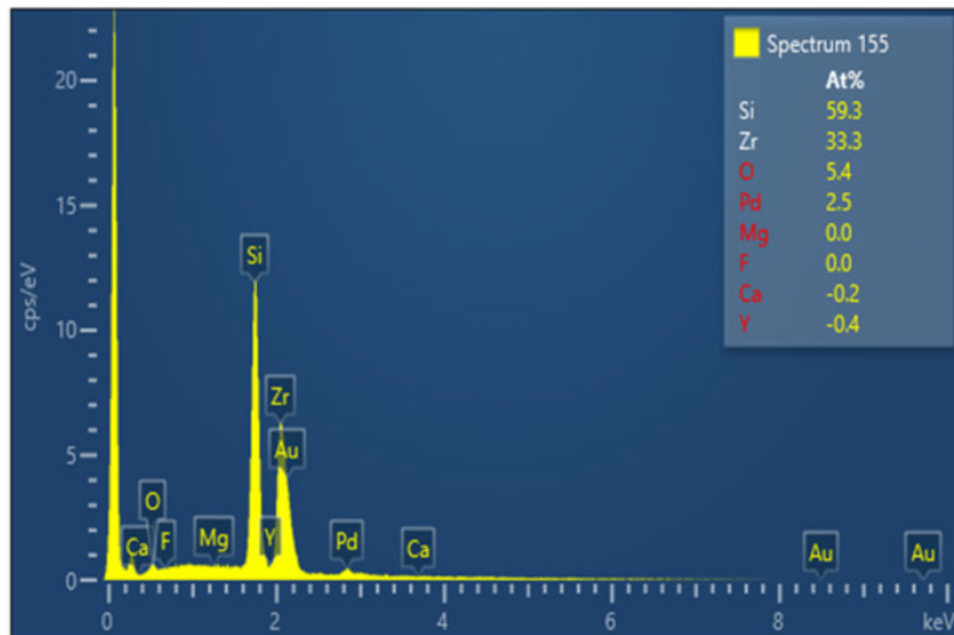


Figure 3.16. EDS Point Analysis of the Si-containing Deposits with Zr as the Major Impurity.

3.4.4 Source and Formation Mechanism of Zirconium Impurities: Postulation

Despite successfully eliminating the formation of Silicon Carbide (SiC) by replacing the graphite current collector, the presence of Zirconium (Zr) impurities persisted in the Silicon deposits. One possible source of Zr impurities could be attributed to the presence of impurities within the flux. During the preparation of the flux, Zirconia balls were utilized to ball-mill the mixture of fluoride and oxide powders. Moreover, it should be noted that the SiO₂ powder and graphite crucible employed in the SOM experiment were reported to contain traces of ZrO₂, with concentrations of up to 3 ppm.

Another possible source of Zr impurities could be the Yttria-Stabilized Zirconia (YSZ) membrane. If Zr is observed to leave the YSZ membrane, there are two proposed mechanisms to consider. The first mechanism is the yttria depletion in the YSZ membrane caused by the imbalance of optical basicity between the flux and the YSZ membrane. As previously discussed, no yttria depletion was observed at the sectioned interface between YSZ and the flux. However, it is possible that yttria depletion exists in other sections of YSZ tube and those regions were not analyzed under SEM and EDS. The second mechanism involves an unknown process that causes the destabilization of Zr from the YSZ membrane. This requires further investigation to determine the exact mechanism involved.

Furthermore, once Zr is present in the flux, mechanisms through which Zr impurities are incorporated into the Silicon deposits are unclear. Based on the reactivity and availability of Si (from the cathode) and SiO₂ (from the flux), the complex interplay between Zr, Si, and SiO₂ in the formation of Zr impurities in the Silicon deposits should

be considered. Hence, several chemical reaction pathways (referred as Postulation 1, 2 and 3 in the following section) that involve the sources and formation mechanisms of Zr impurities are proposed:

- 1: Si originated from the cathode reacts with Zr impurities in the flux.
2. Si originated from the cathode reacts with Zr detached from the YSZ membrane.
3. SiO₂ in the flux reacts with Zr detached from the YSZ membrane.

3.4.5 Source of Zirconium Impurities: Validation

A series of validation experiments corresponding to different proposed reaction pathways were designed and conducted. To test Theory 1, a Si wafer was immersed in a new batch of SOM flux for 6 hours without the presence of the YSZ tube (Flux Run #1). To validate the reaction mechanisms suggested by Theory 2 and 3, it is crucial to attribute the source of Zr solely to the YSZ membrane. This necessitates the use of a Zr-free SOM flux, which was achieved by employing silica ball media during the ball-milling process. Additionally, a thorough SEM/EDS analysis was conducted on the SOM flux prior to the testing experiments to ensure that there were negligible Zr impurities in the flux.

The validation experiments corresponding to Theory 2 and 3 were then conducted. To test Theory 2, both the Si wafer and YSZ tube were placed in the SOM flux that contained no SiO₂ at 1150 C for 8 hrs (Flux Run #2). To test Theory 3, both the Si wafer and YSZ tube were placed in the SOM flux that contained 5wt% of SiO₂ at 1150 C for 8 hrs (Flux Run #3). If Si-Zr-O is only detected at the interface between the silicon wafer and flux in Flux Run#3, it suggests that the formation of Si-Zr-O is more likely

attributed to SiO_2 rather than Si originating from the cathode.

Next, to assess whether Yttria depletion was responsible for Zr detachment from the membrane, experiments were conducted by immersing both the Si wafer and YSZ tube in the SOM flux containing 5% and 10% excess optical basicity compared to that of Yttria (Flux Run #4 and #5). This was achieved by maintaining a fixed amount of CaO (9wt%) and reducing the amount of SiO_2 to 4.74 wt% and 3.57 wt% respectively.

All validation experiments were performed in the same SOM experiment condition (1150 °C, reducing environment) without any applied potential. This approach provides valuable insight into the nature of the formation of Si-Zr-O, specifically whether it is primarily a result of a chemical reaction or an electrochemical reaction. After each experiment was complete, the Silicon wafers with flux and YSZ membranes with flux were sectioned and mounted in epoxy. These prepared samples were then examined using SEM/EDS analysis. A pristine YSZ membrane was also prepared using a similar method and evaluated under SEM/EDS as a reference. By preparing and analyzing the pristine YSZ membrane in the same manner as the experimental samples, any observed differences or deviations in the experimental samples could be attributed to the specific conditions and interactions involved in the validation experiments.

Table 3.2 provides a summary of the experimental results, along with the corresponding theories being tested and the experimental setups employed. A comparison between the results of Flux Run #1 and the remaining experiments confirmed that the YSZ tube is the source of Si-Zr-O. When SiO_2 was not added to the flux, no Si-Zr-O was observed, indicating that the presence of SiO_2 in the flux is necessary for its formation.

Additionally, variation of SiO₂ content in the flux did not result in any noticeable changes in the thickness and composition of Si-Zr-O. In the experiments where the flux had an excessive optical basicity compared to Ytria, no Ytria depletion was observed at the interface between the YSZ membrane and the flux. These findings suggest that Ytria depletion did not occur during the actual SOM electrolysis, and the optical basicity of the flux is not the cause of Zr detachment from the YSZ membrane. The mechanisms of Zirconium detachment from YSZ membrane requires further analysis.

Experiment	Description	Aim	Results
Flux Run#1	Si cathode dipped into new batch of SOM flux	To test Postulation 1	Zr impurities was not observed at the interface between Si and flux.
Flux Run#2	Si cathode and YSZ membrane dipped into a batch of Zr-free SOM flux with no SiO ₂	To test Postulation 2	Zr impurities was not observed at the interface between Si and flux;
Flux Run#3	Si cathode and YSZ membrane dipped into a batch of Zr-free SOM flux with 5 wt% SiO ₂ ($\Lambda_{\text{flux}} = \Lambda_{\text{Ytria}}$)	To test Postulation 3	15 – 20 μm of Si-Zr-O observed at the interface between Si and flux; YDL was not observed.
Flux Run#4	Si cathode and YSZ membrane dipped into a batch of Zr-free SOM flux with 4.74% wt SiO ₂ ($\Lambda_{\text{flux}} = 1.05 * \Lambda_{\text{Ytria}}$)	To assess whether Ytria depletion was responsible for Zr detachment from the membrane	15 – 20 μm of Si-Zr-O observed at the interface between Si and flux; YDL was not observed.
Flux Run#5	Si cathode and YSZ membrane dipped into a batch of Zr-free SOM flux with 3.57 wt% SiO ₂ ($\Lambda_{\text{flux}} = 1.10 * \Lambda_{\text{Ytria}}$)	To assess whether Ytria depletion was responsible for Zr detachment from the membrane	15 – 20 μm of Si-Zr-O observed at the interface between Si and flux; YDL was not observed.

Table 3.2. Description, Aim and Observation of Experiments to Validate the Source and Formation Mechanism of Zirconium Impurities.

3.4.6 Mechanisms of Zirconium Detachment from YSZ membrane

Microstructural analysis on the interface between YSZ membrane and flux provides deeper insight into the possible mechanism of Zirconium (Zr) destabilization from YSZ membrane. **Figure 3.17** shows the YSZ boundary of a pristine YSZ tube after it was sectioned and mounted in epoxy. No mechanical failure or composition change was detected, suggesting that the preparation process of the YSZ membrane was not the cause of Zr detachment.

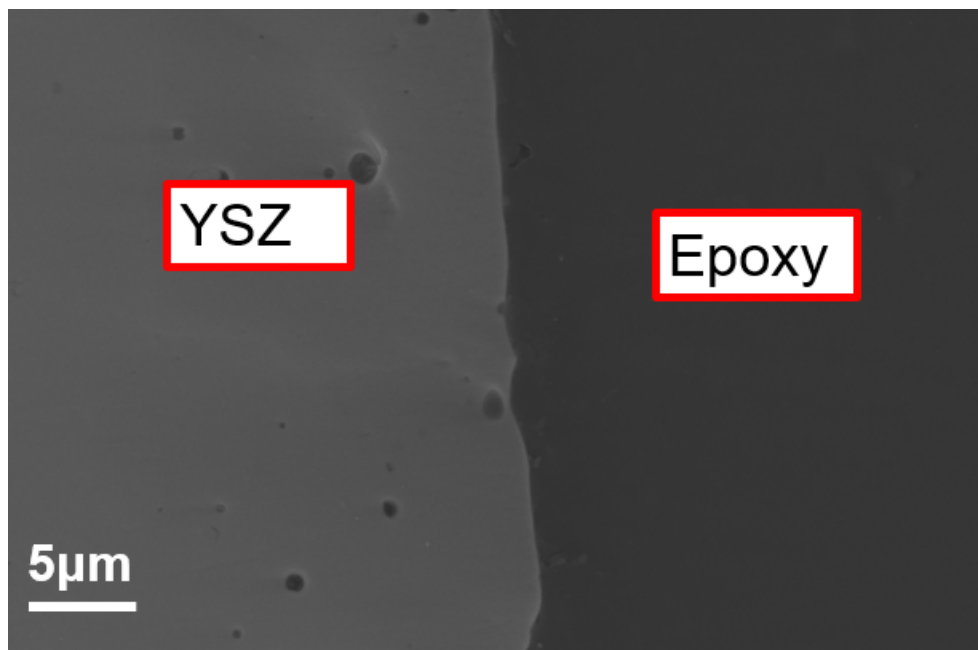


Figure 3.17. SEM Image of the Pristine YSZ Membrane.

Yttria depletion layer (YDL) was not observed on the YSZ membrane in all validation experiments (Flux Run#1 to #5). However, multiple particles were observed to detach from the YSZ membrane after Flux Run #2 was complete (**Figure 19**).

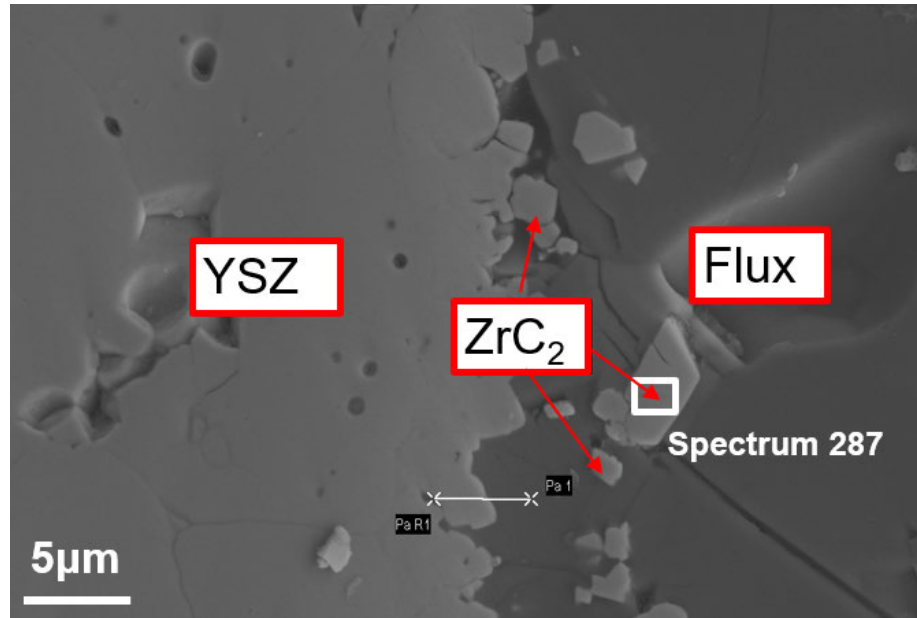


Figure 3.18. SEM Image of YSZ/Flux Interface after Flux Run #2.

The subsequent EDS analysis confirms that the detached particles were primarily composed of a hyper stoichiometric Zirconium Carbide (carbon rich; $C/Zr = 2$) (**Figure 3.19**). The possible source of carbon for the formation of Zirconium Carbide is attributed to the graphite crucible used to contain the molten flux.

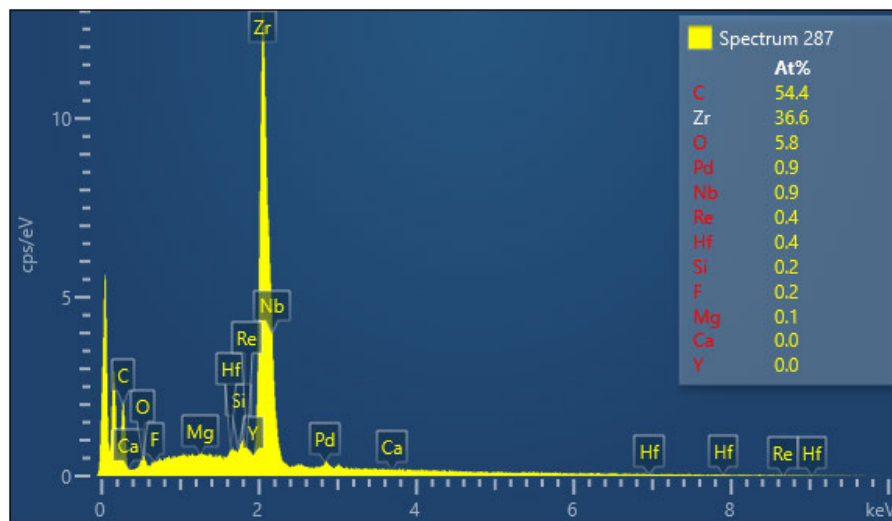


Figure 3.19. EDS spot analysis of ZrC_x at the YSZ/Flux Interface after Flux Run #2.

In the experiments where the SiO₂ content was varied (Flux Run #4 and Run #5), a distinct degradation layer with a thickness of approximately 5 μm was observed at the interface between the YSZ membrane and the flux. (**Figure 3.20** and **3.21**).

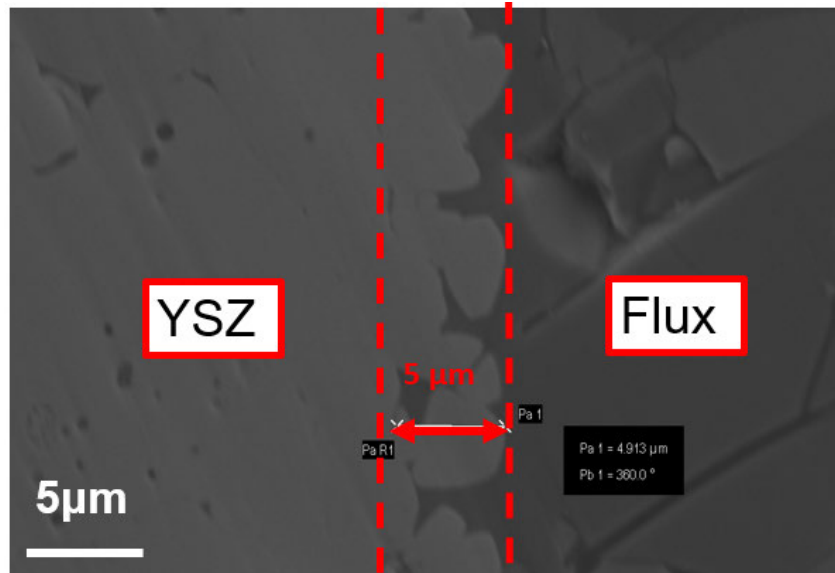


Figure 3.20. SEM Image of YSZ/Flux Interface after Flux Run #4

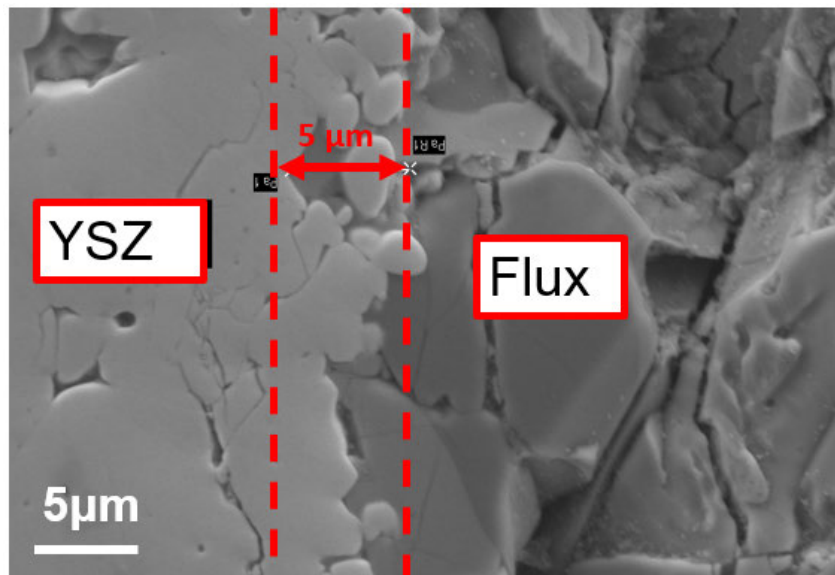


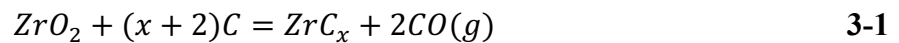
Figure 3.21. SEM Image of YSZ/Flux Interface after Flux Run #5

Subsequent EDS analysis conducted on these degraded regions revealed a notable decrease in the Zr concentration compared to the bulk of the YSZ membrane (**Table 3.3**). This observation suggests that Zr at the boundary of the YSZ crystals leaves the YSZ membrane and migrates into the flux.

Region	Atomic Concentration (%)			Atomic Ratio
	Y	Zr	O	Zr/Y
Bulk of the YSZ membrane	3.5	27.8	68.6	7.94
Degradation layer in Flux Run #4	18.2	28.7	46.9	1.58
Degradation layer in Flux Run #5	19.4	30.2	38.4	1.56

Table 3.3. Composition of YSZ in Bulk of the YSZ Membrane and Degradation Layer in Flux #4 and Flux #5.

Based on these observations, a possible series of reactions that involved ZrO_2 , and C and SiO_2 were considered. First, the reaction related to Zr leaving the YSZ membrane surface was proposed. ZrO_2 may react with carbon that were dispersed in the flux to form Zirconium Carbide (ZrC_x), shown in **Equation 3-1**.



As Zr has an oxidation state of -2, 0, +1, +2, +3, +4 and C has an oxidation state of 0, ± 1 , ± 2 , ± 3 , and ± 4 , the coefficient of C in ZrC_x can range from 0.25 to 4. Based on the EDS analysis of the ZrC_x at the interface between YSZ and flux, it is likely ZrC_2 ($x=2$). However, thermodynamic data available in the HSC database only include two types of ZrC_x , ZrC and ZrC_4 . The formation of ZrC ($x=1$) has a Gibbs free energy of 191.56 kJ/mol at 1100°C, suggesting it is thermodynamically unfavorable. On the other hand, the formation of ZrC_4 ($x=4$) has a Gibbs free energy of -797.97 kJ/mol at 1100°C,

indicating it is thermodynamically favored. Therefore, it is possible that the observed ZrC_x ($x=2$) was formed based on the mechanism described in Equation 3-1 as:

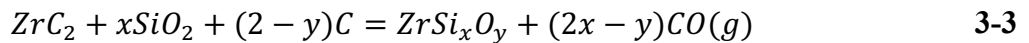


Subsequently, it is likely that the ZrC_2 compound reacts with SiO_2 to form the Si-Zr-O compound. In order to determine the precise stoichiometry of the Si-Zr-O compound and investigate its formation mechanism, EDS spot analysis was conducted on several Si-Zr-O compounds. The atomic concentrations of Si, Zr, and O in the Si-Zr-O compounds are presented in **Table 3.4**.

Region	Atomic Concentration (%)			Atomic Ratio	
	Si	Zr	O	Si/Zr	O/Zr
1	59.5	35.8	4.7	1.66	0.13
2	49.0	26.7	24.3	1.83	0.91
3	60.5	34.0	5.5	1.78	0.16
4	55.4	33.1	11.5	1.68	0.35
5	47.6	28.1	24.3	1.69	0.87

Table 3.4 Composition of Si-Zr-O Observed in Different Regions at the Cathode/Flux Interface.

Based on the EDS analysis, this Si-Zr-O compound was determined to be $ZrSi_xO_y$ (x ranges from 1.66 to 1.83; y ranges from 0.13 to 0.91) As a result, the reaction between ZrC_2 and SiO_2 was proposed as:



Due to the lack of existing thermodynamic data on Si-Zr-O compounds in the available literature databases, this reaction cannot be verified. However, considering the

experimental observations from Flux Run #2 and the proposed formation mechanism of the Si-Zr-O compound, it is proposed that the elimination of carbon from the SOM environment should lead to the elimination of the Si-Zr-O compounds.

3.4.5 Formation Mechanism of Zirconium Impurities: Validation

To validate the postulation that the elimination of carbon can result in the elimination of Zirconium impurities in the Silicon deposits, a SOM electrolysis experiment was conducted in a carbon-free environment. A silicon wafer attached with a Tungsten current collector was immersed 4 cm deep into the flux. The YSZ-encased anode assembly was immersed at the same depth into the flux. The flux was contained in a stainless-steel crucible, and its composition remained as eutectic $\text{CaF}_2 - \text{MgF}_2$ with 9 wt% CaO, 5 wt% SiO_2 and 4 wt% YF_3 . The electrolysis was performed in a reducing environment at 1150 C for 8 hrs. Following the electrolysis, the silicon wafer cathode was sectioned, mounted in epoxy, and examined using SEM and EDS analysis.

Figure 3.22 presents the interface between the silicon wafer and the flux following the electrolysis process. The corresponding EDS mapping in **Figure 3.23** reveals that Zr impurities in the silicon deposits was not detected either in the interface between the cathode and flux or in the bulk of the flux. This confirms the theory that once the electrolysis excludes any source of carbon, Zr impurities can be eliminated. However, other phases were observed which will be discussed next.

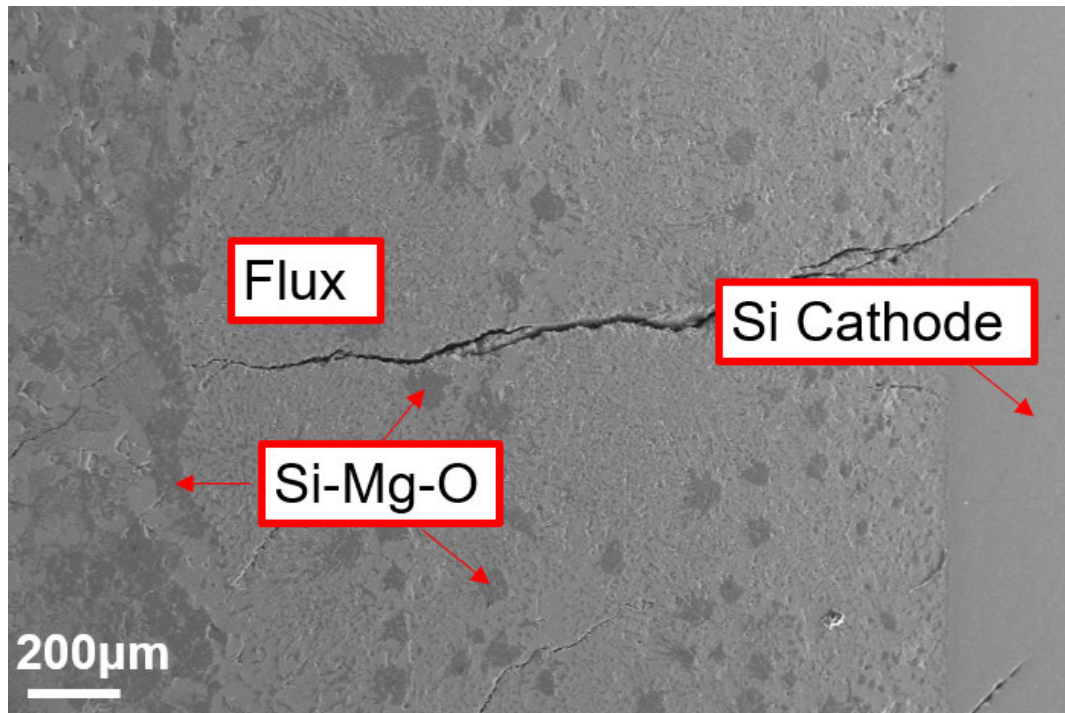


Figure 3.22. SEM Image of the the Cathode/Flux Interface after the Carbon-free electrolysis (50X Magnification)

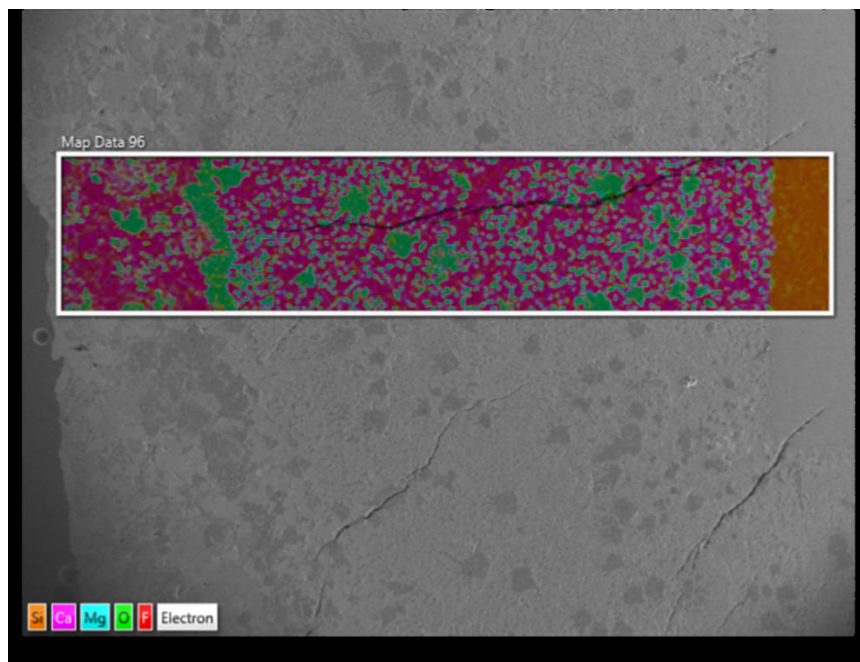


Figure 3.23. EDS mapping of the Cathode/Flux Interface after the Carbon-free Electrolysis.

Thus, by employing a Tungsten current collector and Stainless-steel crucible, the issues of C and Zr impurities in the silicon deposits was solved. Nonetheless, by closely examining the interfaces between Si cathode and flux, two new phases were observed, shown in **Figure 3.24**.

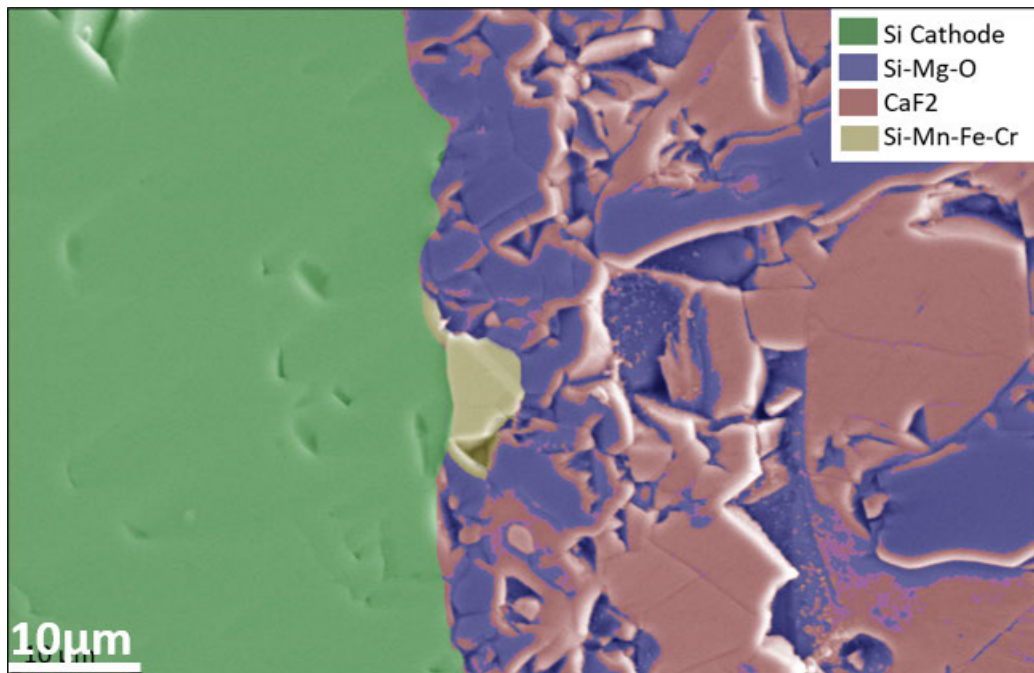


Figure 3.24. SEM image of the Cathode/Flux Interface after the Carbon-free electrolysis (1 kX magnification)

Further EDS analysis suggests that one phase corresponded to an intermetallic compound of Si, Mn, Cr, and Fe (**Figure 3.25**), while the other phase was identified as Si-Mg-O (**Figure 3.26**).

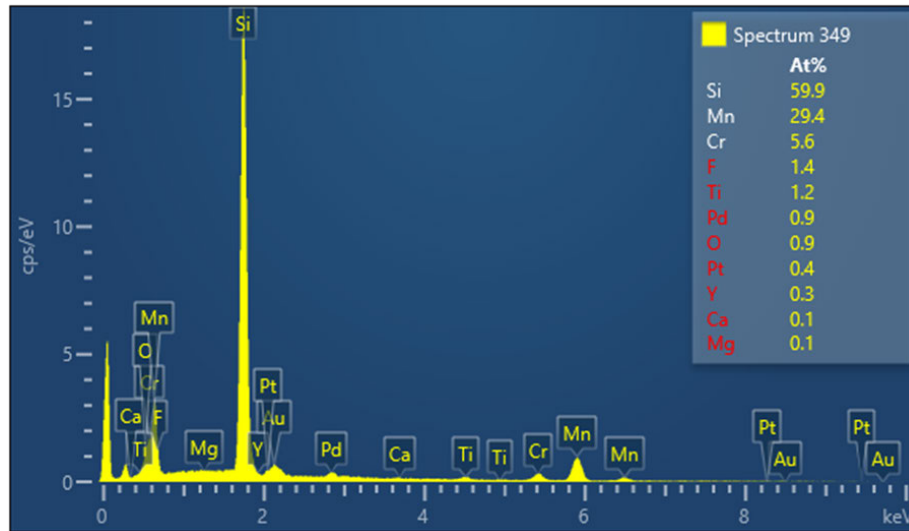


Figure 3.25 EDS Spot Analysis of the Si-Mn-Cr Deposits.

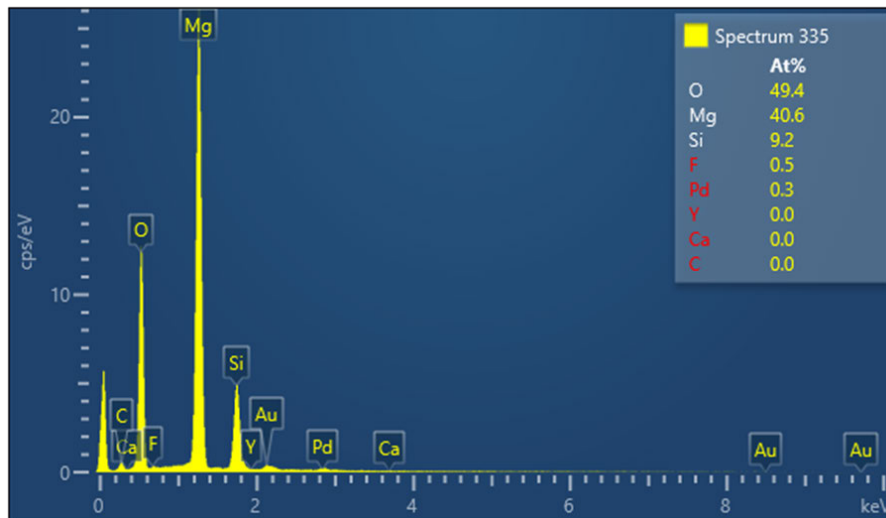


Figure 3.26 EDS Spot Analysis of the Si-Mg-O Phase.

Given that the intermetallic compound has been previously observed in SOM experiments for other metal productions, its formation mechanisms are well-understood, and will be described in the next section along with the source and formation mechanism of the Si-Mg-O phase.

3.5 Elimination of Silicon-Magnesium-Oxygen Phase

As the SOM electrolysis needs to be performed in a carbon-free environment, a Tungsten current collector and a stainless-steel crucible was employed. While this change effectively eliminated Carbon and Zirconium impurities in the Si deposits, it introduced two new phases.

First, the Si deposits exhibited the presence of Mn, Fe, and Cr compounds. Sources of those impurities could be attributed to the Stainless-steel crucible. Stainless steel, when subjected to trace amounts of oxygen in the SOM environment, forms metal oxides of Cr, Mn, and Fe. According to the Table of Dissociation Potential of major oxides in the SOM system, it is evident that these metal oxides, such as Cr, Mn, and Fe, display higher reactivity (lower dissociation potential) compared to silica within the flux. Furthermore, suggested by previous research, these metal oxides have demonstrated moderate solubility in the SOM flux. As a result, during the electrolysis process, the reduction of these metal oxides takes precedence over the dissociation of silica. Fortunately, the presence of Cr, Mn, and Fe in the silicon deposits was not a major concern, as potential steel sources could be easily eliminated from the system. By employing a Boron Nitride crucible to contain the molten flux and excluding any stainless-steel bubbling tube in the setup, a stainless-steel free SOM environment can be obtained.

However, the source and formation mechanism of the Si-Mg-O phase remained unclear, prompting a need for a thorough investigation to unveil its underlying causes.

3.5.1 Source and Formation Mechanism of Si-Mg-O Phase: Postulation

One possible source of magnesium (Mg) is attributed to the presence of MgF₂ in the flux. It is postulated that the oxygen content in the flux from SiO₂ (5 wt%) and CaO (9 wt%), creates an MgO phase in the SOM flux which contributes to the formation of the Si-Mg-O phase. This suggests that by reducing the content of CaO and SiO₂ in the flux one can reduce the MgO activity or eliminate the MgO phase and thereby lower the likelihood of the formation of the Sr-MgO phase.

Furthermore, it is also crucial to investigate the reaction pathways through which MgO transforms into the Si-Mg-O phase. In the presence of MgO within the flux, a series of electrochemical and chemical reactions can occur, resulting in the formation of the Si-Mg-O phase. When a potential that exceeds the standard dissociation potential of MgO (1.12 V) is applied during the electrolysis, MgO is reduced to Mg and O₂ (**Equation 3-4**).



The reduced Mg then can react with SiO₂, resulting in the formation of Si-Mg-O phase (**Equation 3-2** and **3-3**).



The Gibbs free energy of **Equation 3-5** at 1150 C is -231.60 kJ/mol, suggesting that this reaction is thermodynamically favored. The exact speciation between MgO and Si in the SOM flux system remains unclear. Nevertheless, based on the EDS spot analysis on the Si-Mg-O phase shown in **Figure 3.26**, the atomic ratio of Mg to O is close to 1:1, implying the incorporation of MgO into Si as a whole.

3.5.2 Source and Formation Mechanism of Si-Mg-O Phase: Thermodynamic Analysis

Phase diagrams generated on FactSage with varying amounts of CaO and SiO₂ can provide further support for this postulation. **Figure 3.27** presents the phase diagram of CaF₂ – MgF₂ – CaO – SiO₂ with eutectic CaF₂ - MgF₂ and 10 mol% CaO (9 wt%). The x-axis represents the molar ratio of Silica, while the y-axis corresponds to the temperature. When the concentration of Silica is held constant at 5.8 mol% (5wt %), the composition of this flux is essentially the same as that of the SOM flux used, except for the variation due to the amount of YF₃. It is believed that the presence of YF₃ does not significantly influence the formation of MgO in the system. Therefore, YF₃ was not included in this phase diagram.

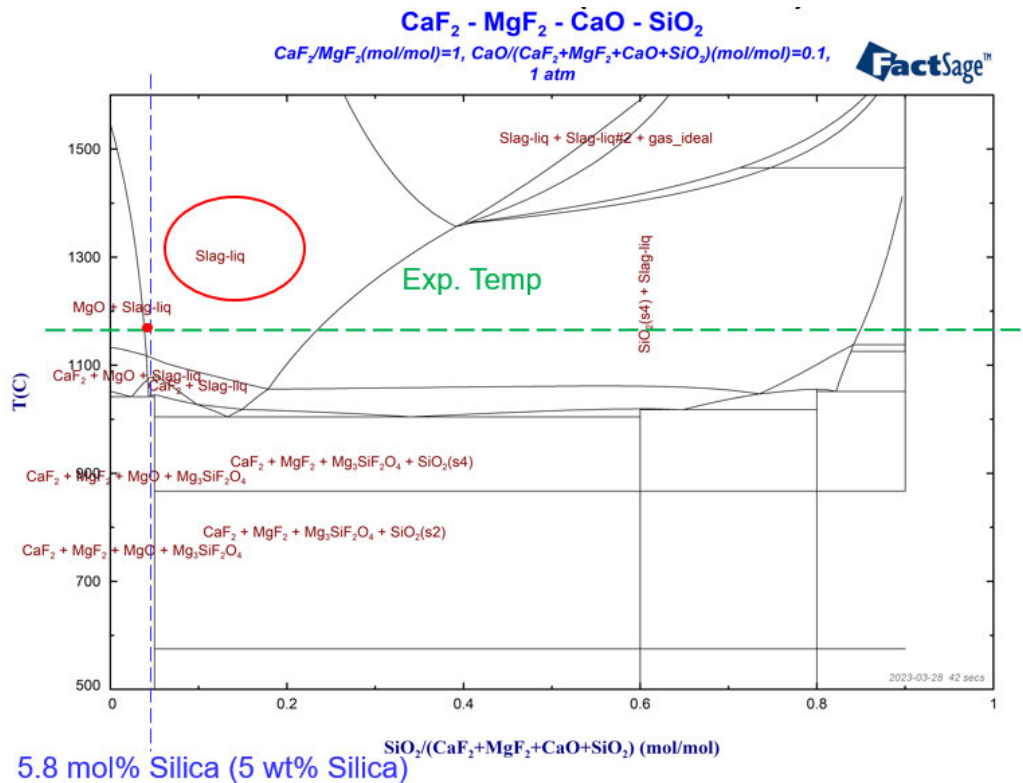


Figure 3.27. Phase Diagram of CaF₂-MgF₂-CaO-SiO₂ with Eutectic CaF₂ - MgF₂ and 10 mol% CaO (9 wt%).

From this phase diagram, at an SiO_2 concentration of 5.8 mol% (5 wt%), it is highly likely that the molten flux at the operating temperature (1150 C) consists of two distinct phases. One phase corresponds to the presence of MgO, while the other phase represents the salt (slag) liquid region (red-circled). The latter phase represents the molten species in this system, which consists of a eutectic mixture of CaF_2 and MgF_2 , along with the Si-O-F complex. In order to ensure an efficient SOM electrolysis process, it is desirable for the entire flux to exist within the “Slag-liq” phase.

To evaluate the potential elimination of the MgO phase by reducing the content of CaO and SiO_2 , a phase diagram of $\text{CaF}_2 - \text{MgF}_2 - \text{CaO} - \text{SiO}_2$ with eutectic $\text{CaF}_2 - \text{MgF}_2$ and 5 mol% CaO (4 wt%) as a function of SiO_2 was created (**Figure 29**). The x-axis represents the molar ratio of Silica, while the y-axis corresponds to the temperature. As the content of CaO was changed, the maximum allowed SiO_2 content had to be adjusted to maintain the same optical basicity in the flux as that of Yttria in the YSZ membrane. Based on **Equation 2-10**, the maximum allows SiO_2 content was 2.8 mol% (2.5 wt%).

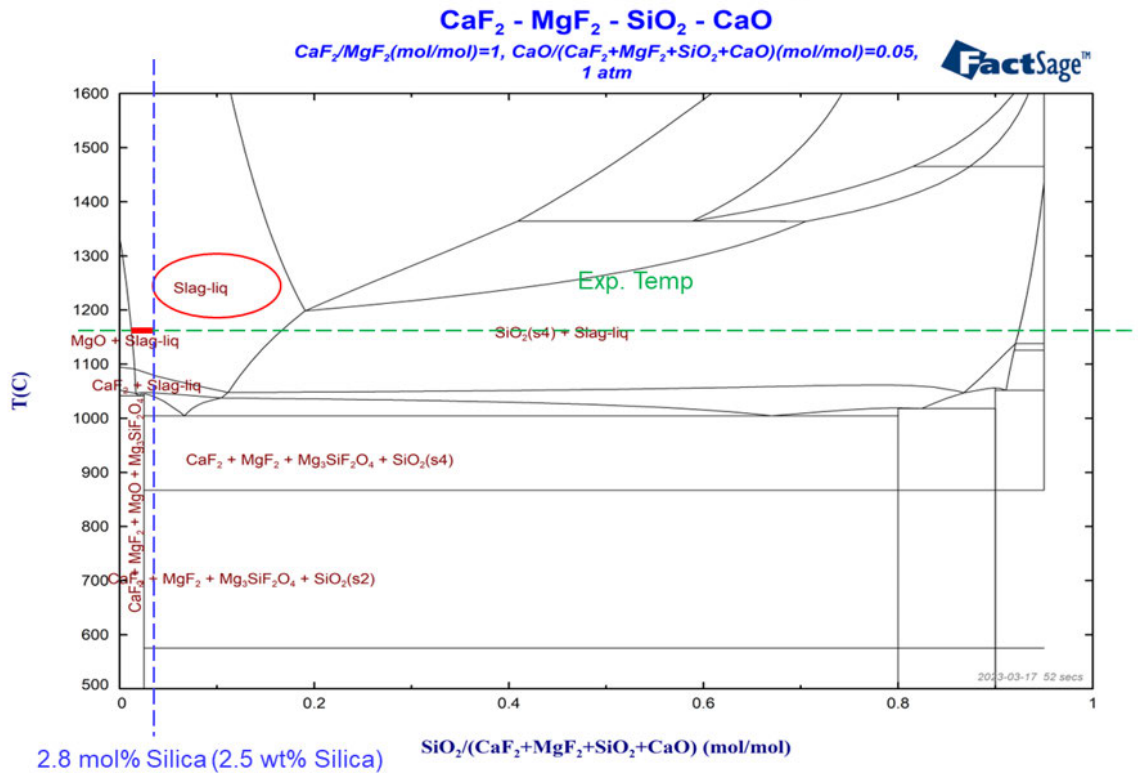


Figure 3.28 Phase Diagram of CaF₂-MgF₂-CaO-SiO₂, with eutectic CaF₂ - MgF₂ and 5 mol% CaO (4 wt%).

At a SiO₂ concentration of 2.5 wt%, the flux remains exclusively within the 'Slag-liq' region, and no MgO is present at this composition. Therefore, thermodynamic simulation results support the postulation that by reducing the content of CaO and SiO₂, the formation of MgO can be eliminated.

3.5.3 Source and Formation Mechanism of Si-Mg-O Phase: Validation

A validation experiment was conducted to confirm the source and formation mechanism of Si-Mg-O phase. A silicon wafer attached with a Tungsten current collector was immersed 4 cm deep into the flux. To eliminate the source of stainless steel, a boron nitride crucible was used to contain the flux, and no steel bubbling tube was employed

during the electrolysis. The flux composition consisted of a eutectic $\text{CaF}_2\text{-MgF}_2$ with 2.5 wt% SiO_2 and 4 wt% CaO . The electrolysis process was carried out in a reducing environment at 1.8 V for 8 hours. Following the electrolysis, the silicon wafer cathode was sectioned, mounted in epoxy, and subjected to evaluation using SEM and EDS analysis.

Figure 3.29 presents the interface between the silicon wafer and the flux following the electrolysis process. The corresponding EDS mapping in **Figure 3.30** confirms that Mn, Fe, and Cr impurities in the silicon deposits are eliminated once the use of stainless-steel crucibles was eliminated. The Si-Mg-O phase was also not observed, as Si and Mg were clearly separated.

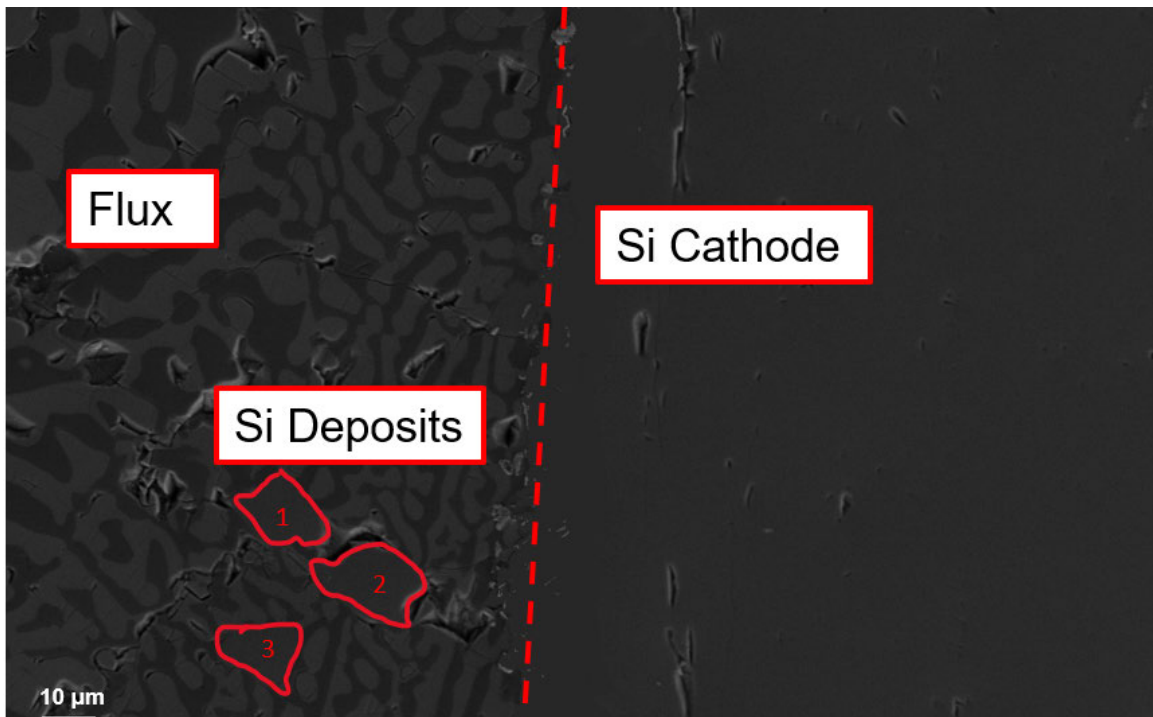


Figure 3.29 SEM Image of the Cathode/Flux Interface after the carbon and Stainless steel-free Electrolysis.

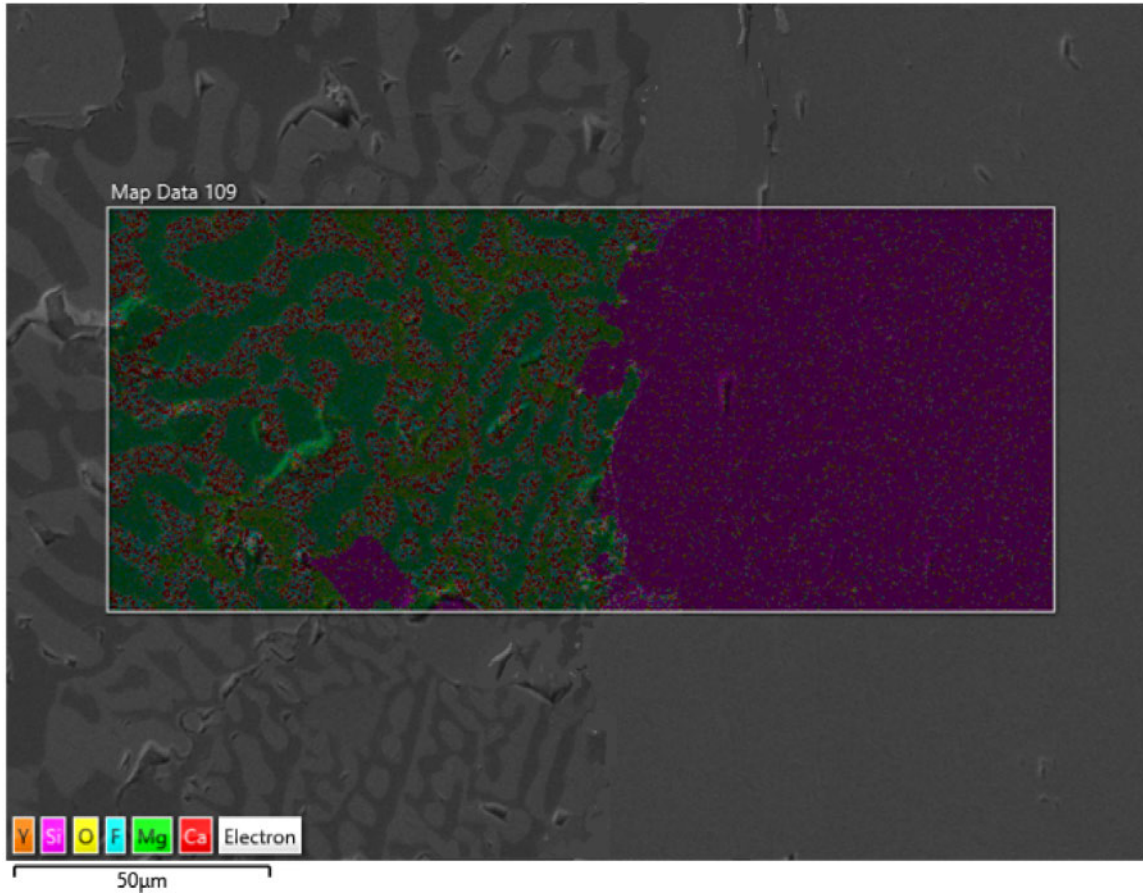


Figure 3.30. EDS Mapping of the Cathode/Flux Interface after the Carbon-free Electrolysis.

Further EDS point analysis conducted on the Si-rich regions within the flux (Si Deposit 1, 2, and 3 in **Figure 29**) reveals that the Si concentration in the silicon deposits averages at 99.3 atomic%, which is identical to that of the Si wafer (**Table 3.5**). Oxygen was detected as the only impurity. These findings provide strong evidence supporting the successful elimination of Si-Mg-O phase and the ability to deposit pure silicon.

Region	Atomic Concentration (%)	
	Si	O
Si Deposit #1	99.6	0.4
Si Deposit #2	99.1	0.9
Si Deposit #3	99.4	0.6
Si Cathode	99.0	1.0

Table 3.5. Composition of the Si Deposits and Si Cathode after the Electrolysis.

3.6 Summary

Chapter 3 of this study focuses on the optimization of Solid Oxide Membrane (SOM) electrolysis for Silicon production, covering three main aspects: the thinning of the Si wafer, the presence of carbon (C) and zirconium (Zr) impurities, and the formation of a Si-Mg-O phase.

The chapter begins by examining the phenomenon of Si wafer thinning during electrolysis. A series of Si stability experiments were conducted, which examines the thinning of the Si wafer as a function of its immersion depth into the flux. The results indicate that the depth of immersion affects the degree of thinning. Based on this understanding, the Si wafer immersion depth for the subsequent Si-SOM experiments was set at 4 cm.

Moving on to the investigation of impurities, the focus shifted to the presence of C and Zr in the silicon deposits. The C impurities were found to originate primarily from the graphite cathode current collector, which was in contact with the Si wafer during electrolysis. By replacing the graphite current collector with a Tungsten one, the formation of silicon carbide (SiC) was eliminated.

In the case of Zr impurities, various theories were proposed on their source and formation mechanism. Validation experiments confirm that the YSZ membrane is the source of Zr impurities. Additionally, the presence of C and SiO₂ in the flux is found to play a crucial role in the formation of Si-Zr-O compounds. To effectively eliminate Zr impurities, it is crucial to ensure the absence of carbon in the system, which requires the implementation of a carbon-free environment in the electrolysis process; achieved by not

using carbon crucible to contain the salt.

Lastly, the formation of a Si-Mg-O phase at the cathode/flux interface was investigated. Thermodynamic analysis and validation experiments were conducted to explain its source and formation mechanism. It was determined that the presence of MgO in the flux leads to the formation of the Si-Mg-O phase. By reducing the content of CaO and SiO₂ in the flux, the formation of MgO, and consequently the Si-Mg-O phase, can be eliminated. The suggested optimal composition of the flux is eutectic CaF₂-MgF₂ with 4 wt% YF₃, 2.5 wt% SiO₂ and 4 wt% CaO.

Successful demonstration of obtaining high purity silicon deposits by following the above-mentioned approach to mitigate the encountered challenges will be further elaborated in Chapter 4.

4. SOM ELECTROLYSIS PROCESS FOR SILICON PRODUCTION

4.1 Experimental Setup

A laboratory-scale Si-SOM electrolysis setup was optimized based on the challenges outlined in Chapter 3. The modifications made to the original setup are highlighted in red in **Figure 1**. These optimizations improved efficiency and reliability of the electrolysis process.

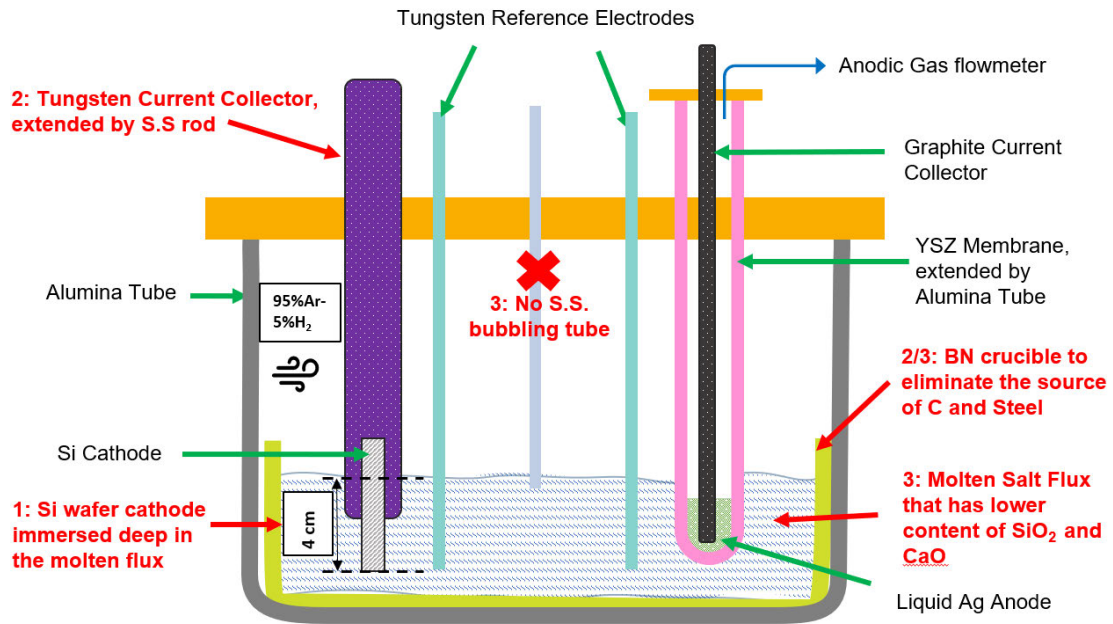


Figure 4.1. Optimized Si-SOM Cell Setup.

To maintain an atmosphere with significantly low level of oxygen and moisture for efficient electrolysis, a gas mixture consisting of 95% argon and 5% hydrogen was passed through a moisture trap filled with Drierite and an oxygen trap filled with heated copper chips. In order to address the issue of Zr impurities in the Si deposits, a boron nitride (BN) crucible was introduced as a replacement for the previous graphite crucible to contain the flux. The BN crucible contained 450 grams of flux which was a eutectic

CaF₂-MgF₂ with 5wt% SiO₂, 9wt% CaO, and 4wt% YF₃. The flux in the BN crucible had sufficient depth to completely immerse the silicon wafer cathode to a depth of 4 cm in the flux. The Si wafer cathode immersion depth was sufficient to prevent its thinning during the electrolysis process.

On the anode side, a one-end closed 8 mol% Yttria Stabilized Zirconia (YSZ) tube separated the flux from 5g of liquid Silver that was enclosed within the YSZ tube. To extend the YSZ tube, an alumina tube was connected using gas-sealing ceramic paste (Aremco 552). A graphite rod immersed in the liquid silver inside the YSZ tube acted as the anode current collector. A digital mass flowmeter was connected to the exit of the anode assembly, which recorded the flowrate of the anodic gas evolution during electrolysis. The faradic efficiency of the cell was calculated by comparing the anodic gas evolution rate and the current-time profile during electrolysis.

On the cathode side, to eliminate the C impurities in the Si deposits, a Tungsten rod was used as the cathode current collector. A slit was precisely created at the end of the rod using Electrical Discharge Machining (EDM). The width of the slit matched the thickness of the silicon wafer used in the electrolysis, ensuring a precise and snug fit. To establish a secure contact between the silicon cathode and the tungsten current collector, the silicon wafer was carefully inserted into the slit and attached using tungsten paste from Nanochemazone. To extend the tungsten rod, a stainless-steel rod was employed. A round hole that matches the size of the tungsten rod was machined at the bottom of the steel rod. The tungsten rod was wrapped with a silver mesh and inserted into the opening at the bottom of the stainless-steel rod. The tungsten rod was then connected to the

stainless-steel extension rod with a set screw (**Figure 4.2**). This meticulous assembly process guaranteed a stable and reliable connection between the cathode and the current collector, enabling effective electrical contact during SOM electrolysis.

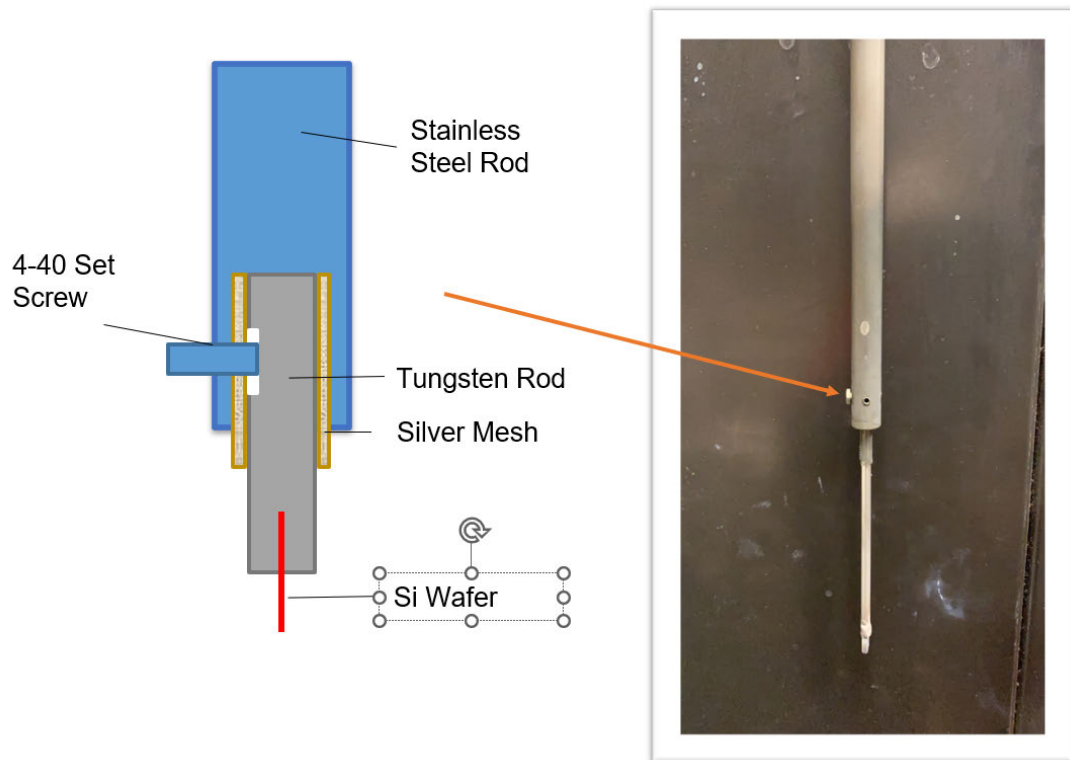


Figure 4.2. Schematics of the Cathode Assembly that consists of Silicon Wafer Cathode, Tungsten Current Collector and Stainless-steel Extension Rod.

During electrolysis, the salt needs to be in a stainless-steel free environment in order to eliminate Mn, Cr and Fe in the Si deposits, the Stainless-steel bubbling tube was not used. The entire SOM cell was placed inside a vertical tube furnace, positioned at the center of the heating zone for optimal temperature distribution. Two electrolysis (Electrolysis 1 and 2) at a steady DC potential of 1.75 V was performed at a temperature of 1150°C for 12 hours each.

4.2 Electrochemical Characterization

4.2.1 Electronic Transference number of the flux

Previous studies have shown an inverse relationship exists between current efficiency in SOM electrolysis and electronic conductivity in the flux [10-15]. Therefore, in order for the SOM electrolysis to operate at high current efficiencies, it is preferable to minimize electronic conductivity in the flux.

The electronic transference number (t_e) is a reliable measure of the electronic conductivity in the flux. The electronic transfer number (t_e) in the flux system is defined as the ratio of electronic conductivity (σ_e) to the total conductivity (σ_{tot}), as shown in **Equation 4-1**. It quantifies the contribution of electronic conductivity to the overall conductivity. As the SOM flux involves only electron and ion transfer, a very low t_e value (close to 0) would indicate that the flux is primarily ionic.

$$t_{e,flux} = \frac{\sigma_{e,flux}}{\sigma_{tot}} \quad \text{Eq 4-1}$$

The electronic and total conductivities in the flux are inversely proportional to the electronic and total resistances, ($R_{e,flux}$) and (R_{tot}), respectively. As other cell parameters do not change during the experiment, the electronic transference number $t_{e,flux}$ can be calculated using **Equation 4-2**.

$$t_{e,flux} = \frac{\frac{1}{R_{e,flux}}}{\frac{1}{R_{tot,flux}}} \quad \text{Eq 4-2}$$

The flux system can be modeled as a parallel combination of two resistors: the ionic resistance and the electronic resistance. The total ohmic resistance (R_{tot}), which

consists of both the electronic and ionic contributions, can be described by the relationship between the ohmic electronic resistance ($R_{e, flux}$) and the ohmic ionic resistance ($R_{i, flux}$), shown in **Equation 4-3** [43].

$$\frac{1}{R_{tot,flux}} = \frac{1}{R_{e,flux}} + \frac{1}{R_{i,flux}} \quad \text{Eq 4-3}$$

Before Electrolysis 1 and after Electrolysis 2, two tungsten reference electrodes were inserted into the flux to measure the total and electronic resistance of the flux. The impedance measured between the two reference electrodes provides the total flux resistance, while the current measured between the electrodes at a very low applied potential provides the electronic resistance. This applied potential was set to 0.01 V, a potential that introduces negligible polarization and is significantly lower than the dissociation potential of any possible metal oxides in the system.

The ionic resistance of the flux can be determined from the measured values of the total resistance and the electronic resistance of the flux using **Equation 4-3**. The electronic transference number can be calculated using **Equation 4-2**. The specific values of the resistances and electronic transference numbers of the flux between the reference electrodes are presented in **Table 4.1**. The results show that the electronic transference number remained low and unchanged during electrolysis. This indicates that the flux was primarily ionic during the entire electrolysis process of 24 hours.

Before Electrolysis				After Electrolysis			
$R_{\text{tot,flux}}$	$R_{\text{e,flux}}$	$R_{\text{i,flux}}$	t_e	$R_{\text{tot,flux}}$	$R_{\text{e,flux}}$	$R_{\text{i,flux}}$	t_e
0.19	7.69	0.194	0.025	0.18	20	0.181	0.009

Table 4.1. Total, Electronic and Ionic resistance of the Flux with the Electronic Transference Number before and after Electrolysis.

4.2.2 Current-Potential Characteristics of the Electrolysis

Potentiodynamic scans (PDS) were carried out at three different stages: before Electrolysis 1, after Electrolysis 1, and after Electrolysis 2. The current-potential relationships are shown in **Figure 4.2**. As the SOM cell has been optimized to minimize the presence of any impurity oxide, negligible amount of leakage current associated with the dissociation of impurity oxides was observed at all three stages. Therefore, there was no need to perform any pre-electrolysis at a potential that is lower than dissociation potential of SiO_2 .

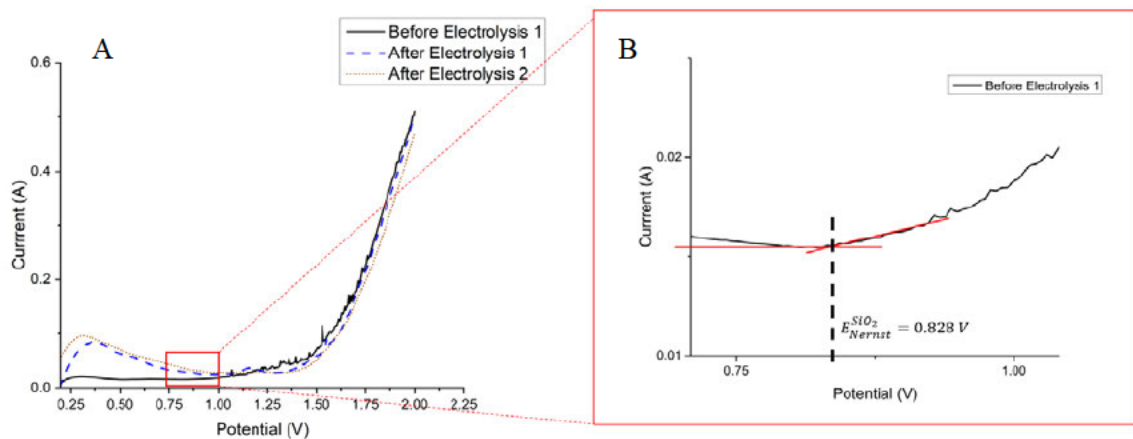


Figure 4.3. PDS showing the Current-Potential Behavior in the potential range of A). 0.2 to 2 V; B). 0.7 to 1.1 V.

The Nernst potential for SiO_2 dissociation can be experimentally determined by finding the first deflection point of the Current-Potential profile. The Nernst potential was

identified to be 0.828 V, which is larger than the standard Nernst potential at the electrolysis temperature of 1150 C (0.51 V). This increase is likely due to the low activity of SiO₂ in the flux. With less SiO₂ available in the flux, it becomes more difficult (requires more energy) to drive the reaction. A detailed explanation is provided in section 4.4.2.1.

The total resistance of the cell ($R_{tot,cell}$) can be determined by calculating the reciprocal of the slope of the current-potential profile at potentials above the dissociation potential of silica ($E > 1.7$ V). The ohmic resistance of the cell ($R_{ohmic,cell}$) was measured by EIS across the anode and cathode. The value of $R_{ohmic,cell}$ was determined by finding the high-frequency intercept on the real axis of the Nyquist plot [45, 46]. The total resistance and ohmic resistance of the cell at different stages are shown in **Table 4.2**. The results show that the total resistance of the cell remained low during the electrolysis. The ohmic resistance increased by 16%, which is likely attributed to the oxidation of graphite anode current collector.

	Before Electrolysis 1	After Electrolysis 1	After Electrolysis 2
$R_{tot,cell}$ (Ω)	0.885	0.909	1.010
$R_{ohmic,cell}$ (Ω)	0.324	0.338	0.375

Table 4.2. Total and Ohmic Resistance of the SOM Cell before Electrolysis 1, after Electrolysis 1 and After Electrolysis 2.

Based on the geometry of the YSZ membrane and effective area of anode/YSZ interface, the ionic resistance of YSZ involved during the dissociation of Silica ($R_{i(YSZ)}^{SiO_2}$) is calculated to be 0.25 Ω . [6] This suggests that the YSZ membrane is the major

component that contributes to the ohmic resistance of the SOM cell. The cathode assembly of the SOM cell is believed to provide low ohmic resistance and maintained reliable electrical contact throughout the electrolysis process.

4.2.3 Current-Time Profile and Faradic Efficiency of the Electrolysis

The electrolysis was performed twice at 1.75V, each for 12 hours. A moderate overpotential was selected as it allows for an adequate current for silicon deposition while potentially promoting the planar growth of the deposits at the cathode. The current-time profile of each electrolysis is shown in **Figure 4.4**. The profile suggests that the current remained steady during each electrolysis, and it was not limited by mass transfer. Total charge that passed through the cell was 12176 C. Assuming 100% current efficiency, 0.88 gram of silicon would be produced.

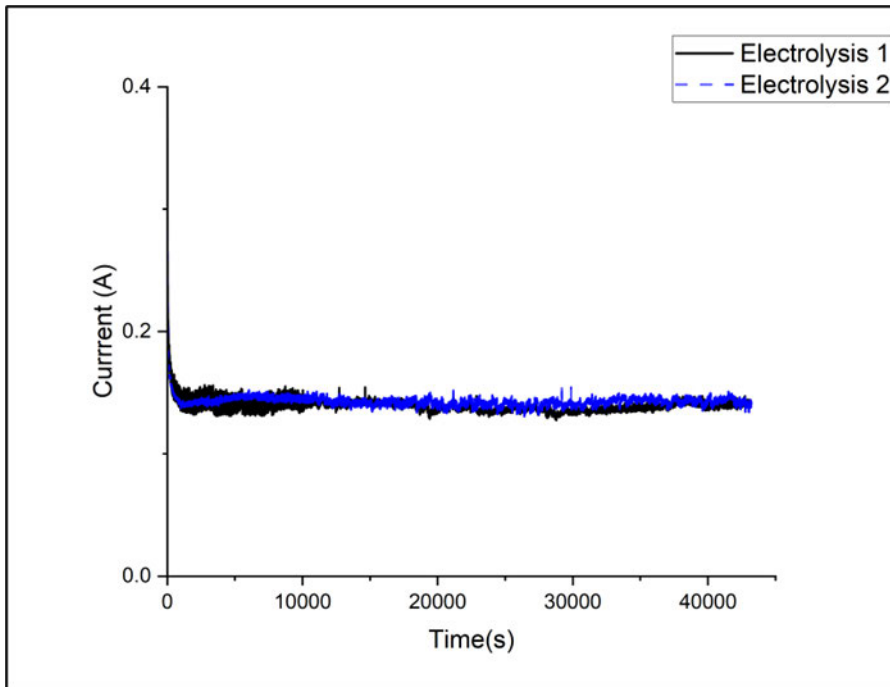


Figure 4.4. Current-Time Plots during Electrolysis 1 and Electrolysis 2 with applied potential of 1.75 V for 12 hrs each.

During each electrolysis, the gas produced at the anode was passed through a digital mass flow meter, which measured the rate of anodic gas evolution. The measured gas evolution rate was then used to calculate the Faradaic current. By comparing the Faradaic current and current profile shown in **Figure 4.4**, the current efficiency of each electrolysis can be calculated. The resulting current efficiency are presented in **Figure 4.5**. It is observed that the current efficiency exhibited a slight increase during the initial 10,000 seconds of Electrolysis 1. This can be attributed to the fact that it takes some time for oxygen to fully saturate the liquid Ag anode before evolution occurs. As a result, the measurement of gases at the anode during this early period might be an underestimate of the actual gas produced in the liquid silver anode. This leads to a lower estimation of the Faradaic current and consequently a slightly lower current efficiency value. After the initial 10000 seconds of Electrolysis 1, the current efficiency remained stable around 60%. The current efficiency of Electrolysis 2 increased to an average of 78%, which might be attributed to the increase in the electronic resistance of the flux shown in **Table 4.1**. Based on the current efficiency of each electrolysis, the production of Si was estimated to be 0.60 gram. Overall, it is evident that both instances of electrolysis were stable and relatively efficient throughout the process; leaks in the system are the likely cause of not seeing higher efficiencies.

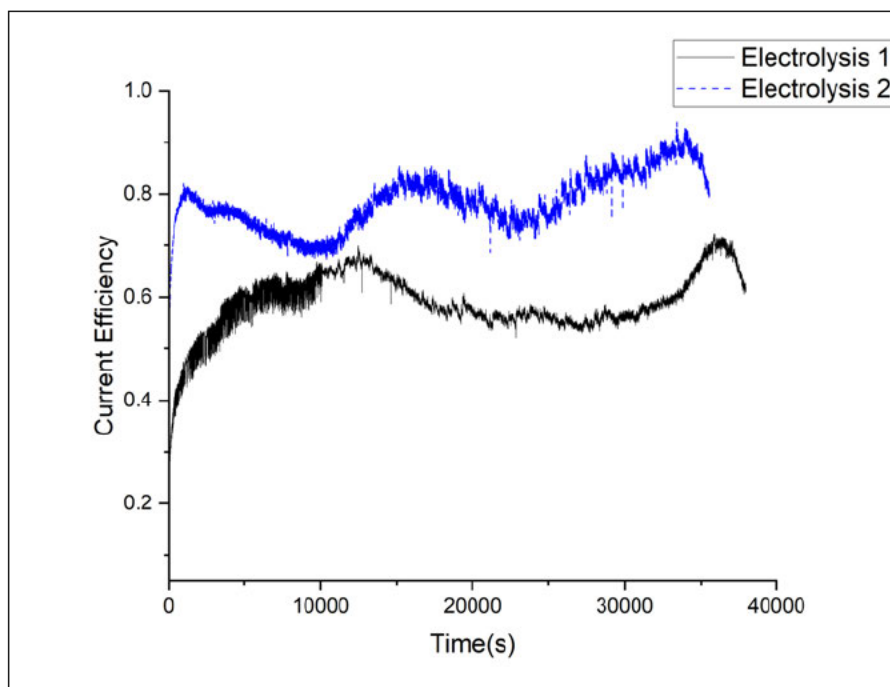


Figure 4.5. Current Efficiency during Electrolysis 1 and Electrolysis 2.

4.3 Post-experimental Characterization

After the SOM electrolysis experiment, the furnace was cooled, and the setup was disassembled. Silicon cathode with flux was sectioned, mounted in epoxy and evaluated under optical microscopy and SEM with EDS capability. **Figure 4.6** shows the optical microscopy image of Si deposits at the interface between cathode and flux. The EDS mapping of the collected silicon shows no detectable impurities such as C and Zr (**Figure 4.7**). Further EDS spot analysis confirms that the deposits consist of 99 atomic % silicon, which is equivalent to the Si purity in the silicon wafer cathode. (**Figure 4.8**). The Si purity in the deposits should be higher as the oxidation inevitably occurred during the materials transfer and polishing of the sectioned sample.

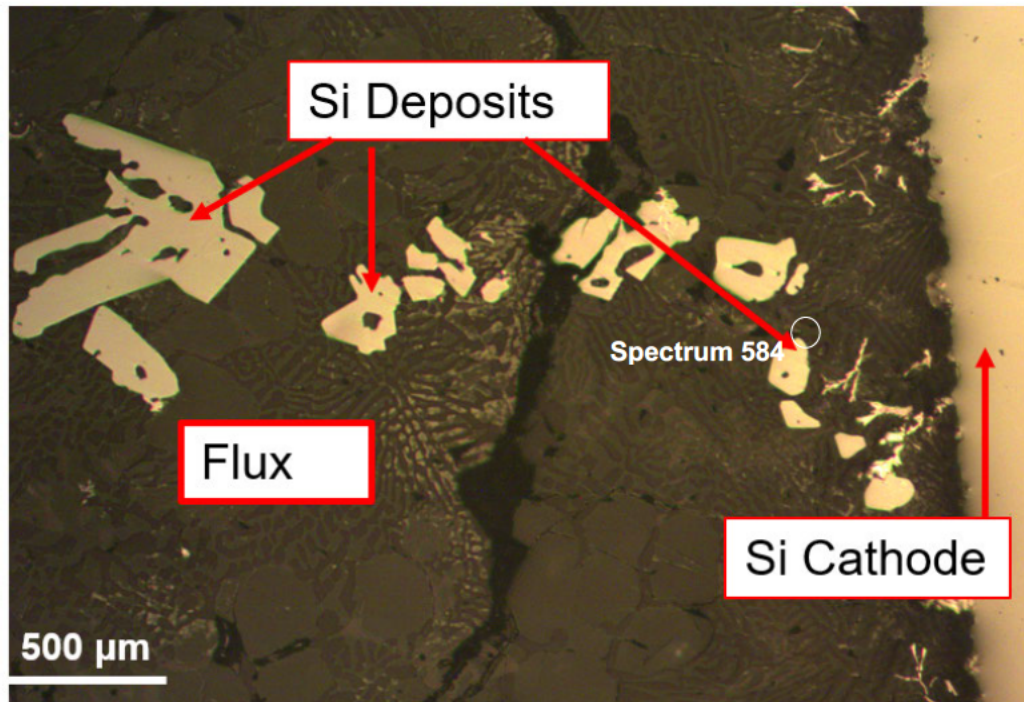


Figure 4.6. Optical Microscopy Image (10X) of the Cathode/Flux Interface after Electrolysis.

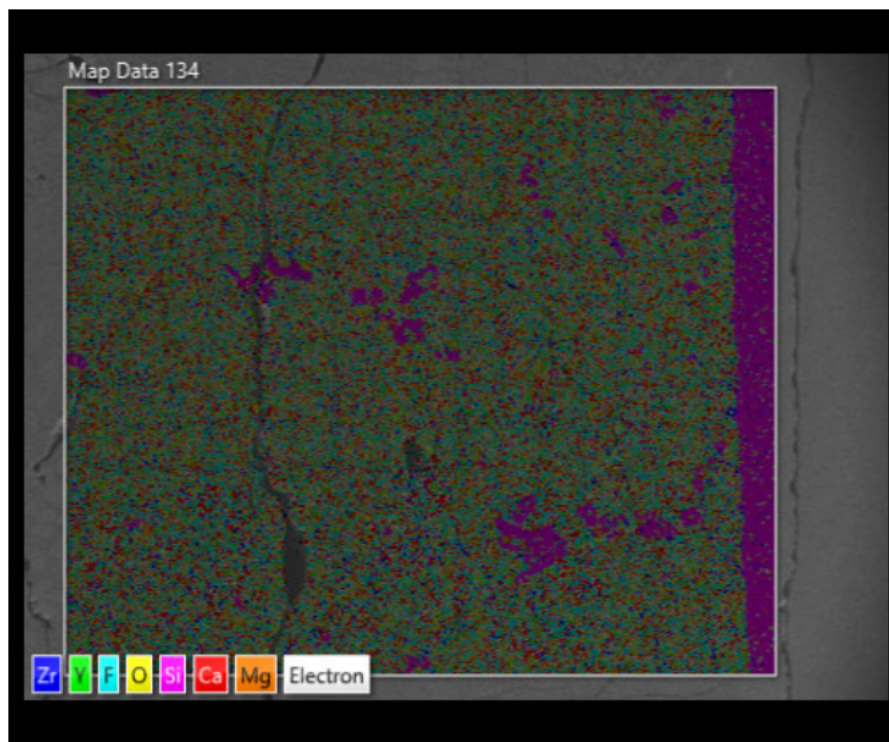


Figure 4.7. EDS mapping of the Cathode/Flux Interface.

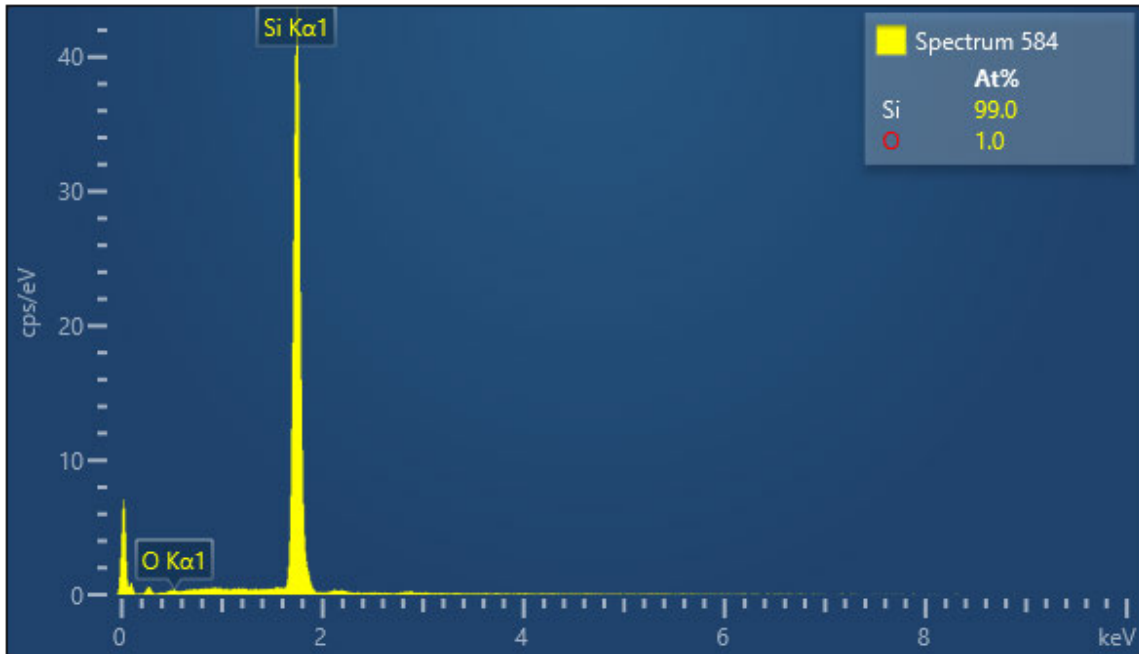


Figure 4.8. EDS Spot Analysis of the Silicon Deposits near the Cathode/Flux Interface.

A dense layer of Tungsten Silicide (WSi_2) with a thickness of $130 \mu\text{m}$ was observed at the interface between tungsten current collector and flux (**Figure 4.9**). As tungsten (2700 S/cm) is more conductive than silicon (120 S/cm) at the electrolysis temperature, reduced silicon tends to accumulate at the tungsten/flux interface. Following that, tungsten atoms from the current collector diffused to the silicon deposits and formed WSi_2 . The uniform distribution of W and Si observed in the EDS mapping in **Figure 4.10** suggests that tungsten diffusion into the silicon deposits is faster than the formation of additional silicon deposits. Consequently, once the reduced silicon accumulates at the tungsten/flux interface, it stabilizes and reacts with the diffusing tungsten atoms to form a dense and planar layer of WSi_2 .

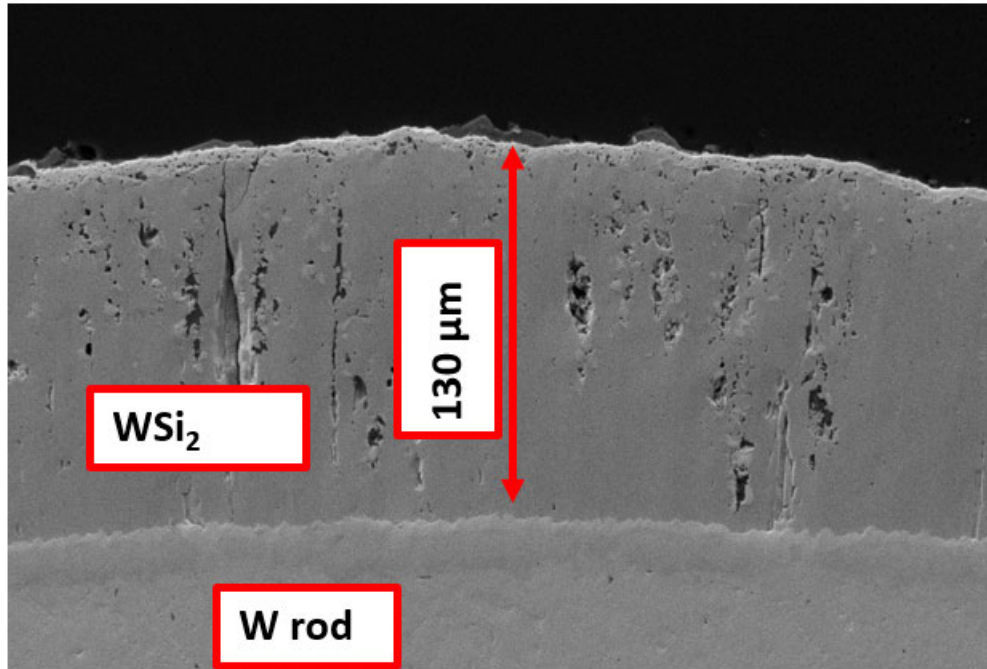


Figure 4.9. SEM Image of the Tungsten Current Collector that was Immersed in the Flux during Electrolysis.

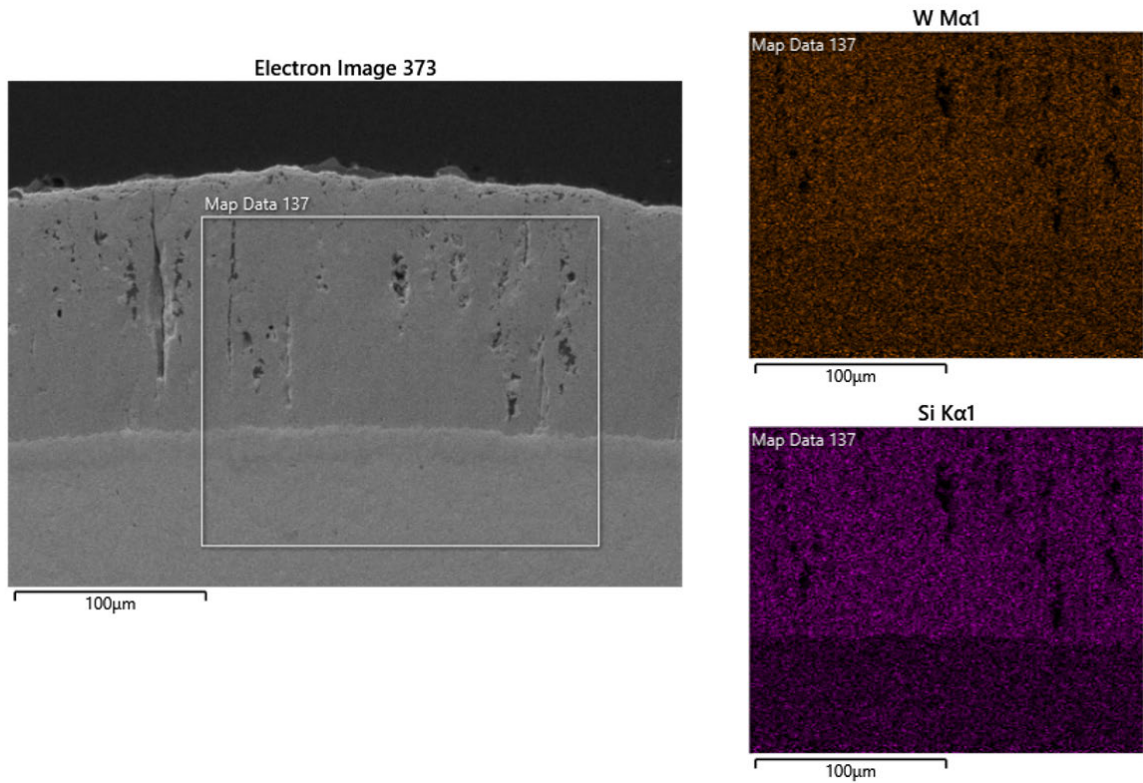


Figure 4.10. EDS Mapping of the Tungsten Current Collector that was Immersed in the Flux during Electrolysis.

The WSi_2 layer with a similar thickness was also observed in other regions of the tungsten current collector that were immersed in the flux. Based on the thickness of the WSi_2 layer and length of tungsten current collector that was immersed in the flux, the total silicon deposits at the tungsten/flux interface were calculated as 0.20 gram. However, the estimated production of silicon was 0.60 gram. The relatively low observed yield (33%) can be attributed to the significant presence of widely dispersed Si deposits throughout the flux, as seen in **Figure 4.6**. However, due to the irregular geometry and nonuniform distribution of these deposits within the flux, it is not feasible to accurately quantify their overall masses.

4.4 Electrochemical Modelling

4.4.1 Equivalent Circuit Modelling of the SOM Electrolysis Process

To gain a comprehensive understanding of the electrochemical behavior of the SOM cell and explore methods for reducing the cell overpotential, it is important to develop the electrochemical modeling of the SOM electrolysis process. Equivalent circuit modeling is a useful tool to represent the SOM electrolysis process. Guan et al. have previously introduced a generic equivalent DC circuit model that incorporates the known mechanisms involved in current flow, including [12, 15, 30, 31]:

- (1) the dissociation of the desired oxide,
- (2) the dissociation of impurity oxides,
- (3) electronic conductivity of the molten flux, and
- (4) the various resistive contributions of the SOM cell.

A similar equivalent DC circuit model is established for the Si production, shown in **Figure 4.11**. The corresponding symbols are defined in **Table 4.3**.

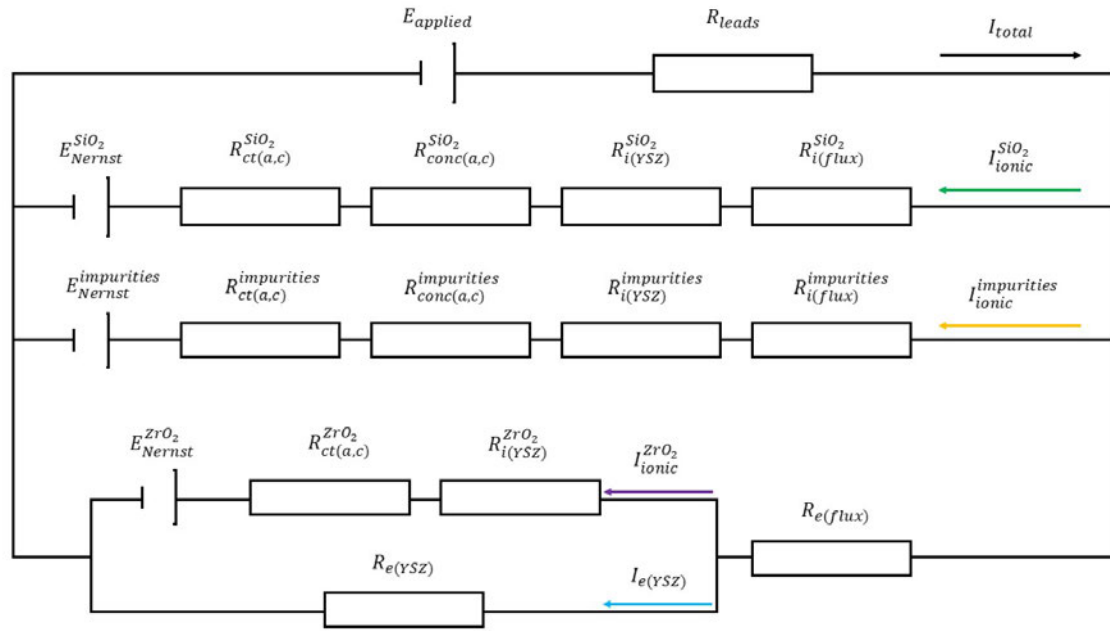


Figure 4.11. Equivalent Circuit of the SOM Process for Silicon Production.

Symbols	Definition
$E_{applied}$	Applied Potential
$E_{Nernst}^{SiO_2}$	Nernst Potential for SiO_2
$E_{Nernst}^{Impurities}$	Nernst Potential for impurity oxides
$E_{Nernst}^{ZrO_2}$	Nernst Potential for ZrO_2
R_{leads}	Resistance of Lead wires and current collectors
$R_{ct(a,c)}^{SiO_2}$	Charge Transfer Resistance at the Anode and Cathode for SiO_2 dissociation
$R_{conc(a,c)}^{SiO_2}$	Concentration Polarization Resistance at the Anode and Cathode for SiO_2 dissociation
$R_{i(YSZ)}^{SiO_2}$	Ionic resistance of YSZ membrane involved in SiO_2 dissociation
$R_{i(Flux)}^{SiO_2}$	Ionic resistance of Flux involved in SiO_2 dissociation
$R_{ct(a,c)}^{Impurities}$	Charge Transfer Resistance at the Anode and Cathode for Impurity oxide dissociation

$R_{conc(a,c)}^{Impurities}$	Concentration Polarization Resistance at the Anode and Cathode for Impurity Oxide dissociation
$R_i^{Impurities(YSZ)}$	Ionic resistance of YSZ membrane involved in Impurity Oxide dissociation
$R_i^{Impurities(Flux)}$	Ionic resistance of Flux involved in Impurity Oxide dissociation
$R_{ct(a,c)}^{ZrO_2}$	Charge Transfer Resistance at the Anode and Cathode for ZrO_2 dissociation
$R_i^{ZrO_2(YSZ)}$	Ionic resistance of YSZ membrane involved in ZrO_2 dissociation
$R_e(YSZ)$	Electronic resistance of the YSZ Membrane
$R_e(Flux)$	Electronic resistance of the Flux between the YSZ Membrane and the Cathode
I_{total}	Total current in the system
$I_{ionic}^{SiO_2}$	Ionic current for SiO_2 Dissociation
$I_{ionic}^{ZrO_2}$	Ionic current for ZrO_2 Dissociation
$I_{ionic}^{Impurities}$	Ionic current for Impurity Oxide Dissociation
$I_{e(YSZ)}$	Electronic Current that passes through the YSZ membrane

Table 4.3. Definitions of Symbols in the SOM equivalent circuit.

As the SOM cell has been optimized to minimize the presence of impurity oxides, the current pathway associated with the dissociation of impurity oxides can be ignored. The PDS scan in Figure 2 also confirms that no dissociation of impurity oxides was observed. Since the flux was primarily ionic and ZrO_2 has negligible solubility in the flux, dissociation of ZrO_2 is also unlikely to occur. The dissociation of ZrO_2 is further mitigated by performing the electrolysis at a potential that is lower than the dissociation potential of ZrO_2 . Another possible current pathway is the electronic current that passes through the flux. Since the flux was identified to be primarily ionic suggested by **Table 4.1**, negligible electronic current passes through the flux. Therefore, the SOM system is

left with one primary pathway for current to pass through, which is the dissociation of SiO_2 . A simplified equivalent DC circuit is established, shown in **Figure 4.12**.

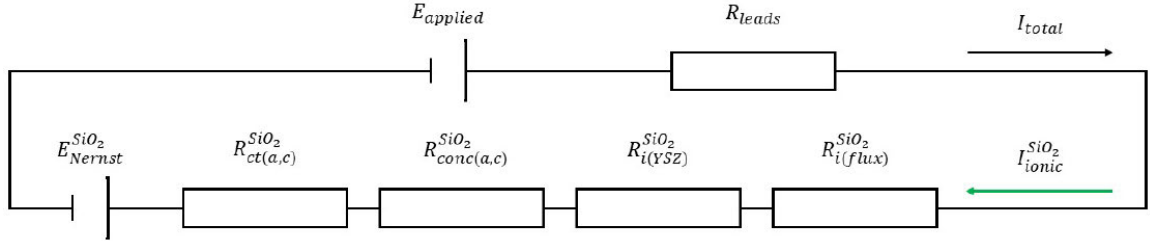


Figure 4.12. Simplified Equivalent Circuit for the Optimized Si-SOM Process.

4.4.2 Polarization Model of the Si-SOM process

Based on the simplified equivalent DC circuit, the applied potential on the system can be expressed by Equation 4-4:

$$E_{applied} = |E_{Nernst}^{SiO_2}| + \eta_{ohm} + \eta_{ct(a,c)} + \eta_{conc,c} + \eta_{conc,a} \quad \text{Eq 4-4}$$

where $|E_{Nernst}^{SiO_2}|$ is the absolute value of the Nernst potential for SiO_2 dissociation, η_{ohm} is the ohmic polarization of the SOM cell, $\eta_{ct(a,c)}$ is the charge transfer polarization in the SOM cell, $\eta_{conc,c}$ is the cathodic concentration polarization, and $\eta_{conc,a}$ is the anodic concentration polarization.

4.4.2.1 Nernst potential for SiO_2 Dissociation

The Nernst potential for SiO_2 dissociation is given by Equation 4-5 when CO is evolved at the anode:

$$E_{Nernst}^{SiO_2} = E_{Nernst}^{\circ SiO_2,CO} + \frac{RT}{nF} \ln \left(\frac{a_{SiO_2(flux)} a_{C(anode)}^2}{a_{Si(cathode)} a_{CO(g)}^2 (YSZ/anode)} \right) \quad \text{Eq 4-5}$$

where $E_{Nernst}^{SiO_2}$ is the Nernst potential for the dissociation of silica, $E_{Nernst}^{\circ SiO_2,CO}$ is the standard Nernst potential for the dissociation of silica when CO is formed at the anode, R is the ideal gas constant (8.314 J mol⁻¹ K⁻¹), T is the temperature of the system (K), n is the number of moles of electrons transferred in the reaction (4 mol), F is the Faraday's constant (96485 C mol⁻¹), $a_{SiO_2(flux)}$ is the activity of silicon oxide dissolved in the flux, $a_{C(anode)}$ is the activity of carbon at the anode, $a_{Si(cathode)}$ is the activity of silicon in the cathode, and $a_{CO(g) (YSZ/anode)}$ is the activity of carbon monoxide gas at the anode/YSZ interface. In this SOM cell, $a_{Si(cathode)}$ and $a_{C(anode)}$ at the anode can be treated as unity. The activity of carbon monoxide gas is equivalent to the partial pressure of carbon monoxide at the YSZ/anode interface, $P_{CO(g) (YSZ/anode)}$. Therefore, the Nernst potential for SiO₂ dissociation can be expressed as follows:

$$E_{Nernst}^{SiO_2} = E_{Nernst}^{\circ SiO_2,CO} + \frac{RT}{nF} \ln \left(\frac{a_{SiO_2(flux)}}{P_{CO(g) (YSZ/anode)}^2} \right) \quad \text{Eq 4-6}$$

It is possible that CO₂ is evolved at the anode when the electrolysis starts. The Nernst Potential for SiO₂ dissociation when CO₂ is formed at the anode can be expressed as follows:

$$\begin{aligned} E_{Nernst}^{SiO_2} &= E_{Nernst}^{\circ SiO_2,CO_2} + \frac{RT}{nF} \ln \left(\frac{a_{SiO_2(flux)} a_{C(anode)}}{a_{Si(cathode)} a_{CO_2(YSZ/anode)}} \right) \\ &= E_{Nernst}^{\circ SiO_2,CO_2} + \frac{RT}{nF} \ln \left(\frac{a_{SiO_2(flux)}}{P_{CO_2(YSZ/anode)}} \right) \end{aligned} \quad \text{Eq 4-7}$$

where $E_{Nernst}^{\circ SiO_2,CO_2}$ is the standard Nernst potential for the dissociation of silica when CO₂ is formed at the anode, $P_{CO_2(YSZ/anode)}$ is the partial pressure of carbon dioxide at the

YSZ/anode interface.

$E_{Nernst}^{\circ SiO_2,CO}$ and $E_{Nernst}^{\circ SiO_2,CO_2}$ are calculated to be 0.51 V and 0.70 V respectively.

$a_{SiO_2(flux)}$ is calculated to be $2.29 \cdot 10^{-3}$ using the equilibrium module in FactSage.

$P_{CO(g)}(YSZ/anode)$ or $P_{CO_2(YSZ/anode)}$ is established by the activity of carbon

($a_{C(anode)} = 1$) at the anode and partial pressure of oxygen in the air ($P_{O_2,air} =$

0.21 atm) prior to the electrolysis. Therefore, the estimated $E_{Nernst}^{SiO_2}$ varies between 0.59

– 0.83 V, depending on the ratio of CO and CO₂ formed at the anode. This range aligns

well with the experimental observation of $E_{Nernst}^{SiO_2}$ ($E_{Nernst}^{SiO_2} = 0.828$ V).

Notably, the FactSage simulation tend to underestimate the interaction between solvent and solute within a molten salt system, so the exact activity of SiO₂ in the flux might be lower. The calculated value of $E_{Nernst}^{SiO_2}$ is likely to exceed the estimated range of 0.59 – 0.83 V. As a result, it is not reliable to determine the ratio of CO and CO₂ formed at the anode by comparing the calculated range of $E_{Nernst}^{SiO_2}$ and experimental observation.

4.4.2.2 Ohmic Polarization

The ohmic polarization (η_{ohm}) in the SOM electrolysis cell can be defined as:

$$\eta_{ohm} = iR_{ohmic,cell} \quad \text{Eq 4-7}$$

The total ohmic resistance for the electrolytic cell (R_{cell}) is the sum of the YSZ membrane ionic resistance ($R_{i(YSZ)}^{SiO_2}$), the flux ionic resistance ($R_{i(Flux)}^{SiO_2}$), the electrodes resistance, the lead wires resistance, and the contact resistances between the interfaces (R_{leads}). The ohmic resistance (R_{cell}) can be measured by Electrochemical Impedance

Spectroscopy (EIS) measurements between the anode current collector and the cathode current collector.

4.4.2.3 Activation Polarization

The activation polarization ($\eta_{ct(a,c)}$) represents the extra potential required to overcome the activation energy barrier for charge transfer reactions at the electrode/electrolyte interface. It can be described by the Butler-Volmer equation (Equation 4-7), which relates ($\eta_{ct(a,c)}$) to the cell current (i) for conditions of small currents and/or rapid mass transfer. [47, 48]

$$i = i_0 \exp\left(\frac{\alpha n \eta_{ct(a,c)} F}{RT}\right) - i_0 \exp\left(\frac{-(1 - \alpha) n \eta_{ct(a,c)} F}{RT}\right) \quad \text{Eq 4-8}$$

where i_0 is the exchange current, α is the transfer coefficient, and $n = 4$ is the number of electrons transferred. The activation overpotentials at both the anode and cathode are combined into one overpotential, $\eta_{ct(a,c)}$. The exchange current i_0 , is a measure of the electrocatalytic activity at the electrode/electrolyte interface in an electrochemical reaction. Its value depends on the specific operating conditions and the material properties involved. Assuming a symmetric activation energy barrier for both electrode reactions, a transfer coefficient of 0.5 is suggested. Equation 4-7 can be then solved for $\eta_{ct(a,c)}$ as a function of i .

$$\eta_{act} = \frac{RT}{2F} \ln \left[\left(\frac{i}{2i_0} \right) + \sqrt{\left(\frac{i}{2i_0} \right)^2 + 1} \right] \quad \text{Eq 4-9}$$

4.4.2.4 Cathodic Concentration Polarization

The cathodic concentration polarization, $\eta_{conc,c}$, is attributed to the transport of SiO_2 across the diffusion boundary layer at the cathode surface [47]. This overpotential can be represented as follows:

$$\eta_{conc,c} = \frac{RT}{4F} \ln \left(\frac{a_{\text{SiO}_2(\text{flux})}^0}{a_{\text{SiO}_2(\text{flux})}^{(i)}} \right) \quad \text{Eq 4-10}$$

where $a_{\text{SiO}_2(\text{flux})}^0$ is the activity of SiO_2 in the bulk flux, and $a_{\text{SiO}_2(\text{flux})}^{(i)}$ is the activity of SiO_2 at the cathode/flux interface for a certain current density. Assuming a Henrian solution, Eq. 4-10 can be expressed as:

$$\eta_{conc,c} = \frac{RT}{4F} \ln \left(\frac{C_{\text{SiO}_2(\text{flux})}^0}{C_{\text{SiO}_2(\text{flux})}^{(i)}} \right) \quad \text{Eq 4-11}$$

where $C_{\text{SiO}_2(\text{flux})}^0$ and $C_{\text{SiO}_2(\text{flux})}^{(i)}$ are the concentration of SiO_2 in the bulk flux and at the cathode/flux interface.

The diffusion of SiO_2 at the cathode surface is driven by the concentration gradient. Assuming a linear concentration profile within the diffusion layer, the flux of SiO_2 due to diffusion at the cathode surface can be described using Fick's first law as follows:

$$J_{\text{SiO}_2, \text{Cathode/Flux}} = -D_{\text{SiO}_2(\text{flux})} \frac{dC_{\text{SiO}_2(\text{flux})}}{dx} = \quad \text{Eq 4-12}$$

$$-D_{\text{SiO}_2(\text{flux})} \frac{C_{\text{SiO}_2(\text{flux})}^{(i)} - C_{\text{SiO}_2(\text{flux})}^0}{\delta_c}$$

where $D_{\text{SiO}_2(\text{flux})}$ is the diffusion coefficient of SiO_2 in the flux, and δ_c is the thickness of the diffusion layer at the cathode surface.

The diffusive flux $J_{\text{SiO}_2, \text{Cathode/Flux}}$ can be then related to the cell current i :

$$i = 2FA_c J_{\text{SiO}_2, \text{Cathode/Flux}} = -4FA_c D_{\text{SiO}_2(\text{flux})} \frac{C_{\text{SiO}_2(\text{flux})}^{(i)} - C_{\text{SiO}_2(\text{flux})}^0}{\delta_c} \quad \text{Eq 4-13}$$

where A_c is the effective cathode's area for the electrochemical half-cell reaction: $\text{Si}^{4+} + 4e^- = \text{Si}$.

The mass transport limit of SiO_2 occurs when $C_{\text{SiO}_2(\text{flux})}^{(i)} = 0$. The value of the current under this condition is defined as the cathodic limiting current, $i_{1,c}$:

$$i_{1,c} = 4FA_c D_{\text{SiO}_2(\text{flux})} \frac{C_{\text{SiO}_2(\text{flux})}^0}{\delta_c} \quad \text{Eq 4-14}$$

Solving **Eq 4-10** through **4-13**, $\eta_{\text{conc},c}$ can be expressed as a function of i :

$$\eta_{\text{conc},c} = \frac{RT}{4F} \ln \left(\frac{i_{1,c}}{i_{1,c} - i} \right) \quad \text{Eq 4-15}$$

4.4.2.5 Anode Concentration Overpotential

In this work, graphite was employed as the anode current collector, and CO or CO_2 evolved at the anode during the electrolysis. It is important to note that CO or CO_2 is formed when the oxygen gas leaves the liquid silver anode and reacts with carbon within the anode current collector. When a potential that exceeds the dissociation potential of silica is applied, oxygen ions migrate through the YSZ membrane to liquid silver anode and are oxidized at the YSZ/anode interface. Once the oxygen in the silver reaches its saturation limit, it bubbles out of the silver and reacts with the C forming CO or CO_2 .

Thus, as the electrolysis proceeds, the oxygen pressure at the liquid silver anode/YSZ interface must exceed 1 atm in order to bubble out of the liquid silver. The difference in pressure within the liquid silver and at the liquid silver anode/YSZ interface generates an overpotential. The anodic overpotential can be expressed as follows:

$$\eta_{\text{conc, a}} = \frac{RT}{4F} \ln \left(\frac{P_{\text{O}_2(\text{Ag})}^{\text{b}}}{1\text{atm}} \right) \quad \text{Eq 4-16}$$

where $P_{\text{O}_2(\text{Ag})}^{\text{b}}$ is the oxygen pressure required for bubble formation at the liquid silver anode/YSZ interface. Since the oxygen evolved during the electrolysis forms bubbles at the YSZ/anode interface, there is negligible concentration polarization resulting from the diffusion of oxygen atoms within the liquid silver anode.

4.4.2.6 Current-Potential Relationship in Polarization Modeling

The relationship between the applied voltage and the cell current for SOM electrolysis can be determined by substituting **Equations 4-7, 4-9, 4-15** and **4-16** into Equation 4-4:

$$E_{\text{applied}} = |E_{\text{N}}^{\text{SiO}_2}| + iR_{\text{ohm, cell}} + \frac{RT}{2F} \ln \left[\left(\frac{i}{2i_0} \right) + \sqrt{\left(\frac{i}{2i_0} \right)^2 + 1} \right] + \frac{RT}{4F} \ln \left(\frac{i_{1,c}}{i_{1,c} - i} \right) + \frac{RT}{4F} \ln \left(\frac{P_{\text{O}_2(\text{Ag})}^{\text{b}}}{1\text{atm}} \right) \quad \text{Eq 4-17}$$

The current-potential curve obtained from PDS measurement can be modeled using **Equation 4-17** to analyze various polarization losses and determine unknown parameters, such as the exchange current, the cathodic limiting current, and the oxygen partial pressure required for bubble formation at the anode/YSZ interface.

4.4.2.7 Curve Fitting of the Measured Current-Potential Relationship.

The current-potential curve obtained before the first electrolysis experiment was used for curve fitting (**Figure 2**). The dissociation potential of silica $|E_N^{SiO_2}|$ was identified at 0.828 V. The current at 0.828 V (0.01547 A) was used as the baseline for curve fitting. The difference between the measured current and the baseline current is referred to as the net current. The ohmic resistance of the SOM cell ($R_{ohmic,cell}$) was measured to be 0.324 Ω (see **Table 3**). The fitting potential range chosen was from 0.828 V to 1.028 V, where the current is small, and the cathodic concentration polarization is negligible. No mass-transfer-limited behavior was observed in the PDS. Therefore, the current-potential relationship can be simplified as follows:

$$E_{\text{applied}} = |E_N^{SiO_2}| + iR_{ohm,cell} + \frac{RT}{2F} \ln \left[\left(\frac{i}{2i_0} \right) + \sqrt{\left(\frac{i}{2i_0} \right)^2 + 1} \right] + \frac{RT}{4F} \ln \left(\frac{P_{O_2(Ag)}^b}{1\text{atm}} \right) \quad \text{Eq 4-18}$$

The parameters used for the curve fittings were $R_{ohmic,cell} = 0.323 \Omega$, $|E_N^{SiO_2}| = 0.828 \text{ V}$, the operating temperature T , the gas constant R , and the Faraday constant F . The exchange current i_0 and the oxygen partial pressure for bubble formation at the Ag/YSZ interface $P_{O_2(Ag)}^b$ were the two unknown fitting parameters. The curve fitting results are shown in **Figure 4.13**, with $i_0 = 3 * 10^{-4} \text{ A}$ and $P_{O_2(Ag)}^b = 1.80 \text{ atm}$. Previous research has demonstrated that the charge transfer reaction at the interface between the liquid metal electrode and the Ytria-stabilized zirconia (YSZ) membrane is fast. [49 - 52] As a result, it is believed that the exchange current value is primarily constrained by factors such as

the structural properties and surface roughness of the cathodic material, as well as the concentration of SiO_2 present on the cathodic surface. The fitted value of $P_{\text{O}_2(\text{Ag})}^b$ confirms the assumption that oxygen bubbles evolve from the liquid Ag only when the oxygen partial pressure exceeds atmospheric pressure.

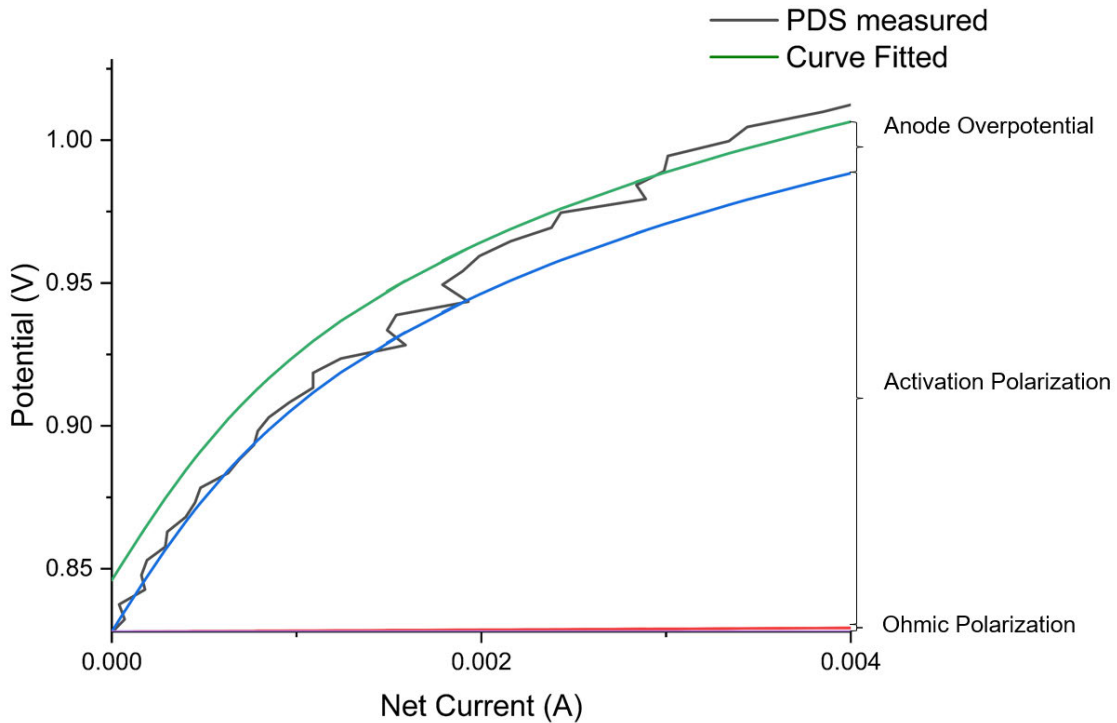


Figure 4.13. Curve Fitting of Measured Applied Potential and Net Current.

When the curve fitting results are extended to a wider potential range from 0.828 V to 2.0 V, the deviation between the fitted curve and the PDS scan increases, primarily due to cathodic concentration polarization (See **Figure 12**). During the PDS scan, the thickness of the diffusion layer (δ_c) continually increases, leading to a non-steady state condition and making it difficult to calculate the cathodic limiting current $i_{1,c}$. However, considering the relatively accurate curve fitting results at the low potential range (See **Figure 4.14**), the difference between the PDS measurement potential and the curve fitted

potential can be attributed to the contribution of cathodic concentration polarization at potentials higher than 1.028 V.

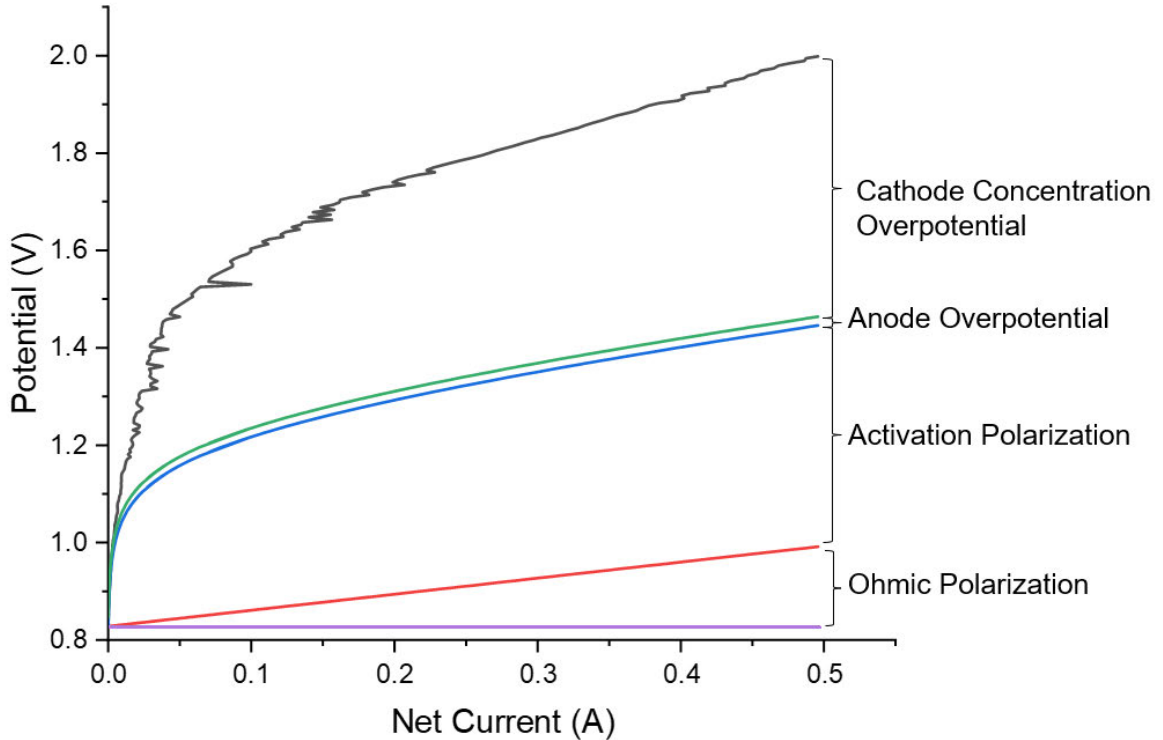


Figure 4.14. Ohmic, Activation, Anode Overpotential and Cathodic Concentration Polarization as a function of the Net Current by Modeling on the SOM cell.

Based on the polarization fitting over the range from 0.828 V to 2.0 V, it is seen that the activation polarization loss dominates at low potentials ($E < 1.028\text{V}$). The cathodic concentration polarization loss became significant at high potentials. At the electrolysis potential of 1.75 V, the activation polarization loss and cathodic concentration polarization loss are the two major contributors to the overall polarization loss, accounting for 50% and 40% respectively. The high activation polarization loss, or low electrocatalytic activity on the cathode/flux interface, may also explain poor adhesion of silicon deposits on the cathode.

To improve the performance of the SOM electrolysis, it is important to reduce losses from cathodic concentration polarization, activation polarization, and ohmic polarization. The concentration polarization can be reduced by facilitating mass transfer near the cathode with gas stirring. The activation polarization loss can be lowered by increasing the electrocatalytic activity of the electrodes (changing the electrode materials). The ohmic polarization loss appears to be the least dominant in the Si-SOM system. It can be reduced by decreasing the thickness of the YSZ membrane, as the ionic resistance of YSZ was identified to be the major contributor of the ohmic resistance of the cell.

4.5 Summary

Chapter 4 demonstrates the feasibility of depositing high purity silicon via SOM electrolysis with the optimized experimental setup, and presents electrochemical characterization, post-experimental characterization and electrochemical modelling of the SOM cell.

The experimental setup section provides details about the modifications made to the Si-SOM setup, such as the use of specific materials and components, to address the challenges identified in Chapter 3 and improve the efficiency and reliability of the electrolysis process.

The electrochemical characterization section discusses the electronic transference number of the flux, current-potential characteristics of the electrolysis, and current-time profile and faradic efficiency of the electrolysis process. The electronic transference

number remained low and unchanged during electrolysis, indicating that the SOM flux is primarily ionic. The current-potential profile and electrochemical impedance spectroscopy (EIS) measurements taken at different stages of the electrolysis process suggest that total and ohmic resistance within the cell were low throughout the entire electrolysis process. Current-time profile and associated Faraday efficiency indicate a stable electrolysis process with high Faraday efficiency.

The post-experimental characterization section describes the analysis of the silicon deposits at the silicon cathode and tungsten cathode current collector using optical microscopy and SEM/EDS. The silicon deposits were found to be pure, while a dense layer of Tungsten Silicide (WSi_2) was observed at the interface between the tungsten current collector and the flux.

Lastly, the equivalent circuit modeling and curve fitting analysis were performed to identify the key polarization losses in the electrolysis process. Reducing polarization losses due to mass transfer at the cathode, charge transfer, and ohmic resistance are crucial for enhancing electrolysis efficiency.

5. SOM ELECTROLYSIS PROCESS FOR IRON RECYCLING

5.1 Fe-SOM Electrolysis Process with YSZ and Silver as the Reducing Medium

5.1.1 Experimental Setup

A proof-of-concept salt-free SOM cell for iron production is shown in **Figure 5.1**. The anode assembly of the Fe-SOM cell incorporates a silver pool as the anode, a one close-ended YSZ tube that conducts oxygen ions from the cathode to anode, low-carbon steel crucible that contains the silver pool, and Inconel 601 rod as the anode current collector. The Inconel rod was connected to the steel crucible with a set screw. It should be noted that to an alumina tube was used to extend the YSZ tube. The alumina tube was connected to the YSZ tube using a gas-sealant alumina paste.

A mixture of Fe_2O_3 , YSZ and silver (each 1/3rd in volume) functioned as the electrolyte of the Fe-SOM electrolysis cell. To create an efficient pathway for the oxygen in Fe_2O_3 to migrate through the electrolyte to the YSZ membrane, it is important to provide Fe_2O_3 with sufficient contact area with both silver and YSZ during the electrolysis. To achieve that, equal volumes of Fe_2O_3 , YSZ and silver powders were thoroughly mixed. The mixture was then pressed into a compact and loaded into the YSZ tube.

A low carbon steel rod was used as the cathode and current collector. A tiny layer of silver powder was placed above the compact to ensure good electrical contact between the steel cathode and the liquid silver anode during electrolysis. To maintain an initial oxygen-free environment in the SOM system for efficient electrolysis, 200 sccm argon

gas was passed through an oxygen trap filled with heated copper chips and flowed to both the anodic and the cathodic side.

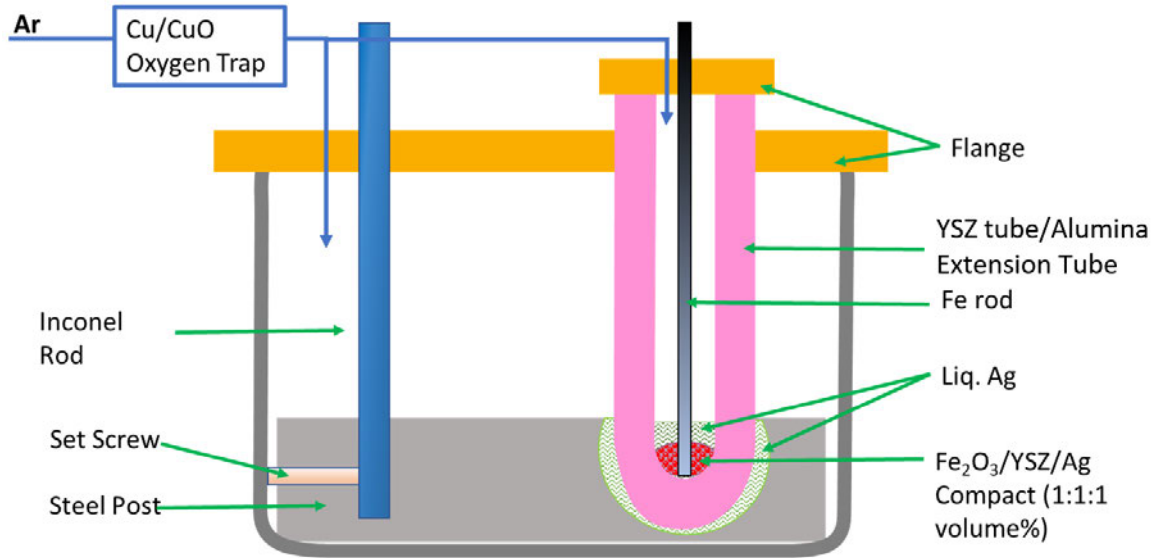


Figure 5.15. Experimental Setup of Salt-free SOM Process for Iron Production using Ag and YSZ as the reducing medium

5.1.2 Electrochemical Characterization

5.1.2.1 Current-Potential Characteristics

A Potentiodynamic Scan (PDS) was conducted between the anode current collector and the cathode, and the current-potential plot is shown in **Figure 5.2**. A significant amount of leakage current was observed, which is attributed to the impurity oxygen that is soluble in the liquid silver inside the YSZ tube. To reduce the leakage current, a pre-electrolysis at 0.8V was performed for 120 min to remove the soluble oxygen in the silver.

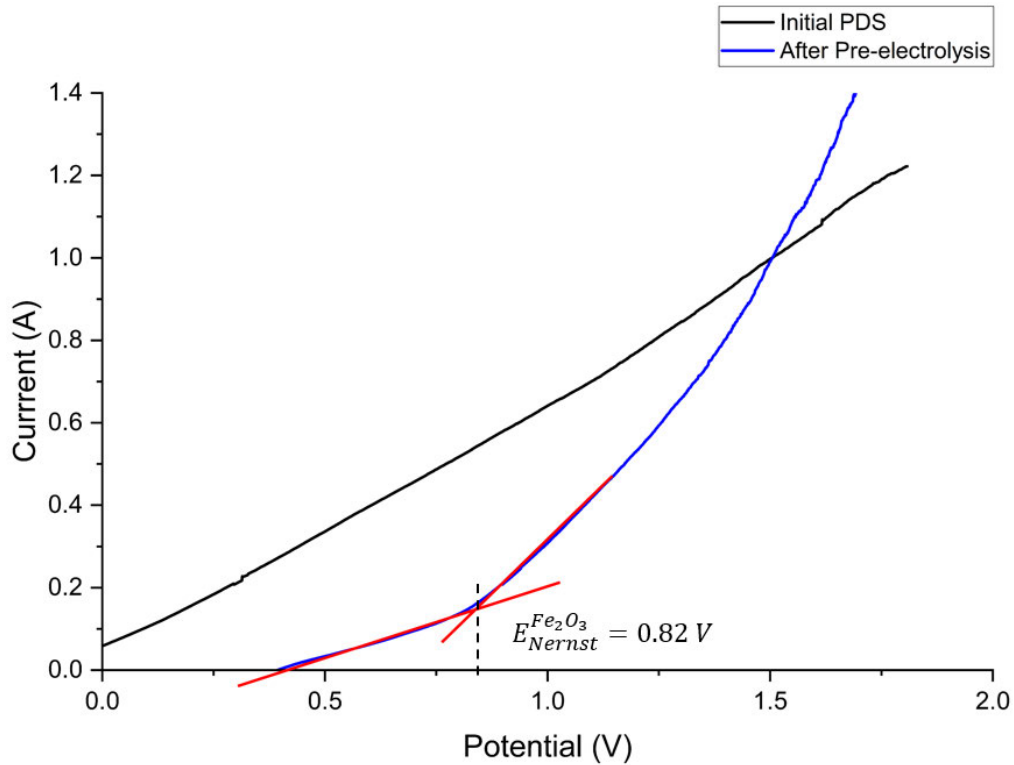


Figure 5.16. Current-Potential Relationship Before and After the Pre-electrolysis

After the pre-electrolysis, another PDS was conducted between the anode current collector and the cathode, and the current-potential plot is shown in **Figure 5.2**. The leakage current was significantly reduced after the pre-electrolysis. The total cell resistance was calculated to be 0.83 ohms. It was determined by calculating the reciprocal of the slope of the current-potential profile at potentials above the dissociation potential of Fe_2O_3 . Previous studies have shown that the charge transfer reaction at the liquid metal electrode surface is fast, so the activation polarization of this cell should be negligible [49-52]. In addition, mass-transfer limitation is negligible at small currents. As a result, the total cell resistance is primarily attributed to the ohmic resistance of the cell. Notably, the ionic resistance of the YSZ membrane was calculated to be 0.66 ohms. Therefore, the

total cell resistance is limited by the ionic resistance of the YSZ. The cell performance can be improved by reducing the thickness of the YSZ membrane and increasing the contact area between the silver anode and the YSZ membrane tube.

The Nernst potential for Fe_2O_3 dissociation $E_{Nernst}^{\text{Fe}_2\text{O}_3}$ was identified to be approximately 0.82 V, which is consistent with the standard Nernst potential for Fe_2O_3 dissociation ($E_{Nernst}^{\circ \text{Fe}_2\text{O}_3} = 0.81$ V). After pre-electrolysis most of the impurity oxygen was removed, and the system was ready for electrolysis.

5.1.2.2 Current-time Profile during the Electrolysis

Two electrolysis experiments were performed at 1373 K to dissociate Fe_2O_3 , both were held at 1.8 V, one for 2 hours and the other for 1.5 hours. The current time plots are shown in **Figure 5.3**. The total charge consumed in the process was 12411 C, whereas only 2372 C would be required for the complete reduction of Fe_2O_3 assuming 100% current efficiency. A significant current flow was observed at the conclusion of the second electrolysis, indicating the presence of another charged species undergoing mass transport through the electrolyte and YSZ membrane.

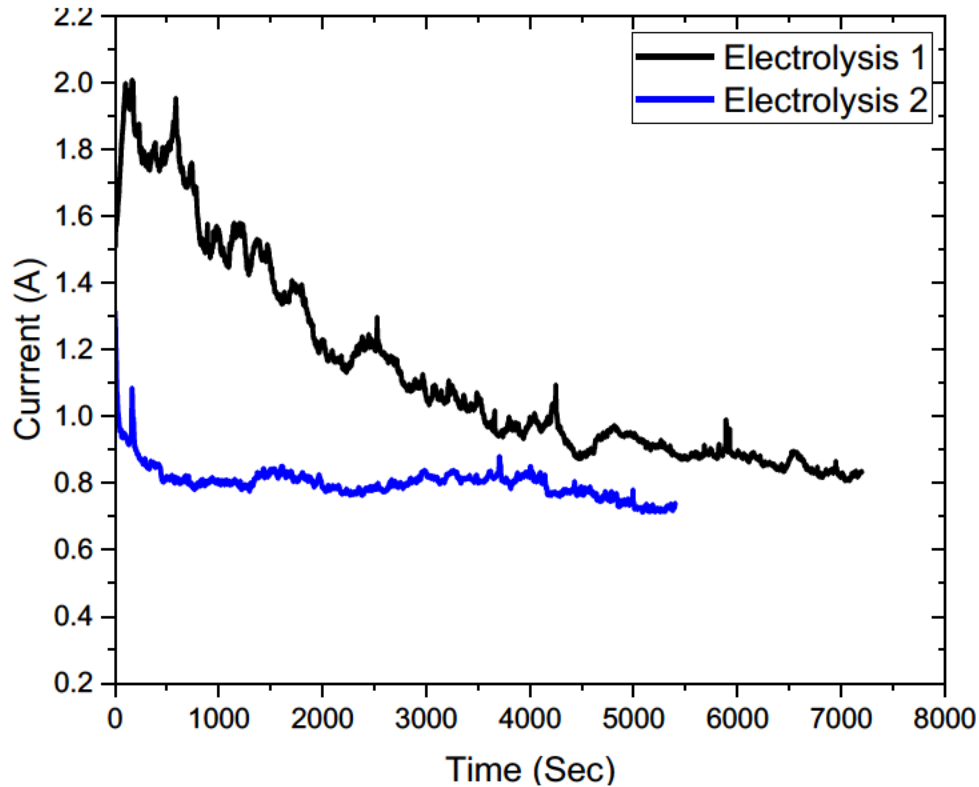


Figure 5.17. Current-Time Profile during Electrolysis 1 and Electrolysis 2 with an applied potential of 1.75 V for 2 hrs and 1.5 hrs respectively

One possible explanation for the remaining current flow is the introduction of oxygen into the cathode site during the electrolysis. Despite the removal of most impurity oxygen in the silver during the pre-electrolysis stage, the oxygen produced during the electrolysis may have been able to return to the cathode site due to imperfect sealing at the joint of YSZ membrane/alumina extension tube. The sealing at the joint between the YSZ tube and alumina extension tube was initially confirmed to be leak-tight before the electrolysis. However, it is possible that the sealing may have been compromised during the heating process. The leak within the sealing results in a continual influx of oxygen into the cathode site. As a result, soluble atomic oxygen was formed in the silver while the system attempted to pump out the oxygen through the electrolysis.

The compromised sealing at the joint between the YSZ tube and alumina extension tube likely resulted from the non-alignment of the YSZ tube entering the anode silver pool. To mitigate this, the top flange for loading the YSZ tube needed to be re-machined to ensure that the YSZ tube and Inconel current collector are parallel in position without any tilting.

Another possible explanation for the remaining current is the increasing electronic conductivity of YSZ. When most of iron oxide was reduced, the oxygen partial pressure at the cathode site is significantly low. This leads to an increase in electronic conductivity of YSZ. The cell is partially short-circuited by electronic conduction through the YSZ membrane. A detailed analysis on the electronic conductivity of YSZ as a function of oxygen partial pressure will be presented in Section 5.3.2.2.

5.1.3 Post-experimental Characterization

After the electrolysis, the furnace was cooled, and the setup was disassembled. The bulk of the compact was sectioned, mounted in epoxy, and characterized under SEM/EDS. **Figure 5.4** shows the SEM image and corresponding EDS mapping of the reduced iron within the bulk of the compact. Further EDS spot analysis shows that the purity of iron deposits within the bulk of the compact is over 98 atomic%. (**Figure 5.5**).

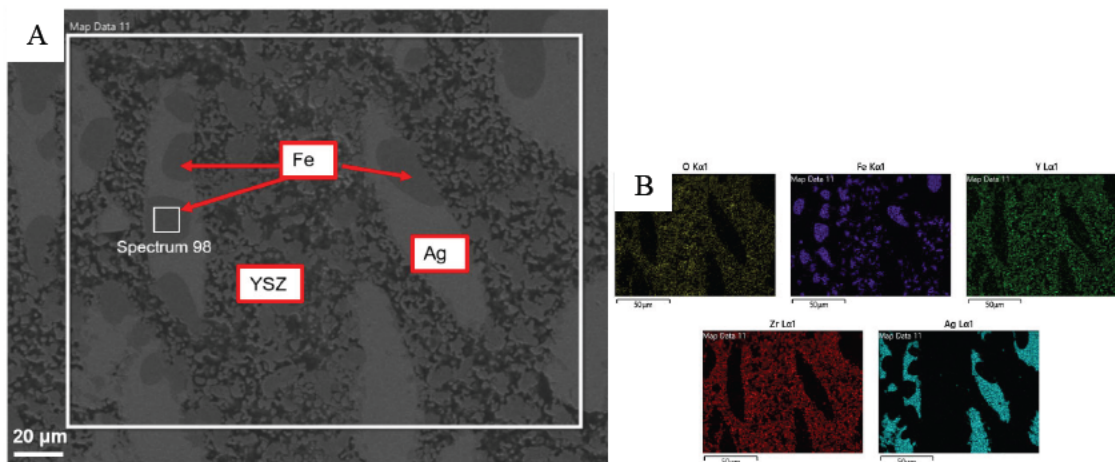


Figure 5.18.A). SEM images of the post-experiment compact(bulk). **B).** EDS mapping of the corresponding area.

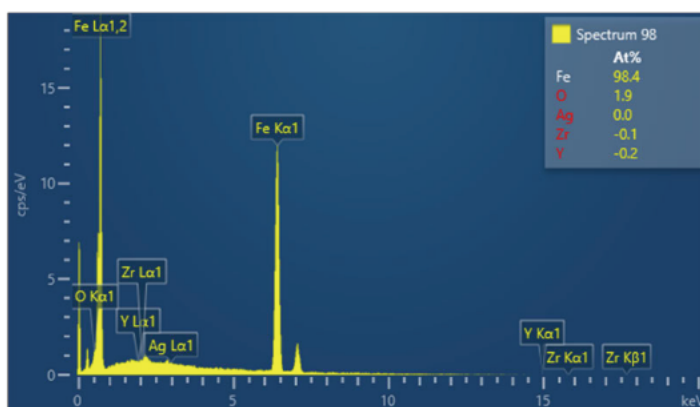


Figure 19.5. EDS point analysis on Spectrum 98 showing the purity of iron deposits

Similarly, the cathode/compact interface was characterized under SEM/EDS.

Figure 5.6 shows the SEM image and corresponding EDS mapping of the reduced Iron within the bulk of the compact. Further EDS spot analysis shows that the purity of reduced iron near the cathode and iron cathode is approximately 84 atomic%, with oxygen present as the primary impurity (**Figure 5.7**). This confirms the prediction that oxygen returned to the cathode site during the electrolysis, leading to low current efficiency.

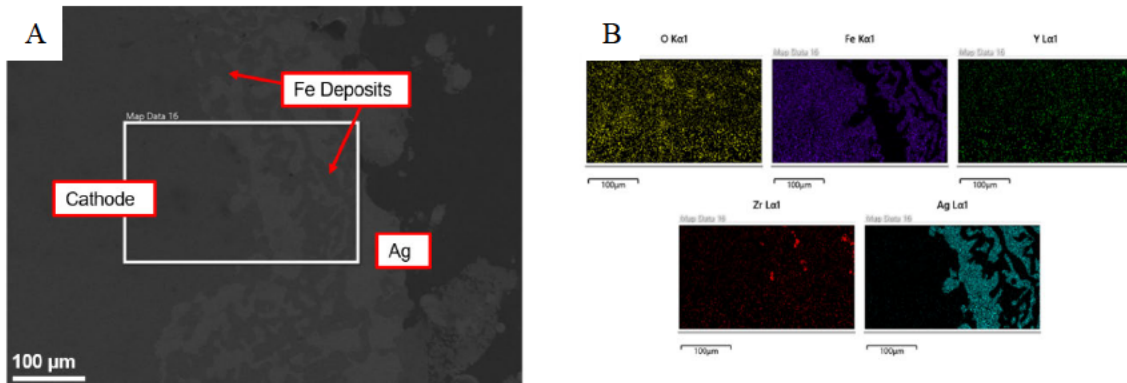


Figure 5.20. A). SEM images of the post-experiment cathode/compact interface. B). EDS mapping of the corresponding area.

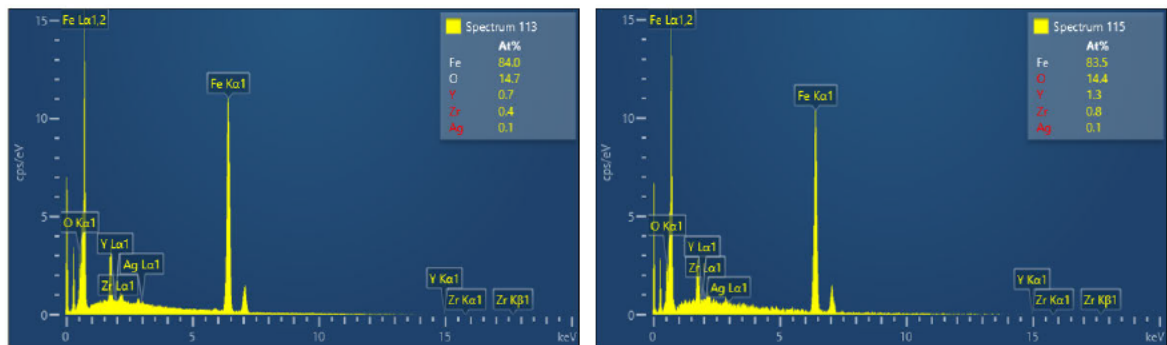


Figure 5.21. EDS point analysis of: A). the iron deposits at the cathode/compact interface. B). the iron cathode.

To confirm the phase composition of the Fe deposits and identify the phase transformation, X-ray Diffraction (XRD) analysis was performed on the compact before and after the electrolysis. The compact was crushed into powders and characterized under Bruker D2 Phaser XRD Analyzer. **Figure 5.8** shows the XRD measurements of the compact before and after the electrolysis. It is evident that most Iron Oxide was reduced to Iron, and no secondary phases were observed.

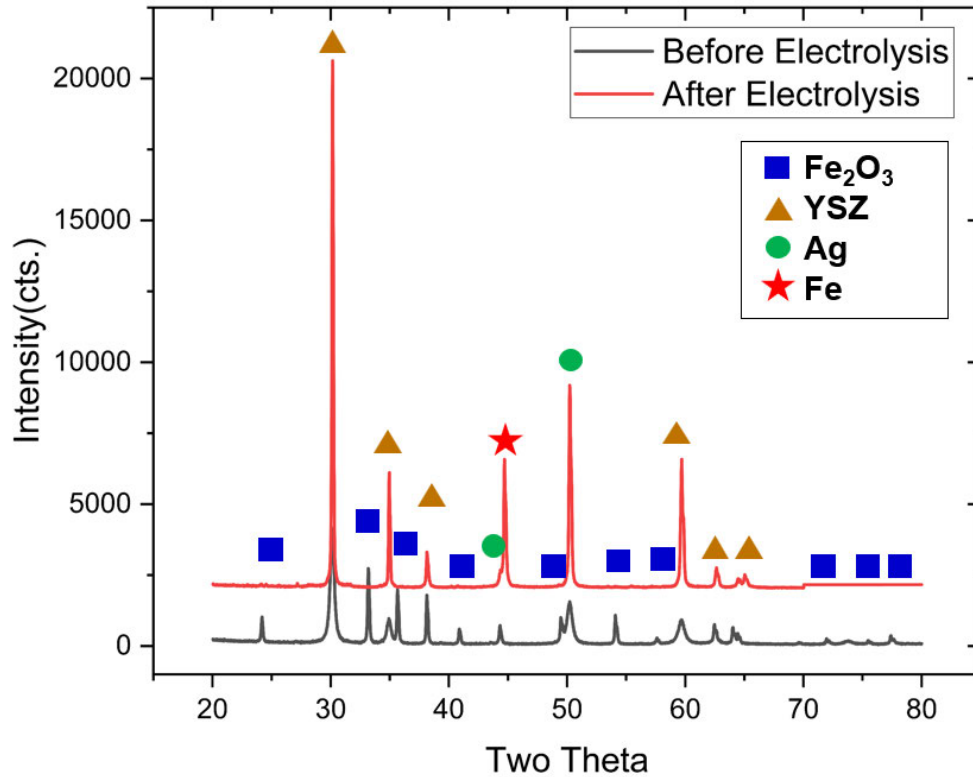


Figure 5.22. XRD spectrum of the compact before and after electrolysis.

5.2 Fe-SOM Electrolysis Process with Silver as the Reducing Medium

5.3.1 Experimental Setup

To understand the role of YSZ in oxygen transport through the electrolyte, another Fe-SOM electrolysis was performed when the compact contained only Ag and Fe₂O₃ (**Figure 5.9**). Equal volumes of Fe₂O₃, silver powders were thoroughly mixed, pressed into a compact and loaded into the YSZ tube prior to the electrolysis. A new flange was used and carefully machined to center the alignment of the YSZ tube into the anode silver pool. All other cell components remained the same as the Fe-SOM cell with YSZ and silver as the reducing medium.

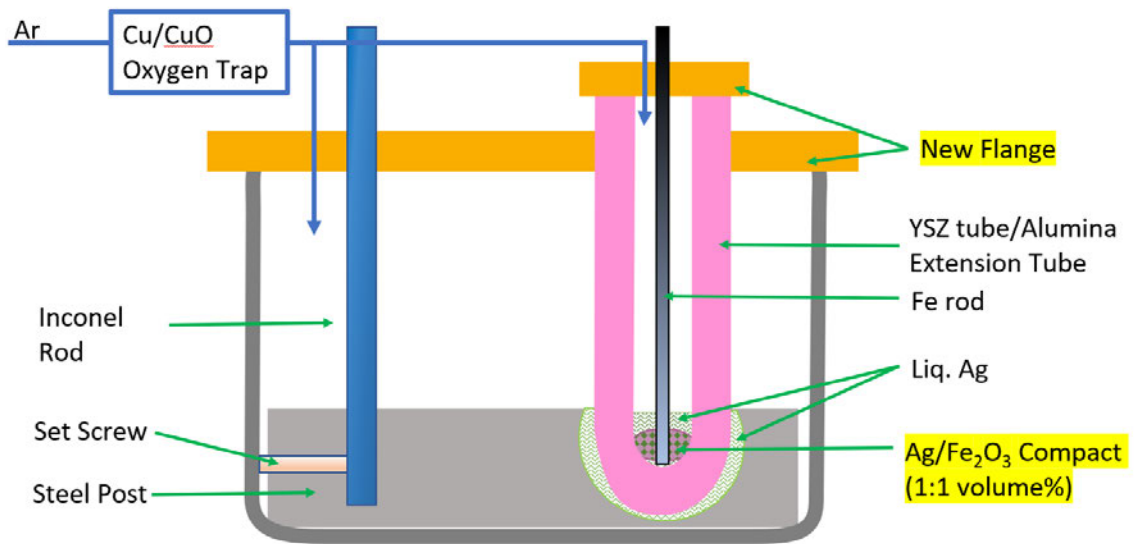


Figure 5.23. Experimental Setup of Molten Salt-free SOM process for iron production using Ag as the reducing medium

5.2.2 Electrochemical Characterization

5.2.2.1 Current-Potential Characteristics

A PDS was conducted between the anode current collector and the cathode, and the current-potential plot (labelled as YSZ-free) is shown in **Figure 10**. Negligible leakage current was observed, and the Nernst potential for Fe₂O₃ dissociation $E_{Nernst}^{Fe_2O_3}$ was identified to be approximately 0.78 V. The current-potential plot for the experiment with YSZ and Ag as the reducing medium was also plotted in **Figure 10** and labeled as "YSZ-contained."

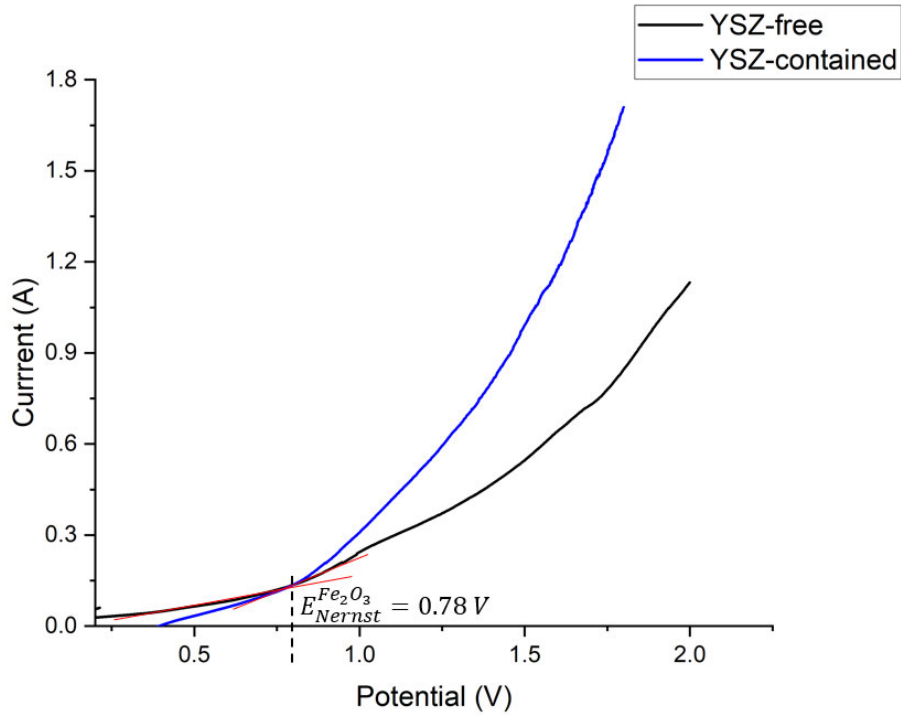


Figure 5.24. PDS showing the current-potential relationship in Fe-SOM experiments with and without YSZ in the compact

When the applied potentials exceeded the Nernst potential for Fe_2O_3 dissociation, more current was observed in the experiment that used YSZ and Ag as the reducing medium than the experiment that used only Ag as the reducing medium. As the amount of Fe_2O_3 initially present in the compact was identical in both experiments, the dissociation of Fe_2O_3 appears to be more kinetically favored in the former experiment.

The dissociation of Fe_2O_3 can still occur when the electrolyte contains only Ag as the reducing medium. In this case, the oxygen transport within the silver was enabled by the diffusion of atomic oxygen in the liquid silver. The solubility of oxygen in liquid silver is around 2000 ppm at 1100 C and the diffusivity of atomic oxygen in the liquid silver at 1100 C is reported to be in a range of $1.2 - 2.0 \times 10^{-4} \text{ cm}^2/\text{s}$ [28][53]. Therefore, the relatively high value of oxygen solubility and diffusivity in silver explains the

feasibility of oxygen transport through the liquid silver.

When YSZ particles were added into the electrolyte, they were interconnected by thorough mixing and pressing. The interconnected YSZ particles within the electrolyte provides an alternative pathway for oxygen migration. The rate of oxygen transport through this pathway depends on the oxygen ion diffusivity in YSZ. Guan et al. reported that the oxygen ion diffusivity in 8 mol% Ytria-stabilized Zirconia (8YSZ) at 1400 K is $0.12 \times 10^{-4} \text{ cm}^2/\text{s}$ [54]. This value explains the efficient ionic conduction of oxygen through YSZ.

Therefore, with an additional oxygen transport pathway enabled by the ionic conduction through the interconnected YSZ particles within the electrolyte, the mass transport of oxygen is promoted. As a result, the overall cell resistance is effectively reduced.

5.2.2.2 Current-time Profile during the Electrolysis

An electrolysis was performed to dissociate Fe_2O_3 , held at 1.8 V for 6 hrs. The current-time plot during the electrolysis is shown in Figure **5.11**, labelled as “ $\text{Fe}_2\text{O}_3 + \text{Ag}$ ”.

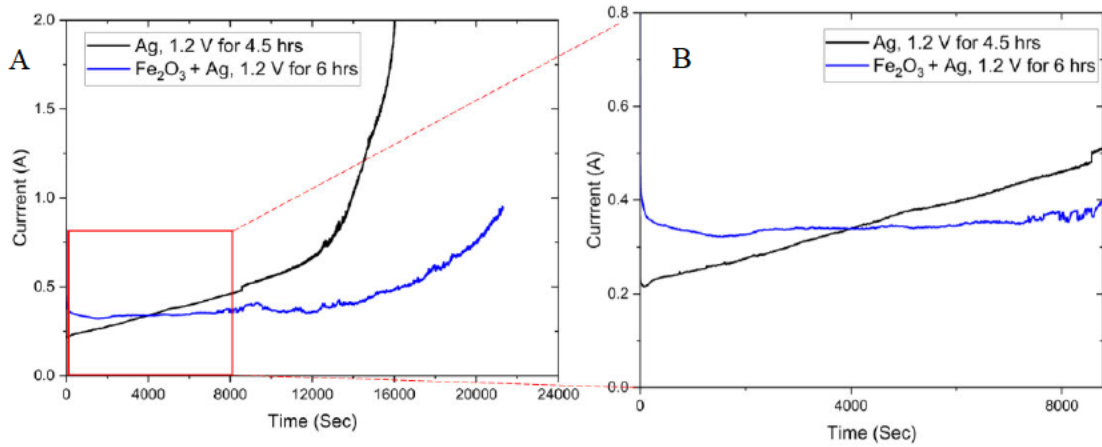


Figure 5.25. Current-Time Profile in the time span of A) 0 to 21600 seconds. B). 0 to 7800 seconds.

It was observed that the current remained stable for the initial 7800 seconds, with an estimated total charge of 2661 C passing through the system. This value closely aligns with the theoretical charge required for complete dissociation of iron oxide (2372 C). After that, the current exhibited some fluctuations and gradually increased at an accelerated rate. This increase is likely associated with the increasing electronic conductivity of YSZ. The electronic conductivity of 8YSZ can be expressed as a function of oxygen partial pressure and temperature [55]:

$$\sigma_{e(8SZ)} = 1.31 \times 10^7 \exp\left(\frac{-3.88\text{eV}}{k_B T}\right) P_{O_2, YSZ/cathode}^{-1/4}$$

Eq 5-1

where k_B is the Boltzmann constant (8.617×10^{-5} eV/K), $P_{O_2, YSZ/cathode}$ is the oxygen partial pressure at the cathode/YSZ interface. When Fe_2O_3 is present at the cathode site, the oxygen partial pressure $P_{O_2, YSZ/cathode}$ is established by the activity of Fe and Fe_2O_3 and determined to be 1.49×10^{-12} atm. $\sigma_{e(8SZ)}$ at this oxygen partial pressure and electrolysis temperature of 1100 C was calculated to be 6.7×10^{-5} S/cm. Therefore, the electronic conduction through YSZ membrane is negligible when Fe_2O_3 is present at the

cathode site. As the majority of Fe_2O_3 is consumed, the oxygen partial pressure at the cathode site decreases while the applied potential is held constant near 1.8 V. This results in an increase in the electronic conductivity of YSZ ($\sigma_{e(8\text{SZ})}$), and the cell is partly short-circuited by electronic conduction through the YSZ membrane. The relationship between $P_{\text{O}_2, \text{YSZ}/\text{cathode}}$ and $\sigma_{e(8\text{SZ})}$, is plotted in Figure 5.12. It is observed that the rate of current increase measured in the experiment follows similar trend as the rate of increase of $\sigma_{e(8\text{SZ})}$ with decrease in the $P_{\text{O}_2, \text{YSZ}/\text{cathode}}$.

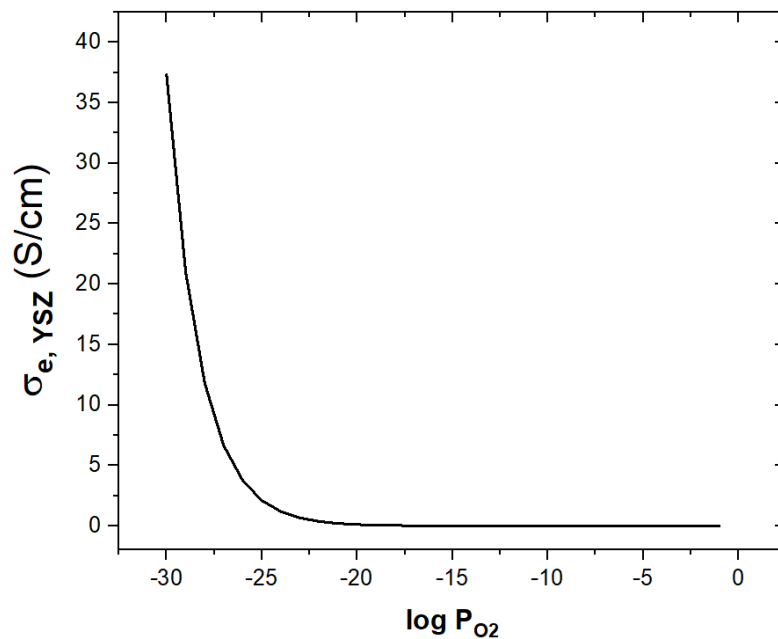


Figure 5.26. Electronic conductivity of 8YSZ ($\sigma_{e(8\text{SZ})}$) as a function of the oxygen partial pressure ($P_{\text{O}_2, \text{YSZ}/\text{cathode}}$)

Another experiment was conducted to validate the factors that attributes to the increasing current observed in Figure 5.11. The compact that contained only Ag was placed within the YSZ membrane, and a potentiostatic hold was applied across the

cathode and anode current collectors at 1.2 V for 4.5 hours. The current-time relationship is shown in **Figure 5.11**, labelled as “Ag-only”. It is evident that in the absence of Fe_2O_3 , the current increased immediately the potential hold. The rate of increase closely matches the observed current increase after 7800 seconds of the electrolysis experiment, as well as the relationship between $\sigma_{e(\text{8SZ})}$ and $P_{\text{O}_2, \text{YSZ}/\text{cathode}}$.

Overall, the cell efficiency for the first 7800 seconds was high as there was negligible electronic current passing through the YSZ membrane. However, once most of the iron oxide was reduced, the cell was short-circuited due to electronic conduction in the YSZ membrane. As a result, it is necessary to stop the electrolysis experiment immediately after most of the iron oxide is reduced.

5.2.3 Post-experimental Characterization

After the electrolysis, the furnace was cooled, and the setup was disassembled. The bulk of the compact and the cathode/compact interface were sectioned, mounted in epoxy, and characterized with SEM and EDS (**Figure 5.13** and **5.14**). EDS spot analysis of the iron deposits at both regions shows the purity of Fe was >99.5 atomic % with less than 0.5 atomic % O impurity. (**Figure 5.15**). The iron deposits wetted the Ag, making it challenging to separate them directly using a magnet.

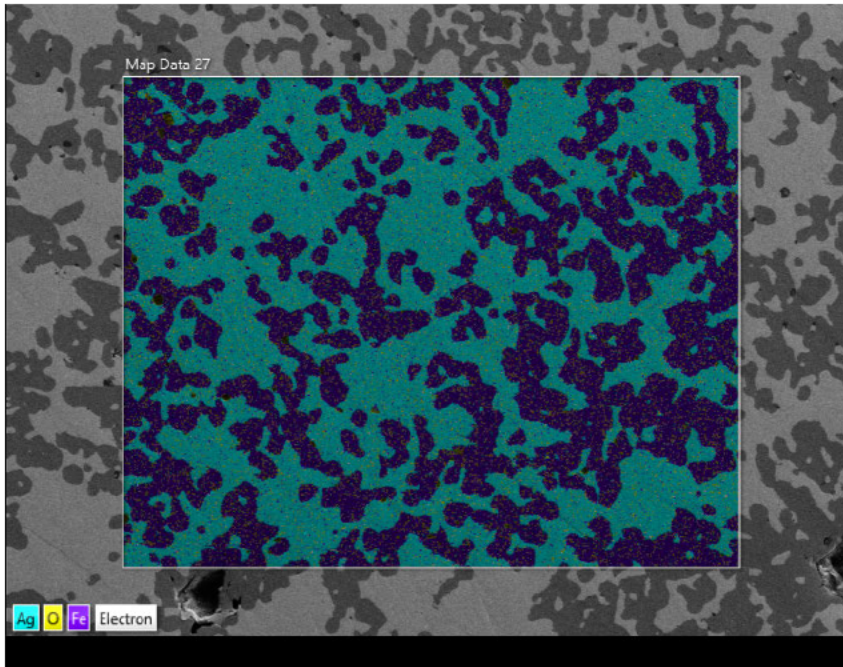


Figure 5.27. EDS Mapping of the Post-electrolysis Compact (Bulk).

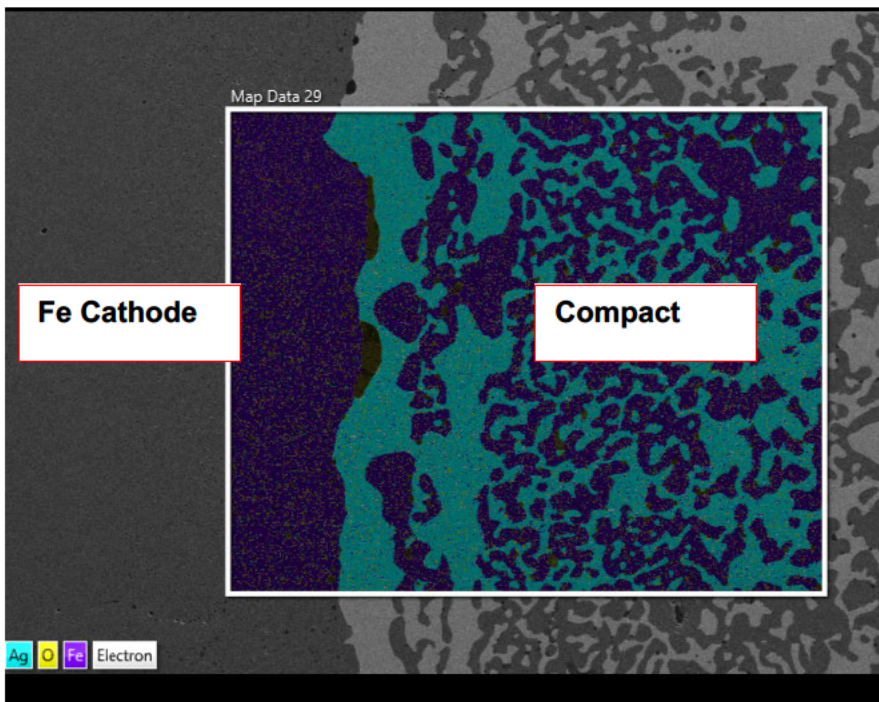


Figure 5.28. EDS Mapping of the Post-electrolysis Cathode/Compact Interface.

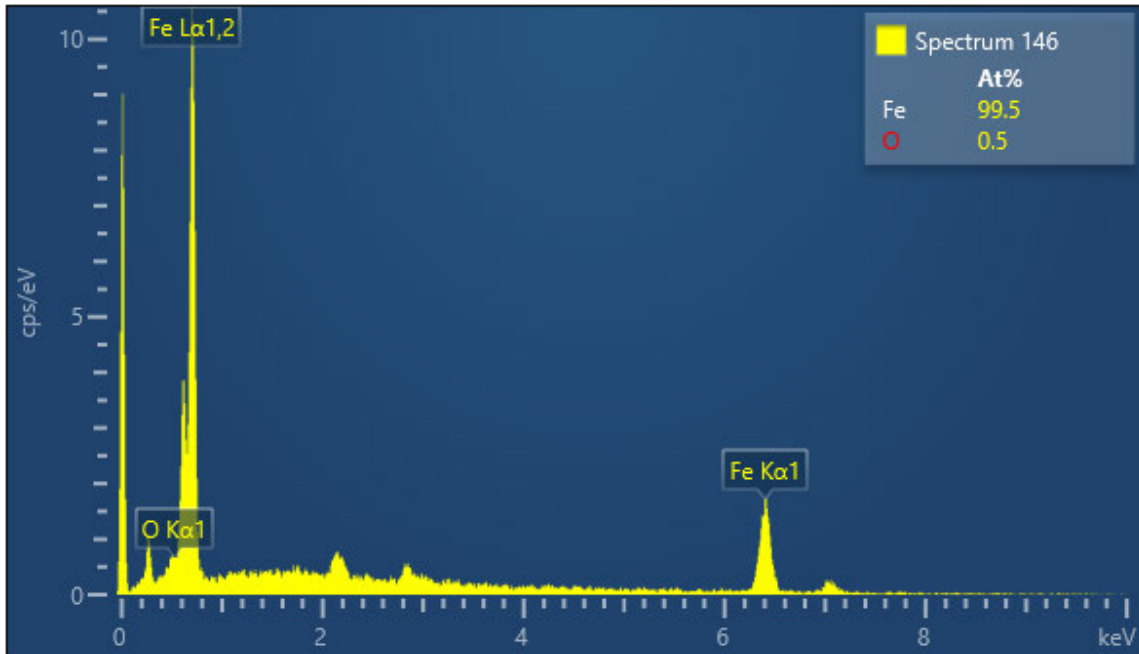


Figure 5.29. EDS Spot Analysis of the Iron Deposits

5.3 Summary

Chapter 5 demonstrates the feasibility of depositing high purity Iron via a novel, molten-salt free SOM electrolysis. Two SOM experimental setups are explored, and the respective electrochemical and post-experimental characterization are presented.

The first Fe-SOM experimental setup involved the use of YSZ and Ag as the reducing medium. The leakage current was observed in the initial PDS scan, resulting from the soluble oxygen in the silver that was later removed through a pre-electrolysis at a lower applied potential. The PDS scan after the pre-electrolysis suggests that the cell resistance was low, and it was primarily attributed to the ionic resistance of the YSZ membrane. The current-time profile indicates that the cell operates at a low efficiency, which can be attributed to the introduction of freshly produced oxygen back into the cathode site. This can be mitigated by improving the sealing of the cathode assembly.

The purity of iron deposits was found to be 98 at% within the bulk of the compact and 85% at the cathode/compact interface, with O present as the major impurities.

The second Fe-SOM experimental setup involved only Ag as the reducing medium. The current-potential profile of this experiment suggests that the addition of YSZ within the compact in the earlier experiment enhanced oxygen transport. The current-time profile indicates that the cell initially operated at a high efficiency. However, once most of the iron oxide was reduced, the electronic conduction through the YSZ membrane became significant, causing a short-circuit in the cell. Therefore, it is recommended that the electrolysis should be immediately stopped after the majority of the iron oxide has been reduced. The purity of the iron deposits was found to be 99.5 atomic% and the iron deposits were found to be wetted by the Ag, making it difficult to separate them directly using a magnet.

6. Conclusion and Future Work

6.1 Conclusion

This work has demonstrated the feasibility of utilizing Solid Oxide Membrane (SOM) electrolysis for the production of high-purity silicon and iron. The SOM electrolysis process involves the use of a solid oxide membrane to selectively transport oxygen ions, facilitating metal deposition at the cathode while allowing efficient separation of oxygen from the electrolyte.

Optimization of SOM process for Silicon deposition was explored. Three key aspects were addressed: Si wafer thinning, elimination of carbon (C) and zirconium (Zr) impurities and preventing the Si-Mg-O phase formation. Thorough Si stability experiments were conducted to understand the thinning mechanism. The required Si wafer immersion depth below the salt surface to prevent Si wafer thinning was determined to be 4 cm. The investigation on the incorporation of impurities showed that the C impurities originated from the graphite cathode current collector. This issue was resolved by replacing graphite with a Tungsten collector. Furthermore, the presence of Zr impurities was attributed to the interplay between YSZ, SiO₂ and C. To eliminate the Zr impurities, a carbon-free environment was required, which was established by employing a Boron Nitride crucible. The investigation of the formation of the Si-Mg-O phase at the cathode/flux interface showed that the presence of MgO in the flux leads to the formation of the Si-Mg-O phase. By reducing CaO and SiO₂ content in the flux, the formation of MgO and the Si-Mg-O phase were eliminated. The suggested optimal flux composition is eutectic CaF₂-MgF₂ with 4 wt% YF₃, 2.5 wt% SiO₂, and 4 wt% CaO.

The modifications made to the Si-SOM setup effectively addressed the challenges identified in Chapter 3, enhancing the efficiency and reliability of the electrolysis process. The electronic transference number remained low and did not change during electrolysis, indicating that the SOM flux was primarily ionic. The current-potential profile and electrochemical impedance spectroscopy (EIS) measurements taken at different stages of the electrolysis process suggest that total and ohmic resistance within the cell were low throughout the entire electrolysis process. Current-time profile and associated Faraday efficiency indicate a stable electrolysis process with high Faraday efficiency. The post-experimental characterization confirmed the high purity of the silicon deposits while identifying the presence of Tungsten Silicide (WSi_2) at the cathode/flux interface. Furthermore, the equivalent circuit modeling and curve fitting analysis provided valuable insights into polarization losses, emphasizing the importance of reducing mass transfer, charge transfer, and ohmic resistance to enhance electrolysis efficiency.

Lastly, a novel, molten-salt free SOM electrolysis process for high-purity iron production was demonstrated. Two experimental setups were explored, one utilizing YSZ and Ag as reducing media, and the other employed only Ag. It is found that the addition of YSZ enhanced the oxygen transport by providing an alternative additional pathway. The sealing of the cathode assembly was found to be crucial for improving the cell efficiency. Furthermore, the observation of electronic conduction through the YSZ membrane emphasized the need for stopping electrolysis once the iron oxide is reduced. The purity of the iron deposits was found to be 99.5 at%.

6.2 Future Work

Future work for Si-SOM process should include the incorporation of inert anode current collector. Previous studies have successfully demonstrated the feasibility of an inert anode assembly for production of magnesium and aluminum. This assembly utilizes sintered strontium-doped lanthanum manganite (LSM) bars and an Inconel rod as the inert anode current collector. With the implementation of an inert anode current collector, the SOM process achieves a remarkable milestone of zero-direct carbon emissions, making it an environmentally friendly and sustainable method for metal production. Moreover, the utilization of an inert anode current collector in the SOM process offers the significant advantage of generating pure oxygen as a valuable by-product. This additional feature further enhances the appeal of the SOM electrolysis for industrial applications, particularly in sectors that rely on a stable and continuous supply of oxygen.

Another area of future research lies in the development of inert anode materials that enable long-term operation of SOM process. While the current anode material, Ag, has proven effective in the electrolysis, it vaporizes over time at high temperatures. Addressing this issue and finding alternative, more stable inert anode materials is crucial to enhance the overall efficiency and reliability of the SOM electrolysis.

The equivalent modeling and curve fitting analysis indicate that optimizing the molten flux composition, operating parameters, and experimental setup can effectively reduce polarization losses and enhance performance. One approach is to explore alternate cathode materials or improving the surface treatment of the current silicon cathode to

enhance the electrocatalytic activity of the cathode surface and improve adhesion between silicon deposits and the cathode.

Future work on the SOM process for iron production should focus on developing effective methods to separate the iron deposits from the reducing medium. By quantifying the iron produced, the cathodic cell efficiency of the electrolysis process can be assessed. Furthermore, when the iron can be effectively collected, it will complete the full oxidation/reduction cycle for use of iron as an energy carrier. This achievement will enhance its potential as a promising option for use as an electrofuel, offering a more sustainable and efficient energy storage solution.

Lastly, a comprehensive electrochemical modeling and curve fitting analysis are essential for the Fe-SOM process to gain deeper insights into the various contributions of the polarization losses and optimize the electrolysis performance. This in-depth analysis will not only enhance our understanding of the Fe-SOM process but also facilitate the design of more efficient and economically viable electrolysis systems for iron recovery from iron oxide.

BIBLIOGRAPHY

- [1] M. S. Islam, M. A. Rhamdhani, and G. A. Brooks, "Solar-grade silicon: current and alternative production routes," In: *Chemeca 2011: Engineering a Better World*. Barton, A.C.T.: Engineers Australia, 2011: pp. 1826 1839.
- [2] D. Rechenberger, "Gross efficiency of power stations in Germany Energy mix for average electricity production (net) in Germany Gross efficiency of power stations in Germany."
https://www.wingas.com/fileadmin/Wingas/WINGASStudien/Energieversorgung_und_Energiewende_en.pdf.
- [3] J. Nelson, A. Gambhir, and N. Ekins-Daukes, "Solar power for CO₂ mitigation," *Grantham Institute for Climate Change, Briefing Paper No. 11*. Imperial College, London, 2014. <https://www.imperial.ac.uk/media/imperial-college/grantham-institute/public/publications/briefing-papers/Solar-power-for-CO2-mitigation---Grantham-BP-11.pdf>
- [4] "Renewables 2017," *International Energy Agency*,
<https://www.iea.org/publications/renewables2017/>. (accessed Jan 05, 2022)
- [5] "Polysilicon Production Processes." *Polysilicon Production: Siemens Process | Bernreuter Research*, <https://www.bernreuter.com/polysilicon/production-processes/>.
- [6] A. Goodrich et al., "A wafer-based monocrystalline silicon photovoltaics road map: Utilizing known technology improvement opportunities for further reductions in manufacturing costs," *Solar Energy Materials and Solar Cells*, vol. 114, pp. 110 135, 2013.
- [7] J. M. Bergthorson, "Recyclable metal fuels for clean and compact zero-carbon power," *Progress in Energy and Combustion Science*, vol. 68, pp. 169 196, 2018. doi:10.1016/j.pecs.2018.05.001
- [8] P. Debiagi, R. C. Rocha, A. Scholtissek, J. Janicka, and C. Hasse, "Iron as a sustainable chemical carrier of renewable energy: Analysis of opportunities and challenges for retrofitting coal-fired power plants," *Renewable and Sustainable Energy Reviews*, vol. 165, p. 112579, 2022. doi:10.1016/j.rser.2022.112579
- [9] Environmental and Energy Study Institute (EESI), "Green hydrogen," EESI, <https://www.eesi.org/briefings/view/042722tech> (accessed Jul. 24, 2023).
- [10] A. Krishnan, X. G. Lu and U. B. Pal, "Solid oxide membrane (SOM) technology for environmentally sound production of tantalum metal and alloys from their oxide sources," *Scandinavian Journal of Metallurgy*, vol. 34, no. 5, pp. 293-301, 2005.

- [11] X. Guan, U. B. Pal, S. Gopalan and A. C. Powell, "LSM ($\text{La}_{0.8}\text{Sr}_{0.2}\text{MnO}_3$)-Inconel inert anode current collector for solid oxide membrane (SOM) electrolysis," *Journal of The Electrochemical Society*, vol. 160, no. 11, pp. F1179-F1186, 2013.
- [12] X. Guan, U. B. Pal and A. C. Powell, "Energy-Efficient and Environmentally Friendly Solid Oxide Membrane Electrolysis Process for Magnesium Oxide Reduction: Experiment and Modeling," *Metallurgical and Materials Transactions E*, vol. 1, no. 2, pp. 132-144, 2014.
- [13] E. S. Gratz, X. Guan, J. D. Milshtein, U. B. Pal and A. C. Powell, "Mitigating Electronic Current in Molten Flux for the Magnesium SOM Process," *Metallurgical and Materials Transactions B*, vol. 45, no. 4, pp. 1325-1336, 2014.
- [14] X. Guan, S. Su, U. B. Pal and A. C. Powell, "Periodic Shorting of SOM Cell to Remove Soluble Magnesium in Molten Flux and Improve Faradaic Efficiency," *Metallurgical and Materials Transactions B*, vol. 45, no. 6, pp. 2138-2144, 2014.
- [15] S. Su, X. Guan and U. Pal, "Zero-carbon-emission Aluminum Production by Solid Oxide Membrane Based Electrolysis Process," in 2015 TMS Annual Meeting & Exhibition, Orlando, Florida, 2015.
- [16] M. Suput, R. DeLucas, S. Pati, G. Ye, U. Pal and A. Powell, "Solid Oxide Membrane Technology for Environmentally Sound Protection of Titanium," *Mineral Processing and Extractive Metallurgy: Transactions of the Institutions of Mining and Metallurgy: Section C*, vol. 117, no. 2, pp. 118-122, 2008.
- [17] S. Pati, M. Suput, R. Delucas and U. B. Pal, "Solid Oxide Membrane Process for Calcium Production Directly from Its Oxide," in EPD Congress, TMS, Warrendale, PA, 2008.
https://www.researchgate.net/publication/287248627_Solid_oxide_membrane_process_for_calcium_production_directly_from_its_oxide
- [18] A. Martin, D. Lambertin, J.-C. Pognet, M. Allibert, G. Bourges, L. Pescayre and J. Fouletier, "The Electrochemical Deoxidation of Metal Oxides by Calcium Using a Solid Oxide Membrane," *JOM: The Journal of The Minerals, Metals & Materials Society*, vol. 55, no. 10, pp. 52-54, 2003.
- [19] U. B. Pal and A. C. Powell IV, "The Use of Solid-Oxide-Membrane Technology for Electrometallurgy," *JOM: The Journal of The Minerals, Metals & Materials Society*, vol. 59, no. 5, pp. 44-49, 2007.
- [20] U. Pal and S.C. Britten, "Method and apparatus for metal extraction and sensor device related thereto", U.S. Patent 5,976,345, 2 Nov. 1999.

- [21] L. He, X.-g. Lu, C.-y. Chen, Q. Li, C.-h. Li and Q.-d. Zhong, "Metal niobium by solid oxygen-ion membrane," *The Chinese Journal of Nonferrous Metals*, vol. 18, no. 7, pp. 1336-1341, 2008.
- [22] Y. Jiang, P. A. Zink and U. B. Pal, "Solid Oxide Membrane Process for the Reduction of Uranium Oxide Surrogate in Spent Nuclear Fuel," *ECS Transactions*, vol. 41, no. 33, pp. 171-180, 2012.
- [23] B. Zhao, X. Lu, Q. Zhong, C. Li and S. Chen, "Direct electrochemical preparation of CeNi₅ and La_xCe_{1-x}Ni₅ alloys from mixed oxides by SOM process," *Electrochimica Acta*, vol. 55, pp. 2996-3001, 2010.
- [24] X. S. Ye, X. G. Lu, C. H. Li, W. Z. Ding, X. L. Zou, Y. H. Gao and Q. D. Zhong, "Preparation of Ti-Fe based hydrogen storage alloy by SOM method," *International Journal of Hydrogen Energy*, vol. 36, pp. 4573-4579, 2011.
- [25] X. Lu, X. Zou, C. Li, Q. Zhong, W. Ding and Z. Zhou, "Green Electrochemical Process Solid-Oxide Oxygen-Ion-Conducting Membrane (SOM): Direct Extraction of Ti-Fe Alloys from Natural Ilmenite," *Metallurgical and Materials Transactions B*, vol. 43B, pp. 503-512, 2012.
- [26] X. Zou, X. Lu, Z. Zhou and C. Li, "Direct electrosynthesis of Ti₅Si₃/TiC composites from their oxides/C precursors in molten calcium chloride," *Electrochemistry Communications*, vol. 21, pp. 9-13, 2012.
- [27] X. Zou, X. Lu, C. Li and Z. Zhou, "A direct electrochemical route from oxides to Ti Si intermetallics," *Electrochimica Acta*, vol. 55, pp. 5173-5179, 2010
- [28] J. K. Baird, T. R. King, and C. Stein, "Diffusion of oxygen in silver," *Journal of Physics and Chemistry of Solids*, vol. 60, no. 7, pp. 891-894, 1999. doi:10.1016/s0022-3697(99)00019-0
- [29] X. Guan, U. B. Pal, Y. Jiang, and S. Su, "Clean Metals Production by Solid Oxide Membrane Electrolysis Process." *Journal of Sustainable Metallurgy*, vol. 2, pp. 152-166, 2016. <https://doi.org/10.1007/s40831-016-0044-x>
- [30] S. Su, "Zero-Direct-Carbon-Emission Aluminum Production by Solid Oxide Membrane-Based Electrolysis Process," Doctoral dissertation, Boston University, 2016. <https://hdl.handle.net/2144/17080>
- [31] T. Villalon Jr., "Zero-direct emission silicon production via solid oxide membrane electrolysis." Doctoral dissertation, Boston University, 2018. <https://hdl.handle.net/2144/30729>

- [32] N. Sano, S. Honma, and Y. Matsushita, "Electrochemical measurement of oxygen diffusivity in Liquid Silver," *Metallurgical Transactions*, vol. 1, no. 1, pp. 301–303, 1970. doi:10.1007/bf02819278
- [33] J. Xu, B. Lo, Y. Jiang, U. Pal, and S. Basu, "Stability of yttria stabilized zirconia in molten oxy-fluorite flux for the production of silicon with the solid oxide membrane process," *Journal of the European Ceramic Society*, vol. 34, no. 15, pp. 3887–3896, 2014.
- [34] J. Guo, T. Villalon, U. B. Pal, S. N. Basu, "Effect of Optical Basicity on the Stability of Yttria-Stabilized Zirconia in Contact with Molten Oxy-Fluoride Flux." *Journal of the American Ceramic Society*, 2018, doi:10.1111/jace.15496,
- [35] F. D. Richardson, *Physical Chemistry of Melts in Metallurgy (Volume 2)*. London; New York: Academic Press, 1974.
- [36] Committee for Fundamental Metallurgy, *Schlackenatlas*. Dusseldorf: Verlag Stahleisen M.B.H., 1981.
- [37] J. Mukerji, "Phase Equilibrium Diagram CaO-CaF₂-2CaO.SiO₂," *Journal of the American Ceramic Society*, vol. 48, no. 4, pp. 210–213, 1965.
- [38] R. A. Brooman, "Improvements in the Manufacture of Fluoride of Silicium," *Newton's London Journal of Arts and Sciences*, vol. 4, no. 22, pp. 16–17, 1865.
- [39] J. A. Duffy, "Optical basicity: A practical acid-base theory for oxides and oxyanions," *Journal of Chemical Education*, vol. 73, no. 12, p. 1138, 1996. doi:10.1021/ed073p1138
- [40] A. Leboutellier and P. Courtine, "Improvement of a bulk optical basicity table for oxidic systems," *Journal of Solid State Chemistry*, vol. 137, no. 1, pp. 94–103, 1998. doi:10.1006/jssc.1997.7722
- [41] Collection of phase diagrams, https://www.crct.polymtl.ca/fact/phase_diagram.php?file=Ag-Fe.jpg&dir=SGTE2017 (accessed Feb. 24, 2023).
- [42] M. Asadikiya, "Oxygen ion mobility and ionic conductivity prediction in cubic yttria stabilized zirconia single crystals," *Science Trends*, 2018. <https://sciencetrends.com/oxygen-ion-mobility-ionic-conductivity-prediction-cubic-yttria-stabilized-zirconia-single-crystals/>
- [43] A. V. Virkar, "Theoretical analysis of the role of interfaces in transport through oxygen ion and electron conducting membranes," *Journal of Power Sources*, vol. 147, no. 1–2, pp. 8–31, 2005.

- [45] S. C. Britten and U. B. Pal, "Solid-State Amperometric Sensor for the In-Situ Monitoring of Slag Composition and Transport Properties," *Metallurgical and Materials Transactions B*, vol. 31, no. August, pp. 733-753, 2000.
- [46] K. R. Cooper and M. Smith, "Electrical test methods for on-line fuel cell ohmic resistance measurement," *Journal of Power Sources*, vol. 160, no. 2, pp. 1088- 1095, Oct. 2006.
- [47] A. J. Bard and L. R. Faulkner, *Electrochemical Methods: Fundamentals and Applications*, 2nd Edition. John Wiley & Sons, 2001.
- [48] C. M. A. Brett and A. M. O. Brett, *Electrochemistry Principles, Methods, and Applications*. New York: Oxford University Press, 1993.
- [49] K. E. Oberg, L. M. Friedman, W. M. Boorstein, and R. A. Rapp, "Electrochemical deoxidation of induction-stirred copper melts," *Metallurgical Transactions*, vol. 4, no. 1, pp. 75-82, 1973.
- [50] S. Yuan, U. Pal, and K. C. Chou, "Deoxidation of Molten Metals by Short Circuiting Yttria-Stabilized Zirconia Electrolyte Cell," *Journal of The Electrochemical Society*, vol. 141, no. 2, pp. 467-474, 1994.
- [51] P. Soral, U. Pal, H. R. Larson, and B. Schroeder, "A Pilot-Scale Trial of an Improved Galvanic Deoxidation Process for Refining Molten Copper," *Metallurgical and Materials Transactions B*, vol. 30, pp. 307–321, 1999. <https://doi.org/10.1007/s11663-999-0060-3>
- [52] T. A. Ramanarayanan and R. A. Rapp, "The diffusivity and solubility of oxygen in liquid tin and solid silver and the diffusivity," *Metallurgical Transactions*, vol. 3, no. 12, pp. 3239-3246, 1972.
- [53] J. Assal, B. Hallstedt, and L. J. Gauckler, "Thermodynamic assessment of the silver-oxygen system," *Journal of the American Ceramic Society*, vol. 80, no. 12, pp. 3054-3060, 2005.
- [54] M. Kilo, C. Argirusis, G. Borchardt, and R. A. Jackson, "Oxygen diffusion in yttria stabilised zirconia experimental results and molecular dynamics calculations," *Physical Chemistry Chemical Physics*, vol. 5, no. 11, pp. 2219-2224, 2003. doi:10.1039/b300151m
- [55] J. Park and R. N. Blumenthal, "Electronic Transport in 8 Mole Percent Y_2O_3 - ZrO_2 ," *Journal of The Electrochemical Society*, vol. 136, no. 10, pp. 2867-2876, 1989.

CURRICULUM VITAE

